Three-Dimensional Numerical Investigation on Velocity Field and Mixing Characteristics at Channel Junctions

by

Xue Chen

A thesis submitted in partial fulfillment of the requirements for the degree of

Master of Science

in

Water Resources Engineering

Department of Civil and Environmental Engineering
University of Alberta

ABSTRACT

Channel confluence is an important component in river systems. The flow dynamics and mixing processes associated with such geometry are highly three-dimensional and complicated. In this study, a commercial software, ANSYS CFX, was employed to investigate the flow structures and mixing characteristics at channel confluences using steady-state three-dimensional numerical method. The results indicated that the flow converging could not produce rapid mixing within the confluence or immediately downstream because of locally confined secondary current. However, with the secondary current growing downstream, the mixing rate was accelerated. Transverse mixing coefficients were determined for channel junctions with different confluent angles and discharge ratios using the generalized method of moments. This research provided the insight view on the curvature-induced secondary circulation at channel confluence and proposed the corresponding mixing rate.

ACKNOWLEDGEMENTS

I would like to express my deep gratitude to my supervisor Prof. David Z. Zhu. I sincerely appreciated that you provided me with a valuable research opportunity and constantly gave me patient guidance and great support throughout my MSc. program. Your energetic and conscientious working attitude on academic gives me a good example of conducting research. Meanwhile, your encouragement helps me overcome numerous difficulties in my study and life. I also want to express the same great thanks to Prof. Peter M. Steffler, my co-supervisor for your ingenious ideas on my project. You exercised my abilities of critical thinking and made me a qualified graduate student in Water Resources Engineering.

I acknowledge University of Alberta and the Faculty of Civil and Environmental Engineering which provides me with the research assistantship as well as the financial support.

I owe the greatest debt of gratitude to my husband, Jingzhou Huang, for his understanding, his encouragement and his love.

Last but not least, I would like to extend my great appreciation to my parents and my parents-in-law for their persistent supports.

TABLE OF CONTENT

LIST OF TABLES

LIST OF FIGURES

NOTATIONS

C = *tracer (e.g., dye) concentration*

C_{RB} and C_{LB} = concentrations at the right and left banks

C_∞ = centration of complete transverse mixing

D = *factor of diffusion*

ε_t = *turbulent diffusion coefficient*

E_y = *transverse mixing coefficient*

Fr = *Froude number*

g = *gravitational acceleration =9.81 m/s*^{2}

H_d = *downstream water depth*

I = *turbulence intensity*

k = *turbulent kinetic energy*

L_s = *length of the separation zone*

P = *turbulence production*

p = *static pressure*

Q = *combined tail water discharge m/s*^{3}

Q_1 = *main channel discharge m/s*^{3}

Q_2 = *side channel discharge m/s*^{3}

Q_1^* = *discharge ratio* Q_1/Q

q = *cumulative discharge m/s*^{3}

Sc_t = *turbulent Schmidt number=0.9*

U = *cross-sectional averaged longitudinal velocity*

U_d = *downstream velocity*

u = *local longitudinal velocity*

u^* = *dimensionless longitudinal velocity*

$u_{\_max}$ = *maximum local longitudinal velocity*

V = *cross sectional averaged transverse velocity*

v = *local transverse velocity*

v^* =*dimensionless transverse velocity*

$v_{\_min}$ = *minimum transverse velocity*

$v_{\_max}$ = *maximum transverse velocity*

W = *width of the channel*

W_s = *maximum width of separation zone*

w = *local vertical velocity*

w^* =*dimension*l*ess vertical velocity*

x,y,z = *longitudinal, transverse distance and vertical distance*

x^*,y^*,z^*= *dimensionless longitudinal, transverse and vertical coordinate distance*

α_a = *volume fraction of air*

α_w = *volume fraction of water*

μ = *the molecular viscosity of fluid*

μ_a = *molecular viscosity of air*

μ_w = *molecular viscosity of water*

μ_t = *turbulent viscosity of fluid*

υ = *kinematic viscosity of water*

ρ_w = *density of water*

ρ_a = *density of air*

δ_{ij} = *Kronecker delta*

$\sigma_\kappa, \sigma_\varepsilon, C_{\varepsilon 1}, C_{\varepsilon 2}, C_\mu$ =*constants of turbulence models*

Θ = *confluence angle*

$\emptyset$ = *passive scalar*

Ψ = *dimensionless shape velocity factor*

Chapter 1 Introduction

1.1 Research Motivation

Channel confluence is a common feature in natural river systems. In the confluence region, flow velocity, turbulence intensity, channel hydraulic geometry and bed geometry may change rapidly (Best and Roy 1991). Not only in the vicinity of channel confluence but also further downstream, substantial changes on flow hydraulic performance and channel morphology may occur (Bradbrook et al. 1998). Due to the complex hydrodynamic environment, mixing process at confluence is attracting significant interest because the mixing rate may be increased associated with confluent flow structure in some situation (Best and Roy 1991) and the knowledge on confluent mixing is important to properly assess the environmental impact of a tributary.

Considerable researches have been performed on the confluent flow structure using physical models and field measurements (Best 1986; Best and Reid 1984; Mosley 1976; Parsons et al. 2007; Rhoads and Sukhodolov 2004; Szupiany et al. 2009). The results of previous studies indicated that flow dynamics at channel confluence relied heavily on the junction angle referring to planform curvature and the ratio of discharge which is classified as flow condition (Best 1987). The former is considered to induce flow helical motion and the latter is the generation of shear dynamics between converging flows. With different junction angle and discharge ratio scenarios, researchers draw different flow patterns. However, as one of the major components of flow structure, curvature-induced helical motion is currently controversial. Visualization

investigation on the secondary flow showed the two cells rotating in opposite direction at an asymmetrical junction (Gurram et al. 1997), whereas experiment measurement (Weber et al. 2001) and numerical simulation (Bradbrook et al. 2000) suggested that only one clockwise cell downstream of the separation zone. Therefore, further research is needed to clarify the disputes of the problem.

In addition, according to Fisher et al. (1979) and Rutherford (1994)'s research, transverse mixing is a slow process that takes a significant distance downstream. However, Rhoads and Sukhodolov (2001) investigated an enhanced mixing at river junctions which had been attributed to curvature-induced helical motion. Later, Lane et al. (2008) also reported a rapid mixing at a confluence at one time period. They found that the transverse mixing took only 8km to complete compared with normal fully mixing which was 400km in distance. They attributed this rapid mixing to a significant channel-scale flow circulation which was found at channel junction. Meanwhile, the momentum ratio and density difference between the two streams also enhanced the mixing process. Based on the above discoveries, in-depth studies are necessary to investigate the relationship between the mixing rate and the confluent flow structure.

With the development of computer techniques, researches using numerical models to assess the flow characteristics and mixing at channel confluence has increased tremendously in recent years (Biron et al. 2004; Bradbrook et al. 1998; Constantinescu et al. 2011; Huang et al. 2002; Lane et al. 1999; Shakibainia et al. 2010; Wang and Cheng 2000; Weerakoon et al. 2003). In

comparison with physical junction model and field investigation, numerical model gives more inside details and saves a lot of time and expense. Therefore, in this study, three-dimensional computational fluid dynamics (CFD) model was adopted. Once the numerical model was validated with the experimental data, a matrix of numerical experiments was performed to analyze the effects of junction angle and discharge ratio on the flow characteristics and associated mixing process.

1.2 Research Objectives

The objectives of this study are to understand how the channel geometry and confluent flow condition affect the confluent flow field, especially the formation of secondary currents and then to examine to which degree mixing is reinforced by these controllers in the form of transverse mixing coefficient.

To reach these goals, a comprehensive literature review is firstly presented in Chapter 2 on channel junctions. This chapter provides a general understanding of the flow dynamics and the mixing characteristics at channel confluence from previous studies. In Chapter 3, a three-dimensional numerical model is established to a simple confluence geometry, as depicted in Figure 1-1. This geometry consists of two equal-width straight channels with horizontal floor. One is the main channel with discharge Q_1. The other one is the side channel which enters the main channel at a certain junction angle Θ with flow rate Q_2. The discharge ratio is defined as main channel flow rate divided by the total discharge of post confluence, $Q_1^* = Q_1/(Q_1 + Q_2)$. After validating the model, a systematic numerical experiment is conducted. The numerical experiments were carried out for three different junction angles 90°, 60° and 30°. For each

junction angle, three discharge ratios were simulated Q_1^*=0.75, 0.5 and 0.25. Thus, a total of 9 cases had been simulated and denoted as shown in Table 1-1. The results are demonstrated in Chapter 4. In Chapter 5, the transverse mixing coefficients are calculated based on the results of velocities and concentration variations for different junction angles and discharge ratios. Then the impact of channel geometry and flow condition on the flow structure and the mixing rate is discussed.

Table 1-1: Descriptions of all simulations.

Case	Junction Angle (θ°)	Q_1*	Q_1 (m^3/s)	Q_2 (m^3/s)	Q (m^3/s)
A1	90	0.75	0.127	0.042	0.170
A2		0.5	0.085	0.085	0.170
A3		0.25	0.042	0.127	0.170
B1	60	0.75	0.127	0.042	0.170
B2		0.5	0.085	0.085	0.170
B3		0.25	0.042	0.127	0.170
C1	30	0.75	0.127	0.042	0.170
C2		0.5	0.085	0.085	0.170
C3		0.25	0.042	0.127	0.170

Appendix entitled “River confluence of Peace River and Smoky River” is attached to this dissertation. The idea of this research was originally from this real river confluence because this site is a typical example of river mixing that the tributary contains higher pollutant level than the main stream. In addition, this junction section involves several pollutant sources, such as waste water treatment plants, pulp paper mills and oil and gas industries et al. Therefore, brief water quality and flow condition study on the Peace River, Smoky River and their post junction are presented in the appendix.

Chapter 2 Literature Review

Channel confluence is a subject that attracts many attentions in recent 30 years. Because of the complex hydraulic and morphological aspects of channel confluence, understanding the characteristic flow structures and mixing process is vital within many areas. For geomorphologists and geologists, junctions in river systems form important agents of considerable erosion and sediment transport deposition. For hydraulic and environmental engineers, the complex flow structure, such as flow acceleration, secondary flow combining with effluent injection may post considerable problems to river mixing analysis and pollutant discharge facility design. Therefore, nowadays increasing attentions have been paid to this topic to identify the confluences processes and interactions.

Considerable researches have been performed on the confluent flow structure using physical models and field measurements. Based on previous studies, factors involved in flow characteristic at confluences can be grouped into two categories: the morphology aspect and the flow condition aspect. The morphology feature includes channel junction angle, bed bathymetry and width-depth ratio, *etc*. Flow condition consists of velocity ratio or discharge ratio, Reynolds number and Froude number, *etc*. Although laboratory and field experiments provide valuable knowledge on the confluent hydraulics, very limited factors can be assessed at a time using physical models and it is difficult to obtain detailed flow measurements at real river confluence. Thus, numerical modelling is an alternative method which allows researchers set up a variety of scenarios of these variables to investigate detailed flow structures

and associated mixing processes. This chapter will review the results of previous studies on the geometrical features and the mixing characteristics of channel confluences, as well as the importance of numerical modelling method.

2.1 Geometrical Features of Channel Confluence

2.1.1 Junction Angle

There are various types of junctions existing in natural river system and hydraulic structures. As Best (1986) proposed, two types of junctions could be classified: asymmetrical "T" shaped confluence that the post-confluence channel forms a linear extension of the mainstream and symmetrical confluence that junction channel is more in "Y" shape.

The earliest researcher that attempts to develop the general confluence structure model is probably Mosley (1976). He carried out a series of lab experiments using both asymmetrical and symmetrical confluences to identify the effect of bed morphology on the flow patterns and scour formation. The results showed different shapes and locations of scour holes formed downstream of those different type of confluences; while the depth of scour hole increased rapidly as confluence angle raised from 15° to 90°, and more slowly up to 180°. Subsequently, Best and Reid (1984) conducted experiments using a "T" shaped junction to examine the flow structure under four junction angles 15°, 45°, 70° and 90°. They found the size of the separation zone enlarged systematically with an increase in confluence angle.

In addition, Best (1988) used an asymmetrical "T" shaped channel to identify the confluent channel morphology in terms of five junction angles 15°, 45°,

70°, 90° and 105°. Based on previous researches, he summarized that bed morphology could be characterized into three distinct elements: (1) a distinct avalanche face that forms at the mouth of the junctions; (2) a scour pool within the center of the post-confluence channel; (3) bars of sediment along the downstream of confluence channel. He emphasized that these elements were controlled predominantly by the confluence angle and the ratio of discharges.

As computer technology develops, more flow details are investigated by changing channel geometry utilizing numerical simulations. The simulations conducted by Bradbrook et al. (2000) using a "T" shape junction with 45° angle and "Y" shape junctions with 90° and 60° angles suggested that local variations in channel morphology could exert a substantial influence on flow structure at confluences. Huang et al. (2002) and Shakibainia et al. (2010) simulated a "T" shape junction with a range of 15° to 105° afterwards. They concluded that the flow structure was very sensitive to the junction angle.

2.1.2 Bed Morphology

Bed morphology is an important controller that impacts the flow structure. Recently, researchers found the bed discordance could influence the confluent flow characteristics as well as the mixing processes because the upwelling flow generated by bed discordance enhanced the mixing within the flow of tributary (Best and Roy 1991; Biron et al. 1996a).

Other than the bed discordance, the forming of scour hole within the junction area is another important feature for confluence. Mosley (1976) carried out a systematic laboratory experiment to identify the effect of bed morphology. By altering junction angles and discharge ratios, he found that the depth of scour

hole increased with both variables. Other researches (Parsons et al. 2007; Szupiany et al. 2009) presented results of field work similar to those in lab experiments.

2.2 Flow Characteristics within the Channel

2.2.1 Hydraulic Zones

Confluent flow is characterized by complex patterns of three-dimensional fluid motion. Best (1986) conducted a comprehensive study on flow structure at channel confluence and produced a generalized two-dimensional model for flow patterns. He proposed six hydraulic zones in confluences: (1) pronounced convergence of flow at the upstream end of the confluences, (2) a region of stagnated fluid near the upstream junction corner, (3) a well-defined mixing interface between the converging flows that persists downstream of confluence, (4) a downstream velocity field characterized by two zones of maximum velocity separated by an intervening region of low velocity centered on the mixing interface, (5) convective acceleration of flow within the mixing interface that leads to increasing uniformity of the downstream velocity field in the downstream direction, and (6) lateral deflection of flow by the dominant tributary.

Plenty of examinations of flow structure at junctions have identified these features including lab experiments (Biron et al. 1996a; Gurram et al. 1997; Weber et al. 2001) and field measurements (Best and Ashworth 1997; Rhoads and Sukhodolov 2001; Serres et al. 1999). Especially, the dimensions of the separation zone have been studied intensively. Best and Reid (1984) conducted experiments using an asymmetrical ‘T’ shaped junction channel to

examine the flow separation zone at channel confluence. The results showed that the separation zone formed at the downstream of confluence corner and as the confluence angle and discharge ratio increased, the zone of separation widened and increasingly dominated the dynamics of the confluence. Subsequently, Best and Roy (1991) suggested that for small asymmetrical junction with low-stage flows, the location of maximum topographic deflection and flow separation varied with momentum ratio and total discharge. Based on large scale experimental measurements, Yang et al. (2009) studied the size of the separation zone in three dimensions thoroughly. Due to this recirculation zone, the effective cross section area decreases and leads to flow acceleration. Therefore, flow acceleration zone has an opposite response to the junction angle and discharge ratio with the separation zone. Downstream of the separation zone, the flow expands into the flow recovery zone.

The results of previous studies indicate that for a given channel junction, the characteristics of an open-channel junction flow, such as the shape index of separation zone, flow angle of lateral channel and location of stagnation point, are quite dependent on the discharge ratio. Furthermore, Bradbrook et al. (2000) grouped the governing controls of flow structure at river confluences into three headings: (1) reach-scale pressure gradient forces associated with realignment, and changes in width/depth ratio, of the post-confluent channel; (2) topographic steering due to confluence scour and point bar formation; and (3) shear generated turbulence created by interactions between the two converging flows and bed morphology, which may affect both intermittent and time-averaged flow structures.

As mentioned above, the flow structure at confluence is complex and highly three-dimensional. These six proposed features are only representatives of time-averaged plane velocity field. Secondary circulations are also key components for the channel confluence.

2.2.2 Secondary Circulation

Secondary current in open channel confluence plays an important role in flow structure. It continuously transports momentum from center to the corner and might results in rapid mixing. Based on flow visualization in small-scale laboratory models, the secondary circulation within the Y-shaped confluence was characterized by typical two helical cells plunging down in the centre of the channel and outward at the bed, when the confluent channels were of roughly equal discharge (Ashmore et al. 1992; Mosley 1976). However, Bradbrook (2000) assumed the back-to-back helix flow existed possibly at the "Y" shaped junction, but it would disappear with an increasing unsymmetrical degree. At unsymmetrical confluences, secondary circulation was found characterized by weak surface-convergent helical cells on opposite sides of the mixing interface when the main flow discharge dominated, whereas a single large helical cell was identified when the tributary momentum was most important (Rhoads and Kenworthy 1995). This is presumably for the reason that the back-to-back helix flow might be limited because of streamline bending and morphology, much like the flow structure of two meander bends (Lane et al. 2000). Later, the field study conducted by Rhoads and Sukhodolov (2001) showed that a well-defined mixing interface persisted downstream of the two symmetrical confluences and this interface was disrupted at the

asymmetrical confluence, suggesting that helical motion enhances patterns of mixing at confluences.

However, Best and Roy (1991) reported prominent helical motion occurred at the asymmetrical confluence, whereas weak helicity was detectable only at one of the two symmetrical confluences. They stated that as the momentum of tributary increased, flow from the lateral channel increasingly deflected flow from the main stream toward the outer channel bank for asymmetrical confluence. As a result, the mixing interface between the converging flows shifted outward. Because of the curvature of the flow, the strength of helical motion was the greatest on the tributary side of the mixing interface. In addition, Orfeo et al. (2006) proposed there was no helix flow but simple converged or diffused flow at large "Y" shaped field junction. Furthermore, Parsons et al. (2007) found an absence of secondary flow at a relatively large confluence-difference unit with an aspect ratio around 200. Unlike the back-to-back strong secondary flow observed in small confluences (width to depth ratio is smaller than 100), they highlighted that the bed roughness suppressed the vertical velocity gradient so that there was no evident secondary flow in large river confluence.

Therefore, the mechanisms of secondary circulation have not been fully understood yet. The formation of secondary circulation within confluence and farther downstream for different junction angles and discharge ratios is still of great interest and requires further research.

2.3 Mixing Processes at Channel Confluence

2.3.1 Background of River Mixing

As sketched by Fischer et al. (1979), three stages can be identified for river mixing: (1) vertical mixing where the initial momentum and buoyancy of the effluent discharge dominate the rate of dilution, (2) transverse mixing where the effects of the initial momentum and buoyancy are dissipated, and turbulence and currents determine lateral mixing rate, and (3) longitudinal mixing when the effluent is fully mixed across the channel, and the process of longitudinal shear flow dispersion tends to erase any longitudinal concentration variations. The amount of time and distance for the first stage to take place is rather small in comparison with the second and third stages. Thus, fully mixing is commonly assumed for the vertical direction. In addition, for a steady state source, the longitudinal mixing can be neglected.

Physical processes involving in river mixing include advection, molecular diffusion, turbulent diffusion, dispersion and secondary circulation etc. (Elhadi et al. 1984). Advection is the transport of a substance along with the river flow. As such, the direction of the movement of the substance is the same as the direction of the river current. Molecular diffusion involves the spread of molecules due to the molecular movement. It follows the Fick's law that molecular moves from high concentration area to low concentration area. Typically, the molecular diffusion coefficient is of the order 10^{-9} m^2/s. Turbulent diffusion is the transport of substance due to the fluctuating components of velocity which cause the eddy motion that enhance the molecular diffusion. The turbulent diffusion coefficient is of the order 10^{-3} m^2/s. In comparison with turbulent diffusion, the molecular diffusion therefore is negligible. Dispersion is caused by the differential advection due to non-uniform distribution of velocity in river flow. The existing of the velocity

gradient induces concentration gradient which leads to enhanced diffusion. Secondary circulation is generated because of non-identical turbulence in all directions or flow curvature. Although secondary current only accounts for a few percentage of the main current, it reinforces the mass transport across the cross section which increases the diffusion coefficient (Elhadi et al. 1984). These physical processes all play a role in the mixing. Which one dominant the mixing rate depends on the area of interest and is still controversial.

2.3.2 Mixing Processes at Confluences

Mixing processes associated with such flow structures at confluences have attracted broad attention from engineering and environmental sides because when tributary joins in the main stream, the mixing of two streams with different water quality may take a considerable distance downstream after the confluence (Li and Morioka 1999).

Transverse mixing is a slow process that requires a significant distance downstream (Laraque et al. 2009; Maurice-Bourgoin et al. 2003; Rathbun and Rostad 2004). However, as mentioned, Lane et al. (2008) found the channel-scale flow circulation, discharge ratio and density difference could affect the mixing process. In addition, Best and Roy (1991) reported that the mixing rate could be enhanced significantly when junction channels had different bed heights. Based on previous researches, three primary flow mechanisms that contribute to mixing at river confluences are: (1) shear layer dynamics in the confluent flow (2) secondary currents associated with streamline curvature and (3) the influence of bed discordance between the two confluent channels (Rice et al. 2008). Despite series of researches carried out in this field including

laboratory experiments, observations and measurements, the understanding is still limited. Most of the mixing layer studies were performed for a specific junction under a certain discharge ratio and some of them investigated the mixing process using parallel channels which had only a simple velocity field. Thus, a thorough assessment of the mixing layer associated with flow structures at channel confluence may help to understand dispersion of solutes and suspended sediment, further on the mixing processes.

2.3.3 Transverse mixing coefficient

The transverse mixing coefficient has been studied intensively in rivers. Fischer et al. (1979) and Rutherford (1994) provided some general guidelines for the selection of the transverse mixing coefficient E_y values in natural rivers. However, E_y is very site specific. A number of factors may affect the value of E_y, such as river sinuosity, local curvature, river width, depth, discharge, river shear velocity and ice cover (Zhang and Zhu 2011). Of these factors, the effect of the river sinuosity on E_y has been recognized to be significant. Rutherford (1994) summarized from a number of studies that E_y could increase by 2–6 times downstream of some river bends. Boxall and Guymer (2003) studied a laboratory meandering channel and found that E_y raised around the bends and then decreased in the straight reaches after the bends. A similar phenomenon was also reported by Dow et al. (2009) in the North Saskatchewan River. Albers and Steffler (2007) proposed an analytical equation to quantify the change of E_y along a bend. The increase of E_y at bends is primarily caused by the helical motion of secondary currents. There have been a few recent attempts to measure the three-dimensional flow structures at bends in

laboratory models and river channels (Baek and Seo 2008; Ramón et al. 2013) in an effort to link them to transverse mixing.

However, very limited researchers reported the transverse mixing coefficient at confluences. Some of the researchers emphasized the rapid mixing at confluence, for example, Lane et al. (2000) suggested that at confluence, the helical motion generated by streamline curvature could also significantly enhance mixing much like the meandering bands. Best and Roy (1991) indicated the importance of bed discordance on rapid mixing. Bradbrook et al. (1998) and (2001) implemented systematic numerical simulation on the controls on mixing at confluences. More recently, Biron et al. (2004) simulated the rate of mixing for discordant bed and analyzed the mixing rate by means of concentration deviation downstream of the confluence. Nevertheless, none of them reported the mixing rate in terms of transverse mixing coefficient. Only Rathbun and Rostad (2004) proposed the coefficient after investigating the lateral mixing in the Mississippi River below the confluence with the Ohio River.

2.3.4 Method of Moments

The most classic method to calculate transverse mixing coefficient is the standard "method of moments" (Fischer et al. 1979), which is derived from the change of the variance of transverse concentration profiles with longitudinal distance. By using the concept of cumulative discharge, the depth-averaged, steady-state mixing equation becomes (Yotsukura and Sayre 1976)

$$\frac{\partial C}{\partial x} = D\frac{\partial^2 C}{\partial q^2} \quad \text{..... (2-1)}$$

where C= tracer (e.g., dye) concentration; x= longitudinal distance; D= factor of diffusion; and q= cumulative discharge. On the basis of C-q profiles at different cross sections, the method of moments is the most widely accepted method to calculate D:

$$D = \frac{1}{2}\frac{d\sigma_q^2}{dx} \quad \text{(2-2)}$$

where σ_q^2= variance of a C-q profile. σ_q^2 is defined as

$$\sigma_q^2 = \int_0^Q (q - q_0)^2 \, Cdq / \int_0^Q Cdq \quad \text{(2-3)}$$

where q_0= centroid of the C-q profile; and Q = total discharge. q_0 is defined as

$$q_0 = \frac{\int_0^Q Cqdq}{\int_0^Q Cdq} \quad \text{(2-4)}$$

The reach averaged transverse mixing coefficient, E_y , can then be calculated (Beltaos 1979)

$$E_y = \frac{D}{\Psi U H^2} \quad \text{(2-5)}$$

where U= average river velocity; and Ψ= dimensionless shape velocity factor, expressed as

$$\Psi = \frac{1}{UH^2Q}\int_0^Q m_x \, uh^2 dq \quad \text{(2-6)}$$

However, Eq. (2-2) is only valid before the plume impinges the nearest bank because beyond that, the plume no longer follows a Gaussian distribution. Beltaos (1979) and Rutherford (1994) derived a generalized method of moments to account for the bank effect. The general form is:

$$\sigma_q^2 = 2D \int_0^x f(x)dx \quad \text{(2-7)}$$

Beltaos (1979) used the plume concentrations at the banks to calculate $f(x)$:

$$f(x) = 1 - \left(1 - \frac{q_0}{Q}\right)\frac{C_{RB}}{C_\infty} - \frac{q_0}{Q}\frac{C_{LB}}{C_\infty} \quad \text{(2-8)}$$

where C_{RB} and C_{LB} = concentrations at the right and left banks, respectively; and C_∞= concentration of complete transverse mixing. C_∞ can be calculated as:

$$C_\infty = \frac{(C_1Q_1 + C_2Q_2)}{Q_3} \quad \text{(2-9)}$$

where$C_1$and $C_2$are the concentrations in the main and side channel channels, $Q_1$and Q_2 are the discharge in the main and side channel channels and Q_3 is the total discharge downstream of the junction. Before the plume reaches either bank,$f(x) = 1$, and Eq. (2-8) reduces to Eq. (2-2). From Eq. (2-7), when σ_q^2 is plotted with $\int_0^x f(x)dx$, half of the slope of the fitted straight line will be the value of D. E_y can then be calculated by using Eqs. (2-5) and (2-6).

2.4 Numerical Simulation

Previous researches on channel confluence provided a good understanding of the flow structure and mixing process with different flow and bed geometry variables. From the literature, there are a number of control parameters impacting flow patterns, for instance, junction angle, bed discordance and plan curvature, which are associated with channel geometry and velocity or discharge ratio, and upstream and downstream Froude numbers, which associate with the flow hydraulic condition. However, the physical models of junctions can only use limited parameters at a time to identify their impacts on

junction flow. To obtain a complete understanding of flow structure at channel confluence, all factors that impact the flow behaviour should be considered. Therefore, numerical simulation is a complementary technique that can be used to study different flow patterns under various boundary conditions.

2.4.1 Three Dimensional Numerical Model

Previously, researchers used one dimensional (1D) theoretical approach (Greated 1966; Hsu et al. 1998b; Hsu et al. 1998a; Ramamurthy et al. 1988; Talor 1944) to investigate the relationship between the depths upstream and downstream of the junction based on conservation of mass and momentum. With the increase of knowledge in junction flow, some two dimensional numerical (2D) studies regarding channel confluence have been conducted (Ghostine et al. 2010; Khan et al. 2000; Weerakoon et al. 2003). Ghostine et al. (2010) compared the 1D and 2D approaches with existing experimental data and concluded that the 1D approach could only be applied to small junction angle and small downstream Froude number, whereas 2D combining with 1D approach performed well in real measurements. Nevertheless, their assumption of 2D flow severely limits the practical applicability of their results.

As discussed in the literature, helical motion of secondary flow is an important factor impacting mixing processes at confluence which cannot be adequately simulated in 2D model. Lane et al. (1999) indicated that 3D model had an outstanding merit when simulating the bed shear stress and secondary flow, and provided more reliable data comparing to the 2D model. Therefore, many three-dimensional models and their applications have been reported in recent years. Weerakoon et al. (1991) examined the 3D flow structure at a confluence

of subcritical flows by means of experimental measurements and a computational model incorporating the standard $k-\varepsilon$ turbulence closure scheme. The predicted results suggested satisfaction with the experimental counterparts. Huang (2002) developed 3D $k-\omega$ model to simulate flow pattern with equal width channel junction that has different junction angles and discharge ratios. Shakibainia et al. (2010) conducted comprehensive 3D numerical study using SSIIM software with RNG $k-\varepsilon$ turbulence model to investigate the secondary currents, velocity distribution, separation zone and water surface elevation in different conditions. So far, only few numerical models have examined the mixing in the confluence. Bradbrook et al. (1998; 2000; 2001) did 3D numerical simulation utilising PHOENICS to study the flow structure and associated mixing at confluence, especially the controls on secondary circulation by applying the standard $k-\varepsilon$ turbulence and renormalization group (RNG) turbulence model. They also deployed large eddy simulation (LES) model to describe this turbulence model on two parallel channels. Results showed that bed discordance was a key controlling factor for mixing close to the junction. Wang and Cheng (2000) used Fluent 4.4 to simulate a side discharge into a cross channel flow. In comparison with standard $k-\varepsilon$ and RNG $k-\varepsilon$ turbulence model, they found that the latter one had a good agreement with experimental data. Biron et al. (2004) used the same three-dimensional numerical modeling tool as Bradbrook et al. (1998) to study the lateral mixing at river confluences. They indicated that the lateral mixing was significantly enhanced by the bed discordance.

Despite the investigations of confluence dynamics have been conducted by means of laboratory study, field measurement and numerical simulation, the

three dimensional model on the mixing process associated with such flow structure is still limited. Therefore, new research is called for to fill this gap.

2.4.2 Available Computational Fluid Dynamics (CFD) Models

Based on previous studies, softwares employed to simulate the junction included SSIIM, PHOENICS and ANSYS Fluent etc.. Different computational schemes and methods such as CFD codes, Large Eddy Simulation (LES) and Direct Numerical Simulation (DNS) were chosen according to the level of complexity of the fluid system, required accuracy and the programming skills.

Presently available CFD model for this study is ANSYS CFX 15.0, which is one of the well-known and acceptable numerical packages (http://www.ansys.com). The CFX is able to simulate the turbulent flow systems, which was verified both theoretically and experimentally in the literature (CFX 2009). The capability of CFX to simulate the free-surface flow was verified recently and shown to have good performance in this field of study. Many turbulence models are available in CFX package such as standard k-ε, RNG k-ε, k-ω and the Reynolds stress models. Because of the availability and research purpose, ANSYS CFX 15.0 was selected for this study.

Chapter 3 Numerical Model Setup

3.1 Governing Equations

A numerical model of the fluid flow at channel confluence was developed using ANSYS-CFX. Ansys CFX is commercial CFD software; capable of solving Reynolds-averaged Navier-Stokes (RANS) in three dimensions. For open channel flow condition, a free surface exists at the air and water interface. To determine the water surface variation, especially at the junction area, a model with the technique of solving free surface is needed. In addition, a free-surface flow model is packaged in its two-phase flow model. Therefore, Ansys CFX 15.0 is employed to solve the governing equations numerically.

The mass conservation equation and the momentum equations solved by the CFX solver are as follows (in tensor form):

Mass Conservation Equation

$$\frac{\partial \rho}{\partial t} + \frac{\partial \rho u_j}{\partial x_j} = 0 \quad \text{(3-1)}$$

Momentum Conservation Equation

$$\frac{\partial \rho u_i}{\partial t} + \frac{\partial \rho u_j u_i}{\partial x_j} = -\frac{\partial p}{\partial x_i} + \frac{\partial}{\partial x_j}\{(\mu + \mu_t)(\frac{\partial u_i}{\partial x_j} + \frac{\partial u_j}{\partial x_i}) - \frac{2}{3}\rho k \delta_{ij}\} + (\rho - \rho_a) g_i \quad \text{(3-2)}$$

where ρ is the fluid density, ρ_a is the density of air, p is the static pressure, g is the gravitational force, k is the turbulent kinetic energy, δ_{ij} is the Kronecker

delta, μ is the molecular viscosity of fluid, and μ_t is the turbulent viscosity of fluid.

In terms of free surface, ANSYS CFX employs Volume of Fraction (VOF introduced by Hirt and Nichols (1981) techniques to track the water surface location (CFX 2009). The VOF model was developed under multiphase flow theory and designed for two or more immiscible fluids by solving a single set of momentum equations and tracking the volume fraction in each computational cell throughout the domain.

Open channel confluence involves two phase flow, air and water. In this study, the phases of air and water are represented by using the subscripts *a* and *w* respectively. Accordingly, the volume fractions of air α_a and water α_w sum to unity.

$$\alpha_a + \alpha_w = 1 \quad \text{..... (3-3)}$$

This volume conservation equation is solved in the entire domain and the volume fraction is computed for each cell. According to this equation, the volume fraction of each phase ranges from 0 to 1. For example, if the cell is completely full of water, the volume fraction of water is computed to be equal to unity (α_w=1) and the cell is considered to be in the main flow region. Likewise, in the pure air region, air occupies the whole volume of the cell, its volume fraction is calculated to be equal to unity (α_a=1). Free surface exists where the value of volume fraction is between 0 and 1 ($0<\alpha_w<1$) which means the cell is partially filled with water and that location will be tracked.

Meanwhile, Equation (3-1) and (3-2) involve the physical properties of the phases, such as density and viscosity. It is apparent to determine the properties in the pure substance region; while in the free surface location, a mixed property value needs to be defined. Under the multiphase theory, computational model for multiphase flows can be classified into homogeneous model, mixture models, and inhomogeneous models (Manninen et al. 1996). Homogeneous model is the simplest multiphase flow model that all phases in the domain of interest share the same velocity field with mixture density and viscosity. Since we mainly focus on the water field, and the open channel flow usually involves little air entrainment, the homogeneous model is employed. According to Wörner (2003), the air-water mixture flow density and viscosity are determined by the phase-averaged properties in each control volume. Therefore, the properties such as density and viscosity appearing in the government Equations (3-1) and (3-2) are given by:

$$\rho = \alpha_a \rho_a + \alpha_w \rho_w \quad \text{(3-4)}$$

$$\mu = \alpha_a \mu_a + \alpha_w \mu_w \quad \text{(3-5)}$$

3.2 Turbulence Model

As RANS equations bring new unknowns (Reynolds stresses), additional equations are needed to determine the turbulence viscosity involved in Equation (3-2). The turbulence viscosity takes the form (Launder and Spalding 1974):

$$\mu_t = C_\mu \rho \frac{k^2}{\varepsilon} \quad \text{(3-6)}$$

where $k = \frac{1}{2}\overline{u_i' u_i'}$ ..... (3-7)

and $\varepsilon = \nu \frac{\partial u_i'}{\partial x_j} \frac{\partial u_i'}{\partial x_j}$ ..... (3-8)

are the turbulent kinetic energy and dissipation rate, respectively. The transport equations for k and ε at high Reynolds numbers take the form:

$$\frac{\partial k}{\partial t} + \bar{u}_i \frac{\partial k}{\partial x_i} = P - \varepsilon + \frac{\partial}{\partial x_i}\left[\frac{1}{\rho}\frac{\mu_t}{\sigma_k}\frac{\partial k}{\partial x_i}\right] \quad \text{..... (3-9)}$$

$$\frac{\partial \varepsilon}{\partial t} + \bar{u}_i \frac{\partial \varepsilon}{\partial x_i} = C_{\varepsilon 1}\frac{\varepsilon}{k}P - C_{\varepsilon 2}\frac{\varepsilon^2}{k} + \frac{\partial}{\partial x_i}\left[\frac{1}{\rho}\frac{\mu_t}{\sigma_\varepsilon}\frac{\partial \varepsilon}{\partial x_i}\right] \quad \text{..... (3-10)}$$

where P is the turbulence production given by

$$P = 2v_t\overline{S_{ij}S_{ij}} \quad \text{..... (3-11)}$$

and $\overline{S_{ij}} = \frac{1}{2}\left(\frac{\partial u_i}{x_j} + \frac{\partial u_j}{x_i}\right)$ ..... (3-12)

is the mean rate of strain tensor. There are 5 constants σ_κ, σ_ε, $C_{\varepsilon 1}$, $C_{\varepsilon 2}$, C_μ involving in Equations (3-9) and (3-10). In the standard k-ε model, these coefficients are constants obtained from experiments for equilibrium turbulent boundary layers and isotropic turbulence (Launder and Spalding 1974). The values of these coefficients are σ_κ=1.0, σ_ε=1.3, $C_{\varepsilon 1}$=1.44, $C_{\varepsilon 2}$=1.92 and C_μ =0.09. From the literature, the RNG model is more responsive to streamline curvature and flow with circulation because the coefficients in RNG k-ε model were calculated by the theory with a modification of the production of

dissipation term to account for non-equilibrium strain rates (Yakhot and Orszag 1986). Therefore, for this channel confluence study RNG *k*-ε model is adopted. These involved coefficients are σ_κ=0.7179, σ_ε=0.7179, $C_{\varepsilon 2}$=1.68, C_μ=0.085 and

$$C_{\varepsilon 1} = 1.42 - \frac{\eta(1-\eta/\eta_0)}{1+\beta\eta^3} \quad \text{..... (3-13)}$$

where $\eta = Sk/\varepsilon$, $S = \sqrt{2\overline{S_{ij}S_{ij}}}$, $\eta_0 = 4.38$ and $\beta = 0.015$.

In homogeneous multiphase flow, bulk turbulence equation is solved the same as single phase turbulence equation.

3.3 Numerical Tracer

To calculate the mixing behavior downstream of the T-Junction, an additional passive transport equation for a scalar $\emptyset$ is activated in water substance. Since the simulated flow is turbulent, the molecular diffusion is omitted. For the closure of the scalar transport equation an approach analog to the turbulent eddy viscosity is used in CFX.

$$-\overline{u_i'\emptyset'} = \varepsilon_t \frac{\partial\bar{\emptyset}}{\partial x_i} \quad \text{..... (3-14)}$$

where an overbar denotes the time averaged quantity and the primed variables are the fluctuations. The turbulent diffusion coefficient ε_t is approximated from the turbulent eddy viscosity in the following way

$$\varepsilon_t = \frac{v_t}{Sc_t} \quad \text{..... (3-15)}$$

Sc_t is the turbulent Schmidt number. In ANSYS CFX 15.0 its default value is 0.9 (CFX 2009) and this value was used for all simulations. With this turbulent closure and the neglected molecular diffusion, the transport equation for $\emptyset$ takes the following form:

$$\frac{\partial \bar{\emptyset}}{\partial t} + \overline{u_\iota \frac{\partial \bar{\emptyset}}{\partial x_\iota}} = \frac{\partial}{\partial x_i}\left(\frac{v_t}{Sc_t}\frac{\partial \bar{\emptyset}}{\partial x_i}\right) \quad \text{(3-16)}$$

3.4 Model Geometry

Model simulated domain is based on Weber et al (2001) laboratory experiments. The model geometry consists of two confluent channels with sharp-edged 90° angle. The main channel has a total length of 23.883 m. The side channel joins the main channel at 7.481 m from upstream and has a length of 5.643 m. Both main channel and side channel have the same width W=0.914 m and the same height 0.51 m. All channel floors are set to be horizontal. Regarding the coordinate system for this simulation, the numerical origin is chosen at the bottom of upstream corner. The positive x-axis direction is considered to be the downstream of main channel. The positive y-axis direction is pointing to the outer wall of the main channel. Vertical direction against the gravity is the z-axis direction. Figure 3.1 shows the layout and the dimensions of two confluent channels for this simulation.

The angle between the main and the side channel is defined as the confluence angle, θ. The upstream main channel, branch channel, and combined discharge are denoted as Q_1, Q_2, and Q, respectively. Herein, the discharge ratio is defined as $Q_1^*=Q_1/Q$. Based on the available experimental data, the total combined flow rate is set as Q=0.170 m^3/s and the downstream depth is

held constant at H_d=0.296 m. Therefore, the downstream velocity is U_d=0.628 m/s, which gives a Froude number of Fr=0.37. The characteristic values such as channel width W, downstream water depth H_d and mean velocity U_d are used to nondimensionalize results. For convenient description, the longitudinal and transverse distance are nondimensionalized by channel width, W as x*=x/W and y*=y/W. Vertical coordinate z is nondimensionalized by H_d as z*=z/H_d.

3.5 Boundary Conditions

Boundary conditions were applied to all sides or faces of the domain. The mass flow rate was specified at main and side channel upstream as inlet boundary according to the discharge ratio, which is uniformly distributed over the water and air phases. Since the air density is relatively small comparing to the water density, the air mass could be neglected. The VOF technique allows air flow through the channel above water. If no air is allowed to enter through the inlet (or air flow rate is too small), then large recirculating regions of air may occur above the water that may cause computational instabilities (Ma et al. 2002). The turbulence intensity (I) of the fluid flow at the upstream boundary was specified as medium (5%). Ma et al. (2002) noted for upland urban river that the predicted velocities are graphically indistinguishable for 5, 10, and 20% turbulence intensity. The solver uses the following expression to compute k and ε at the inlet from the given value of intensity (CFX 2009),

$$k_{in} = \frac{3}{2} I^2 u_{in}^2 \quad \text{(3-17)}$$

and $\varepsilon_{in} = \rho C_{\mu} \frac{k^2}{100 I \mu_t}$ ……..……. (3-18)

where C_{μ} is the κ–ε turbulence model constant (0.085 for RNG κ–ε). Downstream boundary was specified as static pressure with 0.296 m's water head. CFX offers the user defined expressions to calculate certain values. Therefore, the static pressure for water with 0.296 m height was computed using the static pressure equation. No-slip boundaries (indicating water flow is zero at the boundaries) were applied at all sidewalls and channel floor. The channel floor roughness height was set as 0.00006 m for smooth glass bottom. The top surface was specified as an opening boundary and this is a pressure boundary which allows both inflow and outflow.

The high resolution advection was used. The fluids are assumed to be Newtonian, isothermal, and incompressible; therefore, their properties are kept constant. Typically, the relative error between two successive iterations is specified using a convergence criterion of 0.0001 for each scaled residual component. The computations are conducted under the steady state condition.

The initial conditions for the fluid flow field may be specified in an arbitrary way. The initial values of velocities were provided as zero in inlet boundaries and the initial pressure was assumed as hydrostatic for the water region and zero for the air region in the outlet boundary. In addition to the fluid velocities and hydrostatic pressure, the water level at the inlet and outlet needs to be given to specify the water volume fraction at the boundary. This water level should be consistent with the water flow rate through the channel. For saving computational time, Weber et al.'s (2001) experimental water level was used

as initial water level at inlets of two channels. And further, for any initial water level, it is assumed that the steady water level in the computational domain should be produced as time progresses. Advection fluxes are evaluated using a high-resolution scheme that essentially involves second order accuracy.

3.6 Computational Mesh

3.6.1 Discretization Scheme

To solve the RANS equation numerically, the fluid domain needs to be discretized in nodes where the solution is obtained. There are three main types of discretization methods for PDEs (Partial Differential Equations): finite different method, finite volume method and finite element method. Finite different method is a classic numerical discretize approach that the algebraic equations systems are solved at each node based on derivative approximation. The number of algebraic equations that needs to be solved is equal to the number of nodes plus two. This method is easy to understand and express. However, it is not suitable for complex geometries and curved boundaries. Most software adopts the finite element method or finite volume method to discretize spatial domain for broad variety applicability.

Typically, in finite element method, the nodes are connected to form elements and the results are obtained at nodes on the corners or along the edges of the elements. But in finite volume method the points are centroids of control volumes and results are obtained at points. ANSYS CFX uses an element-based finite volume method to discretize the RANS equation (CFX 2009). In finite element based control volumes, the simulation domain is firstly discretized with mesh element and then the element center is constructed to

form control volumes. The finite volume approach ensures the conservation of quantities such as mass, momentum and energy. Meanwhile, the finite element method is optimum for complex geometries and local grid refinement (Ferziger and Peric 2002). The element-based finite volume approach carries the advantages of both the above methods.

3.6.2 Mesh Structure

Ansys CFX 15.0 offers two types of grids: structured grid and unstructured grid. If not specified, Ansys CFX often generates unstructured mesh for selected domain. This type of mesh is typically less efficient to generate and fit boundary well, however, artificial diffusion may be large since grid lines are not aligned with the flow. For regular geometry, such as rectangular channel, structured mesh is recommended because it is usually best suited for flow calculation and the artificial diffusion is minimum.

To better fit the geometry, the multi-block algorithm is applied to divide simulation domain into a number of blocks. Figure 3-2 shows the mesh structure and mesh blocks for this study. As seen in Figure 3-2 (a), the simulation domain consists of four blocks: upstream main channel block, upstream side channel block, the junction area block and the post junction block. Each block is geometrically simple and can be solved independently.

Usually, mesh refinement need to be done at places where the fluid properties change rapidly. Since within the junction, flow velocity, turbulence intensity and water elevation may change fast, mesh was refined around the junction as seen the darker color in Figure 3-2 (a) and the detail view is depicted in Figure

3-2 (b). And more nodes were added to boundary layer because the velocity gradient there is high as shown in Figure 3-2 (c).

3.7 Mesh Sensitivity Test

A mesh sensitivity study was conducted to determine the grid density for the simulated domain. Three mesh systems, Mesh 1 (coarse), Mesh 2 (medium), and Mesh 3 (fine) were used to examine the effect of the mesh size on the accuracy of the numerical results. Since the simulation domain was divided into several blocks and refined near the confluence, two locations were selected to conduct the mesh sensitivity test: one was upstream of the confluence and the other one was in the confluence; and two mesh sizes were tested simultaneously: one was for the refined grid and the other referred to the rest of the domain. Detailed properties of the three computational meshes are summarized in Table 3-1. Figure 3-3 (a) and (b) compare the simulated longitudinal and transverse velocity profiles for three different mesh sizes at x^*=-2 along the centerline of the junction, respectively. Figure 3-4 (a) and (b) compare the imitated longitudinal and transverse velocity profiles for three different mesh sizes at x^*=2 along the centerline of the junction, separately. At these two locations, the average differences from each other in longitudinal velocity profiles varied from 4-5%, 1.5-2%, and 1-2% m/s, respectively. And the average differences in transverse velocity profiles ranged from 4-5%, 1.5-2%, and 1.8-2% m/s, correspondingly. Accordingly, Mesh 3 has been used for all simulations.

Table 3-2: Details of three mesh properties used for computations

Mesh	1	2	3
Size (mm)	24 for refine 48 for other	22 for refine 44 for other	20 for refine 40 for other
Nodes	1,510,076	1,864,882	2,282,280
Elements	1,436,292	1,735,946	2,183,000
Hexahedra	1,436,292	1,735,946	2,183,000

3.8 Model Validation

Experimental results published by Weber et al. (2001) were used to validate the numerical simulation predictions. For this application, the low discharge ratio (Q_1*=0.25) was selected as the preceding results suggested that the low discharge ratio produced a larger separation zone and had a greater water-surface elevation change. Therefore, the case was more challenging to calculate.

3.8.1 Validation of Water Surface Elevation

Water surface is an integral quantity that is preferred to validate the numerical model because whole solution is taken into account. In CFX, the water volume fraction α_w= 0.5 (= the air volume fraction α_a) is usually assumed at water surface (CFX 2009) such that the surface was determined.

Figure 3-5 shows the comparison of the predicted nondimensionalized water surface variation along the channel with the experimental results at three

longitudinal cross sections (y^*=0.25, 0.5 and 0.75). It is seen that the overall agreement between CFD predictions and experimental measurements is good. Only at location y^*=0.25, a relatively big discrepancy existed between simulations and measurements which might due to the strong flow re-circulation. Similar deviation between numerical results and laboratory measurements in the recirculation region was shown in Shakibainia et al. (2010). This discrepancy decreased away from the flow recirculation area (location y^*=0.5 and y^*=0.75). The Mean Absolute Percentage Error (MAPE) for water level was about 5.2%, 4.1% and 3.9% for location y^*=0.25, 0.5 and 0.75, respectively.

3.8.2 Validation of Velocity

Figure 3-6 illustrates the comparison of measured and calculated longitudinal velocity $u^*=u/U_d$ at three cross sections: x^*=0, 1 and 2 and four longitudinal sections: y^*=0.125, 0.25, 0.5 and 0.75.

At location x^*=0, the figure illustrates that larger errors exist near the channel bottom. The error in the calculated velocity values may be attributed to the underestimation on the channel floor friction. As seen, the velocity profiles in the zone of interest x^*=1 and x^*=2 have good agreement between the model simulation and the experimental measurements. Especially the model gave good prediction on the velocities within the separation zone (shown in the lower left profiles) where the value had big variation vertically. Thus, it can be concluded that the predicted error from upstream does not affect the downstream results very much. The Mean Absolute Percentage Error (MAPE) for water velocity was within 10% which is reasonable for model prediction.

Chapter 4 Results

4.1.1 Hydraulic Flow Zones

Figures 4-1, 4-2 and 4-3 showed the plane view of longitudinal velocity u contours with streamlines at about middle depth z=0.15m for junction angle 90°, 60° and 30°, respectively. The sub-figures illustrated three different discharge ratios Q_1*=0.75, 0.5 and 0.25.

In general, six distinct hydraulic flow zones that defined by Best (1987) were observed in these figures. It could be seen that a stagnation zone characterized by recirculating fluid, existed at the upstream corner of the confluence just before two streams actually met each other. This zone was apparent in cases A1 and A2 owing to the fact that the mutual deflection of flows was strong for the sharp junction angle and relatively large main channel discharge. As the junction angle and discharge ratio decreased, the stagnation zone died away because two streams merged into downstream channel gradually and smoothly with milder deflection. The area where the confluent streams deflected each other is recognized as flow deflection zone. Evidently, with increasing junction angle and decreasing discharge ratio, the streamlines of the confluent streams distorted more dramatically and would take longer distance until flowing parallel to the post-confluence that was denoted as flow recovery zone.

A separation zone was created immediately below the downstream junction corner because when the side channel encountered the main stream, it was forced to change its original direction so that the side flow could not remain

attached to the wall and then it was diverged away from side bank. From the contour maps, we knew that negative longitudinal velocities existed in this region, indicating upstream motion. Thus, the area is called recirculation zone as well. Moreover, the size of the separation zone changed as the junction angle and discharge ratio varied. The plane view of longitudinal velocity at middle depth suggested that the size of the separation zone reduced as the discharge ratio rose. However, the separation zone is a highly three dimensional area (Best and Reid 1984; Shakibainia et al. 2010; Weber et al. 2001). The figures shown here only represented the two dimensions of the separation zone at a certain water depth. Detailed descriptions on the size of the separation zone affected by junction angles and discharge ratios can be found in subsequent section.

Besides the separation zone, a high velocity area formed due to the contraction of the recirculation area. From Figure 4-1, it could be found that the largest maximum velocity occurred in the case of A3 which had the largest separation zone. The maximum flow acceleration therefore responded synchronously to the growth of the separation zone. Detailed discussion of junction angles and discharge ratios influencing on the maximum velocity are shown in following section.

4.1.2 Separation Zone

The formation of the separation zone had been documented by several researchers (Best 1987; Best and Reid 1984; Shakibainia et al. 2010; Weber et al. 2001). As mentioned above, the size of the separation zone was highly three dimensional. As indicated in Fig.4-1, Fig.4-2 and Fig.4-3, the separation

zone started right at the downstream confluence corner. With flow travelling downstream, the separation zone became a certain distance away from the wall, followed by gradually re-approaching the wall. The total length of this process varied with both junction angle and discharge ratio. Besides, the width of this area was not vertically uniform. Instead, the width was small near the bottom and it reached a maximum value at a certain depth (Weber et al. 2001). Here we denote L_s as the length of the separation zone, and W_s the maximum width of the separation. For comparison purpose, these lengths were normalized by the channel width W. Therefore, non-dimensional sizes of the separation zone for all cases were plotted in Fig.4-4.

It was apparent in Fig.4-4 that the separation dimensions (both in length and width) decreased with a growing discharge ratio. For the same discharge ratio, the size of the separation zone decreased as the junction angle declined. It could be seen, however, that the rate of reduction increased at higher junction angle. Thus, case A3 (θ=90°, Q_1*=0.25) had the largest separation zone. The length and the width of the separation zone extended up to 4 times and 0.4 times of the channel width, respectively. No separation zone was detected in case C1 (θ=30°, Q_1*=0.75). This could be determined by considering the limiting condition of two parallel channels of flow joining, which would exhibited no flow separation at the downstream corner.

4.1.3 Zone of Maximum Velocity

Due to the existence of the separation zone, the real width of flow cross-section reduced. After combining the discharge from main channel and side channel, a flow acceleration zone formed besides the separation zone. It is

important to identify the location and the magnitude of maximum velocity in this area because maximum shear stress and velocity vorticity might occur.

In Figure 4-5, it depicted the non-dimensional maximum longitudinal velocity, $u_{\_max}$* (=$u_{\_max}/U_d$), in each case. As mentioned in the previous section, the higher the junction angle and the smaller the discharge ratio, the larger the separation zone which led to smaller contraction zone and velocity growth. Case A3 had the largest maximum velocity among these simulated scenarios and the magnitude of the maximum velocity was as large as approximately 1.7 times of the downstream velocity. However, case C1 had the smallest maximum velocity and its non-dimensional value approached unity. In Figure 4-5, it also illustrated that for small confluence angles (60° and 30°) the non-dimensional maximum velocity did not show much sensitivity to the discharge ratio. The reason was that the interaction between the main flow and the side flow was not that strong for small junction angle and the flow contraction was not significant.

4.1.4 Secondary Velocity Vectors

To observe the structure of secondary currents, the transverse velocity vector *v*, and the vertical velocity vector *w* for nine simulation cases were illustrated in Figure 4-6 to Figure 4-14. As seen in Fig.4-1, Fig.4-2 and Fig.4-3, the length of the separation zone extended up to 4 times of the channel width. Correspondingly, for the side view of flow structure, four cross sections, x*=1, 2, 3 and 4 were chosen near the confluence spacing one-fold width. The other four cross stream sections x*=5, 10, 15 and 18 were picked downstream of the confluence with 5-fold width interval except the last section which located at

the end of the simulation reach. Thus, eight different cross sections were plotted. The locations of the cross sections were indicated in these figures as well. Meanwhile, the longitudinal velocity contours are also shown in the figures to illustrate the area of the separation zone and the flow acceleration zone.

In these figures, evolution of the helical motion along the channel was clearly illustrated. For the case of 90° junction angle (as shown in Fig. 4-6, Fig. 4-7 and Fig. 4-8), a typical two-cell system was developed at location x^*=2. One cell was formed in the flow acceleration area and occupied a relatively large area. The formation of this cell was because of the mutual deflection of the main stream and side flow which induced local flow curvature and counter-clockwise helical motion. The other cell was relatively small and confined at the feet of the separation zone, rotating in clockwise direction. The formation of this cell was as a result of the flow spinning between the merged flows and the separation zone and it would fade away as flow passed the recirculation area. As flow travelled downstream, these two rotating cells quickly developed into a single, channel-width circulation cell as seen at location x^*=3, 4 and 5. A potential cell might exist in the separation area but it was very weak and quickly disappeared with recirculation zone ended. This finding was consistent with the study of Bradbrook (2000) who reported that only a single cell was formed in asymmetrical channel confluence. However, for the case of low discharge ratio (A3), two helical cells with the same clock-wise rotating direction were discovered from location x^*=2 to location x^*=5. The formation of these cells was owing to the fact that the side flow with large angular momentum first impinged and then was reflected by the side walls. Due to the

confinement of the boundary, two helical motions with the same rotating direction were generated, one on each side of the channel. As the confluent flow went farther downstream, the two-cell system disappeared, and the single cell rotating anti-clockwise direction appeared at location x^*=10. This clockwise helical motion continued to develop but got weaker until the end of this simulation reach.

Unlike the 90° junction case, Fig. 4-9, Fig. 4-10 and Fig. 4-11 suggested up to four helical motions existed at location x^*=2 for the confluence with 60° junction angle. Two counter-rotating cells could still be found. One was still observed in the flow acceleration area as before and the other one was located at the feet of the separation area. Moreover, two more helical cells developed at the upper right corner of the channel and in the separation zone. The latter was less surprising as 90° junction case had the same potential cell as well. Since the former was formed within the main channel region, it might be initiated by the interaction between the side channel and the main channel. The most likely reason for this phenomenon was the main stream and the side stream converged with a relatively smooth angle so that part of the main flow could keep its motion without being merged by side flow helical motion. However, for the case of 90° junction, when the side channel merged to the confluence with a sharp angle, the side flow and the main stream mingled rapidly and formed a large helical motion together. As flow travelled downstream, these helical motions reduced to one or two cells and became weaker. In terms of the low discharge ratio, two large cells with the same rotating direction were shown. And at further downstream, the single helical

circulation occupied a large area of the channel. This result was similar to that in case A3.

Regarding to the cases with 30° confluence angle, the main channel helical cell was confined on the right side of the channel (looking downstream), the helical cell of the separation area still existed and the side flow cell was trapped at the top of the second cell. The reason for this distribution was that the main flow and side flow converged with approximately the same flow direction so that the side momentum had little effect on the main flow motion. Together with rather small separation zone, the circulation pattern of tributary was limited in a narrow area. This small junction angle also led to one single helical cell formed at the right bank corner for low discharge ratio (Q_1*=0.25) which was unlike that in the cases with 90° and 60° junction angles that generated two cells. And this single cell gradually grew to a channel scale vortex rotating in the clock-wise direction as went further downstream.

In summary, helical flow pattern existed in all these junction angles and discharge ratios. Typical two counter-rotating cells were found for 90° junction angle and high discharge ratio (Q_1*=0.75 and Q_1*=0.5). However, this two-cell system only lasted a short distance and quickly developed into a single, channel-width circulation cell due to angular momentum ratio. As junction angle decreased, three main helical cells were identified. One was the separation flow cell existing at the separation zone which diminished as the separation zone ended. Another was the side flow cell that was recognized as the strongest cell by previous researchers (Shakibainia et al. 2010). The third one was the main channel cell located on one side of the channel which could

be observed clearly in 30° and 60° angle cases. For the case of 90° angle junction, the side channel entered sharply into the confluence, and thereby the main channel cell might be mingled by the side flow cell. For low discharge ratio (Q_1*=0.25), higher junction angle resulted in two circulations rotating in the same direction, whereas only one channel scale helical cell existed in small confluent angle.

4.1.5 Transverse Velocity

The previous sections presented the flow patterns in longitudinal direction. To provide a further detailed confluent flow structure, Fig.4-15, 4-16 and 4-17 were drawn to show the variations of transverse velocities along the channel with different junction angles and discharge ratios. To be consistent with the secondary velocity vectors, the horizontal axis was for eight cross sections as well. In each figure, four types of velocity components were described: the maximum transverse velocity denoted by $v_{\_max}$; the minimum transverse velocity denoted by $v_{\_min}$; the cross-sectional averaged transverse velocity named V and the cross-sectional averaged longitudinal velocity named U.

The variation of transverse velocities along the longitudinal distance suggested that the magnitude of the transverse velocities reduced as flow travelled downstream and the decreasing rate varied from case to case. For the cases with 90° confluent angle, as shown in Fig. 4-15, the transverse flow velocity near the junction reached a maximum magnitude of 0.42 m/s in section x*=2 for Q_1*=0.25, which was about 70% of the local mean velocity U= 0.6m/s. (Note, since at location x*=1 the side channel just entered the junction, the velocities showing in these figures were not really the transverse velocities for

the confluent flow. Therefore, the results at location x^*=1 will not be discussed.) The cross-stream flow strength declined sharply downstream of section x^*=4 and at section x^*=10, the transverse velocity approached zero where the double-cell circulation had broken down into one single cell, as seen in Fig. 4-6. For Q_1^*=0.75 and Q_1^*=0.5, the transverse velocities decreased from a maximum magnitude of around 0.2 m/s at location x^*=2 to about zero at location x^*=5 which indicated the less strength of transverse velocities and the shorter lasting distance comparing with that in Q_1^*=0.25.

In terms of the cases with 60° confluent angle, shown in Fig.4-16, the maximum magnitude of the transverse velocity arrived at 0.2 m/s at location x^*=2 for Q_1^*=0.25 which was about 40% of the averaged stream wise velocity U=0.5 m/s. For other discharge ratios, the strength of the transverse velocities decreased to about 30% of the mean longitudinal velocities U= 0.5 m/s. And the variations of transverse velocities along the channel were milder than that in case with 90° confluent angle. As for the case with 30° confluent angle, seen in Fig. 4-17, the transverse velocity only accounted for 20% of the mean stream wise velocity U= 0.5 m/s near the junction and declined gradually as flow went downstream.

It is interesting to see that the maximum magnitude transverse velocity occurred in the negative transverse direction for 90° junction angle, the absolute value of $v_{\_max}$ and $v_{\_min}$ were approximately the same for 60° junction angle and for 30° junction angle $v_{\_max}$ had the maximum transverse velocity which indicating the positive transverse direction. This finding suggested that increasing junction angle had a significant effect upon the intensity of

secondary circulation. This also interpreted why some of the helical cells located on one side of the channel but some sited in the center of the channel.

In summary, it is clear that in all cases, increasing junction angle resulted in greater maximum magnitude of cross-stream flow and stronger variation along the longitudinal distance. And for a given angle, the maximum magnitude of transverse velocity was lower at a higher discharge ratio. Sensitivity to changes in angles was greater with lower values of Q_1*.

4.2 Mixing Patterns at Junction Channel

A non-reacting scalar component was introduced to track the mixing processes of these two flows. Different concentrations of 0 and 1 were applied as the inlet conditions for the main channel and side channel, respectively, to predict the mixing rate of a pollutant. The pollutant was set to be neutrally buoyant and conservative. As such, it did not influence the mean density and the velocity field.

4.2.1 Mixing Characteristics at Cross Sections

From Fig.4-18 to Fig.4-26, the mixing patterns were shown at eight cross sections for all nine cases. The water velocity streamline was also illustrated in these figures to highlight the associated secondary circulation.

As demonstrated in case A1 of Figure 4-18, at location x*=1, an obvious mixing interface between the converging flows presented approximately three quarters distance from the right bank which was corresponding to the discharge ratio Q_1*=0.75. The mixing interface marked the boundary between the confluent fluids and was almost vertically uniform except for a slight

divergence at the bottom. The thickness of the interface was narrow relative to the width of the cross section. Section x^*=2 showed that with flow moving downstream, the mixing layer shifted slightly to the right bank and the band of mixing layer expanded especially at the bottom comparing with the one at the last section. Two counter rotating helical cells, as mentioned above, were located on the opposite sides of the mixing layer. In combination with the transverse velocity, although the strength of the transverse velocity was strong at this location, this two-cell system did not contribute much to the mixing as the spatial extent of each cell was confined in its original flow region. It only dragged the interface laterally and diverged the mixing interface as seen at location x^*=3. A similar vertical mixing interface with convergent helical cells on both sides was reported in field measurements on a symmetrical confluence by Rhoads and Kenworthy (1998). The contour map exhibited that the dye concentration injected in the side flow was not diluted until reaching x^*=4. But, the dye concentration was diluted quickly within the left portion of the channel where a potential circulation formed in this area. Meanwhile, a single helical cell developed at the center of the channel. As the helical motion grew downstream, it promoted the transfer of momentum on both sides of the interface and further resulted in progressive mixing at downstream locations. However, at the end of the simulation reach, the dye did not arrive at the right bank which meant the dye concentration at the right bank remained at 0.

Case A2, shown in Fig. 4-19, had a similar mixing pattern to case A1. The mixing interface had an almost vertical alignment near the confluence (from location x^*=1 to location x^*=5) and this pattern was maintained downstream without any significant change other than the mixing band expansion

especially at the bottom. Regarding the streamline, two helical cells of similar sizes formed at both sides of the mixing layer at location x^*=2. At location x^*=3, these two cells developed into a single counter-clockwise rotating circulation. This cell slightly distorted the base of the mixing layer near the junction and impelled the mixing process between the sides of the mixing interface as moving in downstream direction.

Figure 4-20 suggested a rapid mixing case of A3. At section x^*=1, the mixing interface was no longer vertically perpendicular to the bed. Rather, it became distorted due to the mutual deflection between the side flow with large discharge and the main stream with a small flow rate. As seen, the base of the mixing layer was pulled towards the side channel area and the top skewed to the right. As mentioned above, with flow converging, two helical cells rotating in the same direction were generated owing to the fact that the side flow impinged and reflected by the side wall. These two strong circulations highly enhanced the mixing of two fluids so that a complete mixing was observed at section x^*=15.

As for the cases with 60° junction angle, depicted in Fig. 4-21, Fig. 4-22 and Fig. 4-23, the characteristic of mixing rate was alike right-angled channel with corresponding discharge ratio that case B3 had the most rapidest mixing rate in which mixing almost completed at the end of the simulation reach, followed by case B2 and then by case B1. Differently, the mixing interface was found not vertically uniformly perpendicular to the bed, but careened to the left at the top. Moreover, the dilution of concentration on the left side of the mixing layer was quicker comparing with 90° angle case near the confluence. This was

attributed to the helical motions that generated on the left area, as shown in streamlines. However, these helical circulations only restrained within a confined region that could not cause a thorough mixing across the channel. Once the helical cell developed within the mixing interface as seen at location x^*=4, the mixing process became quicker afterwards as the exchange of the fluid on both sides of the mixing layer accelerated.

With regard to the cases with 30° junction angle in Figure 4-24, 4-25 and 4-26, the segregation in the concentration remained very strong downstream in comparison with the other two junction angle cases. As mentioned in the previous section, for large discharge ratios, two circulation cells formed that left side of the mixing interface and one cell developed on the right corner of the channel. It is interesting to see that these helical cells stayed on each side of the channel without relocation at downstream cross sections which proved foregoing finding that local restrained secondary current had limited effect on the mixing rate. In terms of the case with low discharge ratio, one small single helical motion gradually grew into a channel scale circulation and the mixing layer was distorted due to this cell which implied a fast mixing process. However, this case (case C3) did not complete transverse mixing at the end of the reach because of the relative small strength of the transverse velocity.

To sum up, an obvious mixing interface existed within the confluence. The lateral position of the interface at the first cross section was consistent with the disparity in the discharge ratio between the converging flows. In combination with the results of the velocity patterns, the structure of the mixing interface remained nearly vertical when flanked by two helical cells. As flow went

downstream, the distortion and disruption of this interface suggested that the helical motion in place enhanced patterns of mixing. Generally, for a certain junction angle, the dye in low discharge ratio case mixed rapidly with the ambient water; whereas the dye concentration was diluted slowly for high discharge ratio. This was related to the magnitude of the transverse velocity discussed in previous section.

4.2.2 Depth Averaged Concentration Profile

In order to investigate the cross sectional and the longitudinal mixing variations, the depth averaged dye concentrations were plotted with transverse distance in Fig.4-27, Fig.4-28 and Fig.4-29 for all nine cases.

As seen in these figures, the variation of the depth averaged dye concentration was consistent with the mixing characteristics shown in contour maps (Fig.4-18-Fig.2-26). At location x^*=1, the dye concentrations at left bank and right bank were 1 and 0, respectively. The location of the big drop of the concentration indicated the mixing interface of side flow and main stream, and it corresponded to the discharge ratio. From location x^*=2 to location x^*=5, the variations of concentration did not change very much except for the cases with low discharge ratio, Q_1^*=0.25, which showed the differences of the dye concentrations between the left bank and the right bank decreased already. As flow travelled downstream, the change of the concentration variation accelerated but the rates of changing were different from case to case. As seen, case A3 had the smallest concentration variation at location x^*=15 where the dye concentrations at the left bank and right bank were almost the same at the value of 0.8, indicating a complete mixing. The second smallest was case B3

which had a concentration difference of 0.12 between the two banks at the end of the simulation domain. The third one was case C3 with a concentration difference of 0.4. None of the other cases showed the same fast mixing as these three and the dye concentration on the right bank in some of them even remained 0 at the end of channel. To rank the mixing rate of these cases, further calculation was needed.

Therefore, the transverse mixing coefficients for nine cases were computed using the method of moments to evaluate the speed of mixing processes quantitatively. The detailed analyses and discussions are shown in the next chapter.

Chapter 5 Analysis and Discussion

5.1 Calculation of Transverse Mixing Coefficient

In order to use Generalized Method of Moments to analyze the transvers mixing of the junction, the profile of concentration versus accumulated discharge *C*-*q* needs to compute. Since the simulation channel in this study is rectangular, the *C*-*q* profile has similar changing variation as the *C*-*x* profiles which was shown in Fig.4-27, Fig.4-28 and Fig.4-29. Thus, the *C*-*q* profiles are not demonstrated here. Then, the variance of the *C*-*q* distribution, σ_q^2 , for all simulation scenarios were plotted with integrated longitudinal distance $\int_0^x f(x)dx$ as indicated in Fig. 5-1, Fig.5-2 and Fig.5-3 and the transverse factor of diffusion *D*, could be determined as half the slope of the straight line fitted to the data points.

It was evident that the results for each case could be broken down into three main segments. A rather steep slope characterized the first segments from Section x^*=1 to Section x^*=2; a relatively flat slope characterized the second segment spanning from Section x^*=2 to Section x^*=5; the third segment exhibited a steep slope from Section x^*=5 to Section x^*=18, the end of the study area. The first segment occurred where the side flow just entered the confluence and was represented by the initial transverse spreading. This segment showed a rapid mixing of the dye which was suspected that the initial side flow momentum dominated in this section. The second relatively flat segment indicated a relatively slow mixing process, although helical circulations and large transverse velocity existed in this region. This

phenomenon was because the circulation was largely confined in the flow tube rather than within the mixing layer. The third segment suggested a rapid mixing from section x^*=5 to Section x^*=18 as flow passed the contraction zone and started expanding resulting in fully developed helical cells blending the confluent flows.

To quantitatively evaluate the mixing rate, linear trend lines were fit to each segment and the factor of transverse diffusion for each segment was calculated as tabulated in the third column in Table 5-1.

Table 5-1: Calculation of Transverse Mixing Coefficients

Case	Θ (°)	Q_1*	D $0.5*d\sigma_q^2/dx$	U (m/s)	E_y (m^2/s)	u^* (m/s)	E_y/u^*h	x*	E_y/u^*h _ave.
A1	**90°**	**0.75**	0.0001	0.55	1.89E-03	0.014	0.422	1-2	0.217
			0.000003	0.56	5.69E-05	0.015	0.014	2-5	
			0.00004	0.52	8.78E-04	0.014	0.216	5-18	
A2		**0.5**	0.0002	0.5	4.72E-03	0.013	1.228	1-2	0.540
			0.000004	0.49	1.12E-04	0.013	0.032	2-5	
			0.00005	0.45	1.27E-03	0.012	0.361	5-18	
A3		**0.25**	0.0004	0.49	9.71E-03	0.013	2.584	1-2	1.819
			0.0001	0.5	3.20E-03	0.013	0.959	2-5	
			0.00025	0.45	6.61E-03	0.012	1.915	5-18	
B1	**60°**	**0.75**	0.0001	0.44	2.36E-03	0.012	0.659	1-2	0.270
			0.000005	0.57	1.12E-04	0.015	0.026	2-5	
			0.000025	0.54	5.28E-04	0.014	0.125	5-18	
B2		**0.5**	0.0001	0.44	2.68E-03	0.012	0.793	1-2	0.310
			0.000002	0.6	4.57E-05	0.016	0.011	2-5	
			0.000025	0.54	5.28E-04	0.014	0.125	5-18	
B3		**0.25**	0.00035	0.43	9.68E-03	0.011	2.936	1-2	1.448
			0.000035	0.61	8.49E-04	0.016	0.201	2-5	
			0.00025	0.55	5.19E-03	0.015	1.207	5-18	
C1	**30°**	**0.75**	0.00003	0.33	9.46E-04	0.009	0.351	1-2	0.185
			0.000015	0.54	3.09E-04	0.014	0.072	2-5	
			0.000025	0.53	5.38E-04	0.014	0.130	5-18	
C2		**0.5**	0. 00005	0.33	1.58E-03	0.009	0.586	1-2	0.260
			0.00002	0.55	4.04E-04	0.015	0.093	2-5	
			0.00002	0.54	4.23E-04	0.014	0.100	5-18	
C3		**0.25**	0.00005	0.31	1.79E-03	0.008	0.730	1-2	0.628
			0.00015	0.52	3.43E-03	0.014	0.860	2-5	
			0.00005	0.5	1.14E-03	0.013	0.292	5-18	

The water depth and velocity magnitude were determined from the hydrodynamic model. These values were then averaged for these segments in order to compute the transverse mixing coefficient E_y, and the dimensionless transverse mixing coefficient $E_y/u*h$. All these analytic results were tabulated in Table 5-1. Referring to the mean dimensionless transverse mixing coefficient, the mixing rate of side flow under certain confluent junction angle and discharge ratio were ranked as follows: A3 > B3 > C3 > A2 > B2 > B1>C2>A1>C1.

According to Rutherford's (1994) summary of the dimensionless transverse mixing coefficient $E_y/u*h$, our results for the nine cases fell within his suggested ranges. The mixing coefficients of case A3 and B3 were within the empirical range of 1~3, which was for sharp curved channel; the values of mixing coefficients for case A2, B2 and C3 were between 0.3 and 0.9, which was for gently meandering channel and the coefficients of case A1, B1, C1 and C2 fell into the empirical range of 0.1~0.3 which was for straight channel.

5.2 Streamline Curvature Induced Secondary Flow

Curvature-induced helical flow or secondary circulation is commonly observed in meandering channels. This helical motion is produced by the local unbalance of pressure gradient and the centrifugal force (Yahata et al. 2010). Rozovskii (1961) summarized the development of secondary currents in curved channels from the results of several theoretical and experimental studies. He stated that the helical secondary circulation was formed because of the transverse velocity toward the concave of the bank when flow entered a bend. The secondary current gradually developed with the continuous curing

of the bend and the increasing of the transverse velocity. When the channel became straight, the secondary current decreased with distance and eventually dissipated. For joining straight channels, the mutual deflection of flows also generated curved flow streamlines at upstream confluence and impacted the downstream flow structure. The degree of deflection was not only related to the confluence itself, but also depended on the discharge ratio. The curved dividing streamlines and their calculated curvatures were plotted in Fig.5-4. The equation used to compute the streamline curvature is as followed:

$$k = \frac{f(x)''}{(1+f(x)'^2)^{3/2}} \quad \text{(5-1)}$$

where k is the curvature m^{-1}; f(x) is the curve function which was estimated by best-fit polynomial as shown in Fig.5-4. However, the polynomial has a defect that when it fits the straight line it becomes highly oscillatory and has a bad fit condition. Thus, in Fig.5-4 the values of curvature at both ends of the streamline are ignored.

As seen in Fig.5-4, case A3 had the strongest streamline curve. The magnitude of the streamline curvature was about 0.8 m^{-1}. In combination with the results of transverse velocity vectors depicted in Fig.4-8, this curve induced high transverse velocity toward the right bank (concave) and return flows with strong basal velocity towards the left bank which further generated two strong circulations rotating in the clockwise direction. The curvatures of case A1 and case A2 were approximately 0.5 m^{-1} and 0.7 m^{-1}, respectively. However, unlike the low discharge ratio case or meandering channel that flow curved against the rigid channel boundary, the side flow meandered versus the yielding fluid so that twin helical motions were formed near the junction as

seen in Fig.4-6 and Fig.4-7. Due to the uneven forces at the curve, these helical cells were not identical. The one formed at the concave curve was relatively big and rotated in anti-clockwise direction and the other one located at the convex curve was small and spun in clockwise direction. These two-system cells existed only in a short distance and then they developed into a single anti-clockwise circulation. But the size and location of the circulations were different. Case A1 had a relatively small helical cell which formed in the center of the channel, whereas the circulation in case A2 was bigger and was pushed to the right bank corner. Similar trends of streamline curvatures were found in other two junction angle cases. For those mildly meandered streamlines, more than one circulation was noticed as mentioned in the previous section. For highly curved streamlines, like case B3 and C3, large and strong helical cells were formed at the right channel corner. These helical cells were less strong and occupied in limited area within the channel.

Other than the velocity vector, the secondary current can be quantified using another parameter, vorticity $\vec{\xi}$. Vorticity is a measure of the rate of rotation of a fluid element about its three axes, which are *x* (longitudinal), *y* (lateral) and *z* (vertical) directions (Shen 2009). For assessing the secondary current, only the longitudinal component of vorticity is calculated here, which is denoted as:

$$\vec{\xi} = (\frac{\partial w}{\partial y} - \frac{\partial v}{\partial z})\vec{\imath} \quad \text{(5–2)}$$

where *v* and *w* are velocity components in the *y* and *z* directions, while $\vec{\imath}$ is a unit vector in the *x* direction. Since the vorticity is vector, its negative and positive signs corresponded to clockwise and counter-clockwise flow spin, respectively. To see the strength of the streamline curvature-induced

secondary flow, the magnitude of vorticity was concerned. Fig.5-5 showed the maximum absolute value of longitudinal component of velocity vorticity at eight cross sections for nine cases. As seen, the higher the streamline curved, the quicker the helical cell rotated. The maximum absolute value of vorticity occurred at where the apex of the streamline happened. As the curvature decreased, the rotating speed of helical cell declined. Even if the curvature-driven secondary current was very small at the end of the simulation, in the case of right-angled junction the vorticity was not zero, which indicated the strong curvature impacted the flow structure very far downstream of the junction.

5.3 Implications of Secondary Current for Mixing

Secondary current was found to be an important factor for rapid mixing (Biron et al. 2004; Bradbrook et al. 1998; Gaudet and Roy 1995; Lane et al. 2008). However, previous studies mainly focused on the bed discordance generated upwelling helical cell, which showed an enhancement impact on mixing immediately in the junction. For confluence with concordant bed, although secondary circulations were observed, the mixing layer was not revealed distorted near the confluence from dye tracer study (Rhoads and Sukhodolov 2004) and thermal mixing study (Rhoads and Sukhodolov 2001). Rhoads and Sukhodolov (2008) also found that even if flow within the mixing interface was highly unstable, the width of the mixing interface and the spatial extent of coherent vortices within the mixing interface exhibited limited lateral growth in the downstream direction.

Similar results from numerical simulation and data analyses were shown in this study. Within the confluence, the mixing interface was discovered almost uniform vertically near the junction and the helical motion largely was confined to the ambient flow on the sides of the mixing layer that did not contribute much to the mixing process. Only as flow passed the contraction zone and moved downstream did developed helical motion enhance mixing as secondary currents grew quickly in recirculation at expansions (Yahata et al. 2010). This phenomenon could be proved by the calculated transverse mixing coefficient which indicated that the mixing coefficient at the second segment was very small comparing with that of the third segment. For low discharge ratio, the secondary circulation produced substantial distortion of the vertical structure of the mixing interface that enhanced mixing.

Therefore, the available evidence suggested that the secondary current that enhancing mixing rate highly depended on its size, strength, especially the location. Even a small single helical motion could promote mixing as long as the circulation was generated within the mixing interface and lead to mixing interface distortion. If two large rotating cells were located on the two sides of the mixing layer, their contribution to the rapid mixing would be limited.

5.4 Mixing Rate Associated with Junction Angle, Flow Condition and Turbulent Diffusion

Previous section discussed the curvature-induced secondary flow and its implication for mixing. Other than the secondary flow, the mixing rate is related to the turbulent diffusion as well. In CFX, the turbulent diffusion ε_t is approximated from the turbulent eddy viscosity. Figure 5-6 illustrated the

contour map of the water eddy viscosity for nine cases. Note that the contour map shows the kinematic viscosity with the unit of Pa • s. Generally, as seen in these pictures, increasing junction angle had a significant effect upon the distribution and maximum value of eddy viscosity. Especially when the junction angle changed from 30° to 60°, the eddy viscosity varied from almost zero distribution to an obvious variation along the channel. For case A3, the downstream turbulence viscosity at the interface of confluent flows was about 3.0 Pa • s (=3.0E-03 m^2/s). In combination with the transverse mixing coefficient E_y (m^2/s) for case A3 at the third section showing in Table 5-1 column six, the turbulence diffusion accounted for approximately half of the contribution of enhanced mixing among other factors. For case B3, the downstream eddy viscosity at the interface of confluent flows was about 2.0 Pa • s (=2.0E-03 m^2/s) which was about 40% of the mixing rate E_y =5.19E-03 at the third section. For case C3, about 44% of the rapid mixing attributed to the turbulent diffusion. This finding gave an idea that the turbulent diffusion had around half of the contribution to the rapid mixing.

The maximum value of eddy viscosity for each case was shown in Figure 5-7. For a certain junction angle, the maximum value of eddy viscosity increased as the discharge ratio decreased, which indicated that the lateral momentum fluxes were important in the generation of turbulence.

To better investigate the impact of junction geometry and flow condition on the transverse mixing, Fig. 5-8 illustrated the comparison of mixing coefficients for nine cases. It was clear to see that the junction angle had a significant effect upon the transverse mixing rate when the discharge ratio was

small. But for high discharge ratio, the transverse mixing coefficient did not show much sensitivity to the junction angle. For junction angles>30°, discharge ratio seemed to be a more important determinant of transverse mixing rate than junction angle.

Chapter 6 Conclusions and Recommendations

6.1 Conclusions

In order to investigate the flow structure and mixing characteristics at channel confluence, a set of numerical experiments were conducted using a commercial three-dimensional CFD model, Ansys CFX 15.0. A standard numerical modeling procedure including geometry setup, mesh generation, mesh independence test, equation and turbulence model selection and model validation was performed. In comparison with lab measured data of Webber et al. (2001), the numerical results suggested that the model could provide a satisfactory prediction of the water surface elevation and the velocity field. After successfully validation, the model was then applied to different confluence geometries with varying flow conditions.

The numerical experiments were conducted on three different junction angles, (A) 90°, (B) 60° and (C) 30°. For each junction angle, three discharge ratios were simulated (1) Q_1*=0.75, (2) Q_1*=0.5 and (3) Q_1*=0.25. The discharge ratio Q_1* is defined as the main stream discharge Q_1 divided by the total downstream discharge Q_1+Q_2. Thus total nine cases were studied.

Typical flow hydraulic zones were observed. Results showed that the stagnation zone could only be visually observed in cases A1 and A2. The size of the separation zone and the maximum velocity in flow acceleration zone highly depended on the junction angle and discharge ratio. The higher junction angle and the lower discharge ratio lead to bigger separation zone and

maximum velocity. However, these elements did not show much sensitivity to discharge ratio when the junction angle was small.

The assessment of the secondary current indicated that coherent helical motion existed in all simulation cases, which stated a prominent feature of the flow structure at channel confluence. However, the size, location and strength of the circulations were quite different because of the imbalance of curvature-induced transverse velocity. For the case with 90° junction angle, two helical cells were generated near the confluence and quickly developed into a single counter-clockwise rotating cell in the center (Q_1*=0.75) or on the right side (Q_1*=0.5) of the channel. For Q_1*=0.25, one single strong circulation was formed near the confluence and then it became two helical cells both spinning in the clockwise direction. As the junction angle decreased and the curvature of the streamline declined (θ=60° and θ=30°), three main secondary cells were identified: the main channel circulation located on the right side of the channel; the separation zone cell which formed within the separation area and the side flow helical circulation which was generated between the two cells. For lower discharge ratio, Q_1*=0.25, only one strong clockwise rotating circulation was found for θ=30°.

Associated with such flow structure, the mixing pattern at confluence was investigated. Near the confluence, the location of the mixing interface highly depended on the discharge ratio and junction angle. For high discharge ratio (Q_1*=0.5 and Q_1*=0.75), the structure of mixing interface remained nearly vertical when flanked by two counter-rotating cells which were recognized to have little contribution to fast mixing. With the development of the secondary

currents, the persistence of the counter-clockwise cell on the right side of the channel and the diminution of the other cell resulted in lateral movement of water from the side channel, which caused the fast spreading of the dye concentration. For low discharge ratio (Q_1*=0.25), mixing interface was strongly distorted. With the combination of the strong channel scale secondary circulation, the lateral mixing process was highly enhanced.

Analysis of the tracer data using generalized method of moments approach was undertaken. The coefficients of transverse mixing at different cross sections were shown to exhibit considerable variations over the longitudinal distance. The first segment from Section x*=1 to Section x*=2 exhibited a rather fast mixing that might be due to the initial momentum of the side flow. A relatively slow mixing characterized the second segment spanning from Section x*=2 to Section x*=5 attributing to the confined secondary current. The third segment showed a rapid lateral mixing from Section x*=5 to Section x*=18, the end of the study area. Overall, the averaged transverse mixing coefficients suggested the junction angle had a significant effect upon the transverse mixing rate. For junction angles>30°, discharge ratio became a more important determinant on transverse mixing rate than junction angle. The results of transverse mixing coefficients for these nine cases could be sorted as follows: A3 > B3 > C3 > A2 > B2 > B1>C2>A1>C1.

Discussions on the factors that enhanced mixing rate found that the vorticity could be used as one of the measurements to quantity the strength of the streamline curvature-induced secondary flow. The higher the streamline curved, the quicker the helical cell rotated and the faster the mixing was

accelerated. Turbulent diffusion was another factor that attribute to mixing. For a certain junction angle, the maximum value of eddy viscosity increased as the discharge ratio decreased. For the cases with higher junction angle and lower discharge ratio, the turbulent diffusion was found to have around half of the contribution to the rapid mixing.

In summary, this research provided the relationship between the channel confluence with flow condition and the transverse mixing coefficient. Our results can help people better understand the flow structure and mixing characteristics associated with confluence and further make optimum decision on engineering design.

6.2 Recommendations

Overall, this dissertation improves our understanding on flow structure and mixing pattern at channel confluences. There are still some gaps left in this area. The following are suggested as the subject of future work.

Firstly, this research has focused on the flow patterns and mixing characteristics at laboratory-scale junctions with relatively small width-to-depth ratios (~3). However, natural junctions are typically more than hundreds meters wide and only few meters deep with a large aspect ratios (>100). Therefore, studies on large river channel confluences are needed in order to assess the similarities and differences between small and large confluences.

Secondly, secondary current is an important factor that impact mixing and its strength contributes to the rate of mixing. In this study, the secondary current is quantified using vorticity $\vec{\xi}$ which measures the rate of fluid rotation.

However, the strength of the helical current is not only depending on the rotating rate but also related to its occupation area. Consequently, additional spatial hydraulic metrics such as circulation are needed to characterize the complex helical motions. Moreover, other factors such as the shear layer dynamics between two flows and coherent turbulence structures are also influencing the mixing processes. Detailed investigations into how to quantify the helical flows and their impacts on the mixing are needed in future research.

Last but not least, flow structure is largely depending on the number of mesh grids. Although three-dimensional numerical model is a very powerful tool, more computer memories are required to generate nodes especially for large natural river channels with complex geometry. The major challenge for such numerical domain is to generate boundary-fitted grid. Thus advanced mesh generation techniques is needed if the expense of computer is viable.

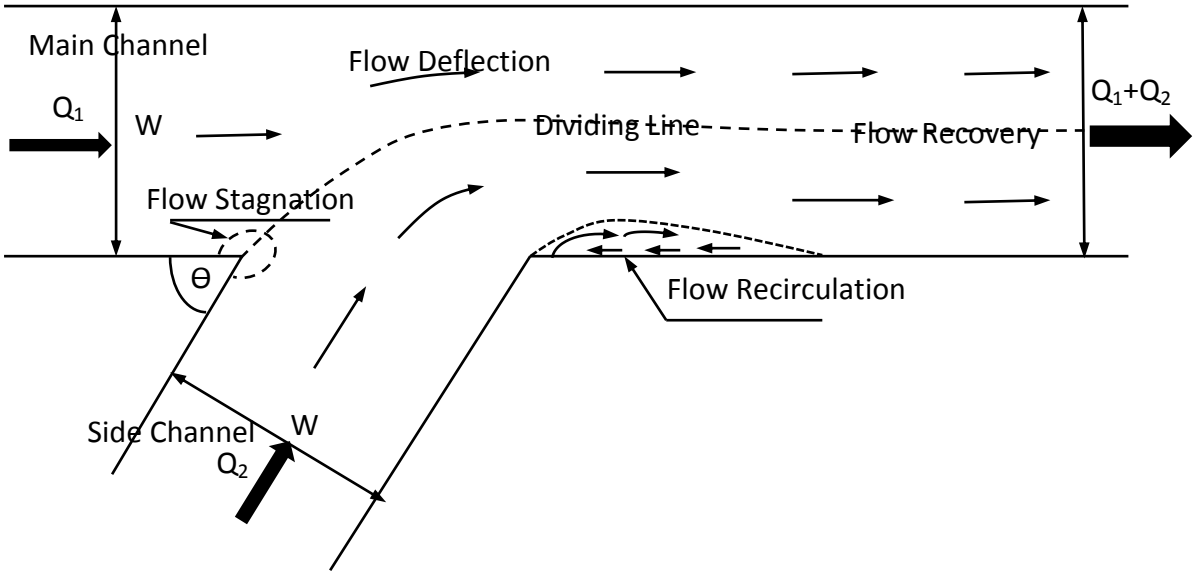

Figure 1-1: Schematic of Converging Flows at Simple Confluence Geometry

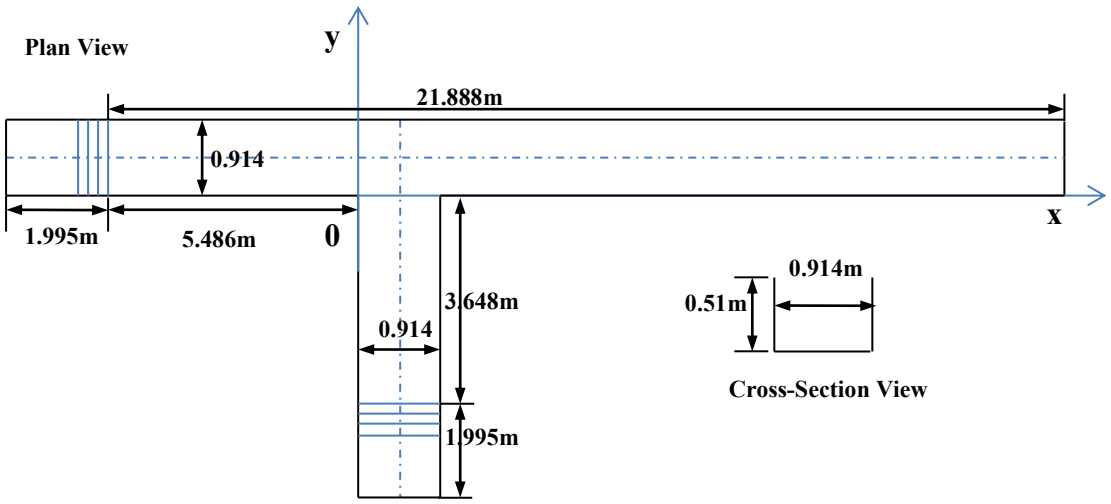

Figure 3-1: Dimensions of two confluent channels for the simulation.

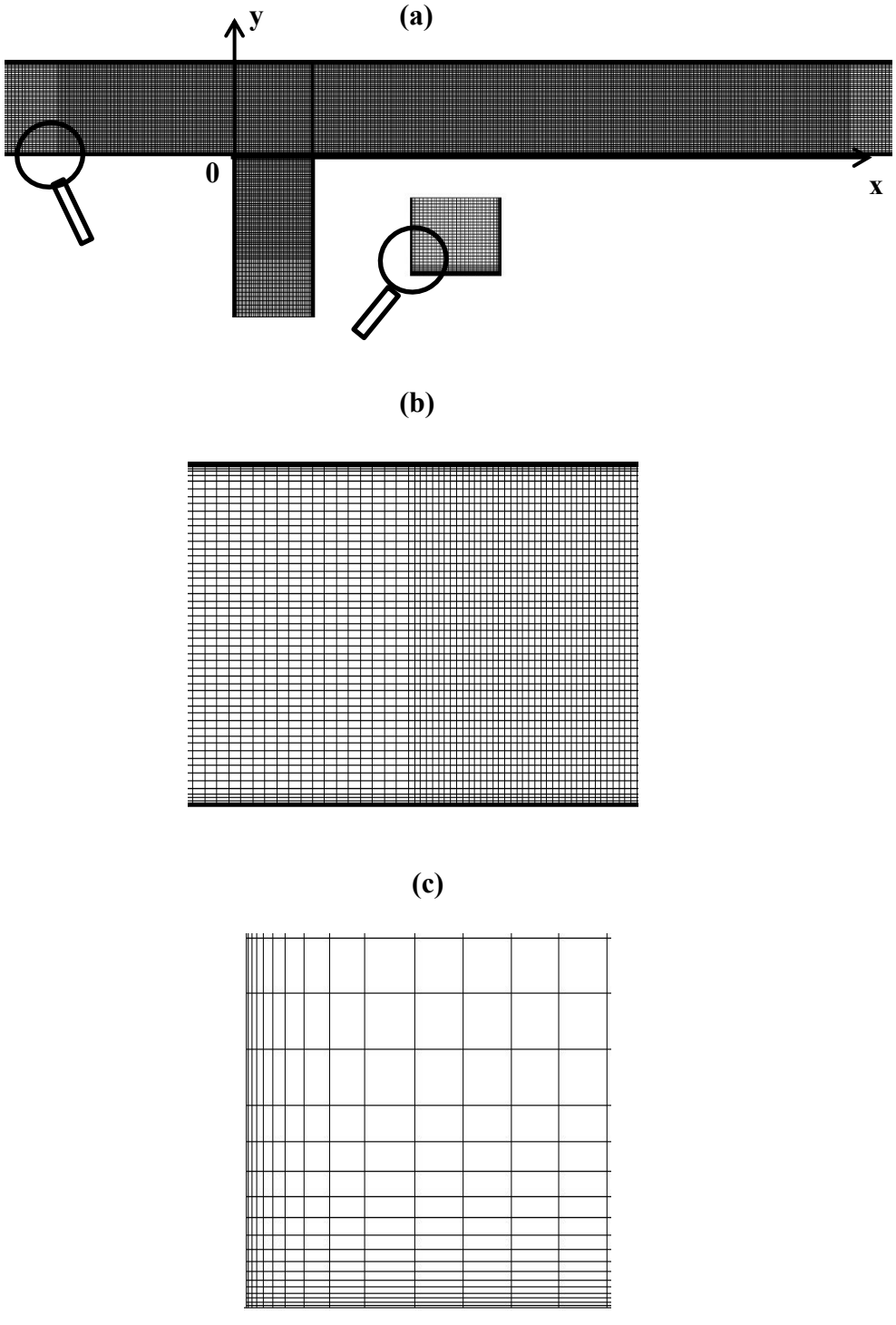

Figure 3-2: Mesh structure and blocks (a) general view of mesh (b) detailed view of transition of mesh refinement (c) mesh refinement at boundary

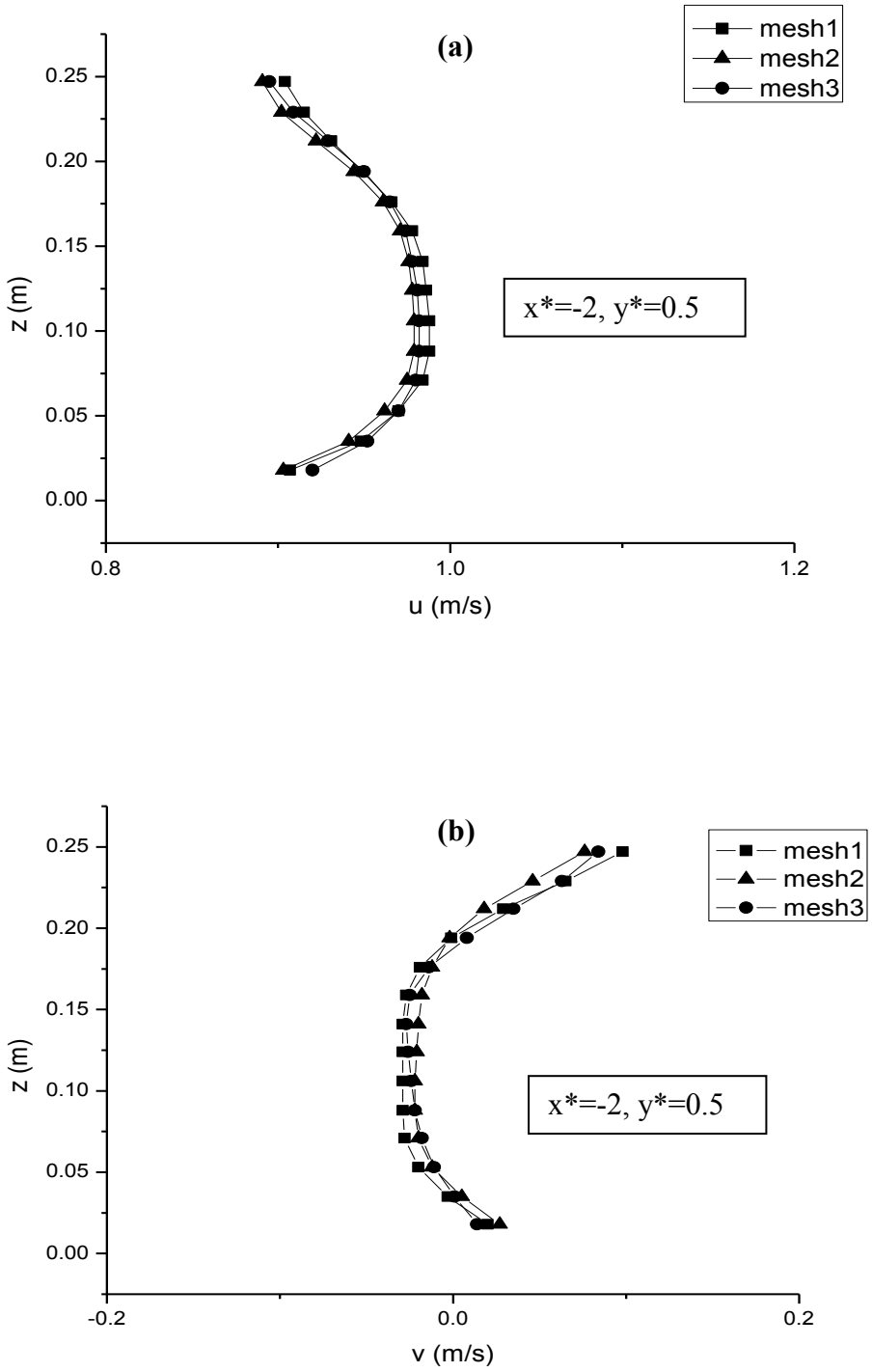

Figure 3-3: Comparison of the simulated stream wise (a) and cross-stream (b) velocity profiles for different mesh sizes at location x^*=-2, y^*=0.5

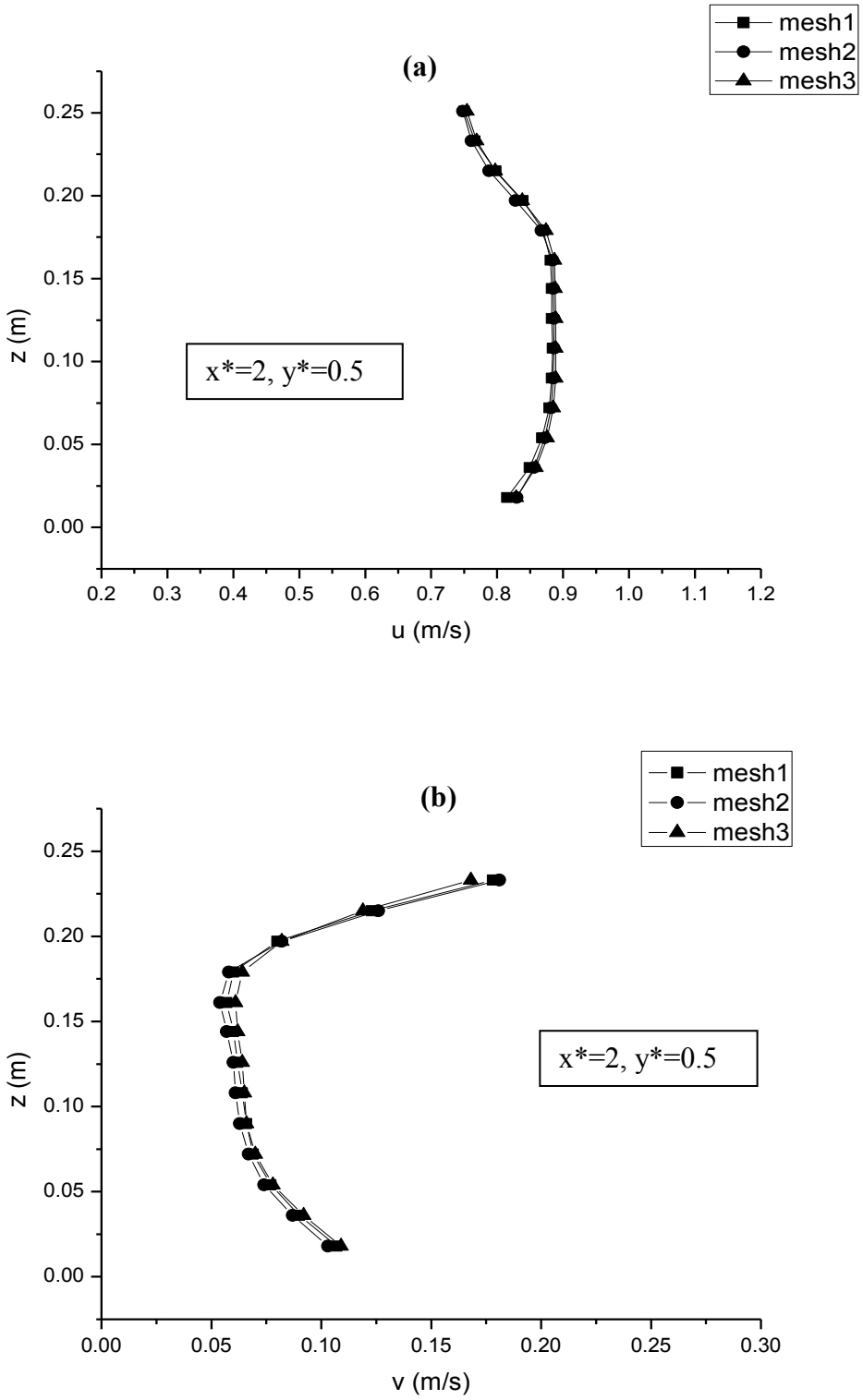

Figure 3-4: Comparison of the simulated stream wise (a) and cross-stream (b) velocity profiles for different mesh sizes at location $x^*=2$, $y^*=0.5$

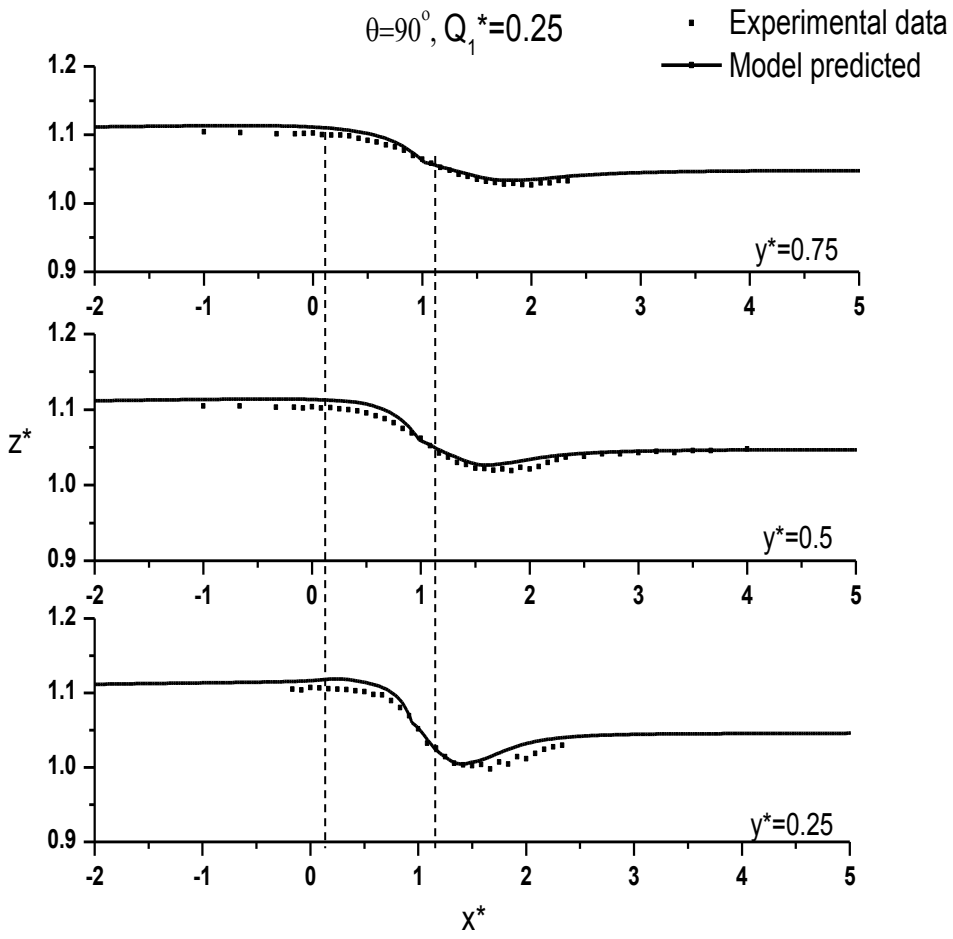

Figure 3-5: Comparison of measured and calculated water surface elevation for Q_1*=0.25 at three longitudinal sections y*=0.25, y*=0.5 and y*=0.75.

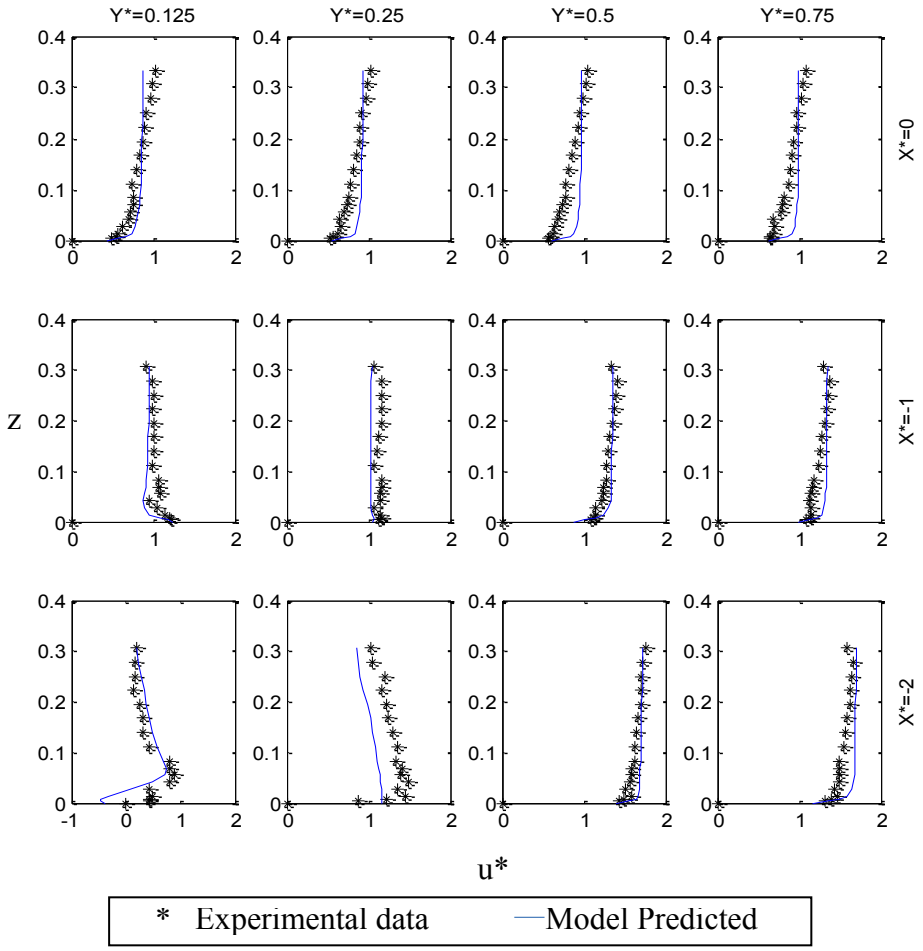

Figure 3-6: Comparison of measured and calculated non-dimensional streamwise velocity for Q_1*=0.25 at three cross sections and four longitudinal sections.

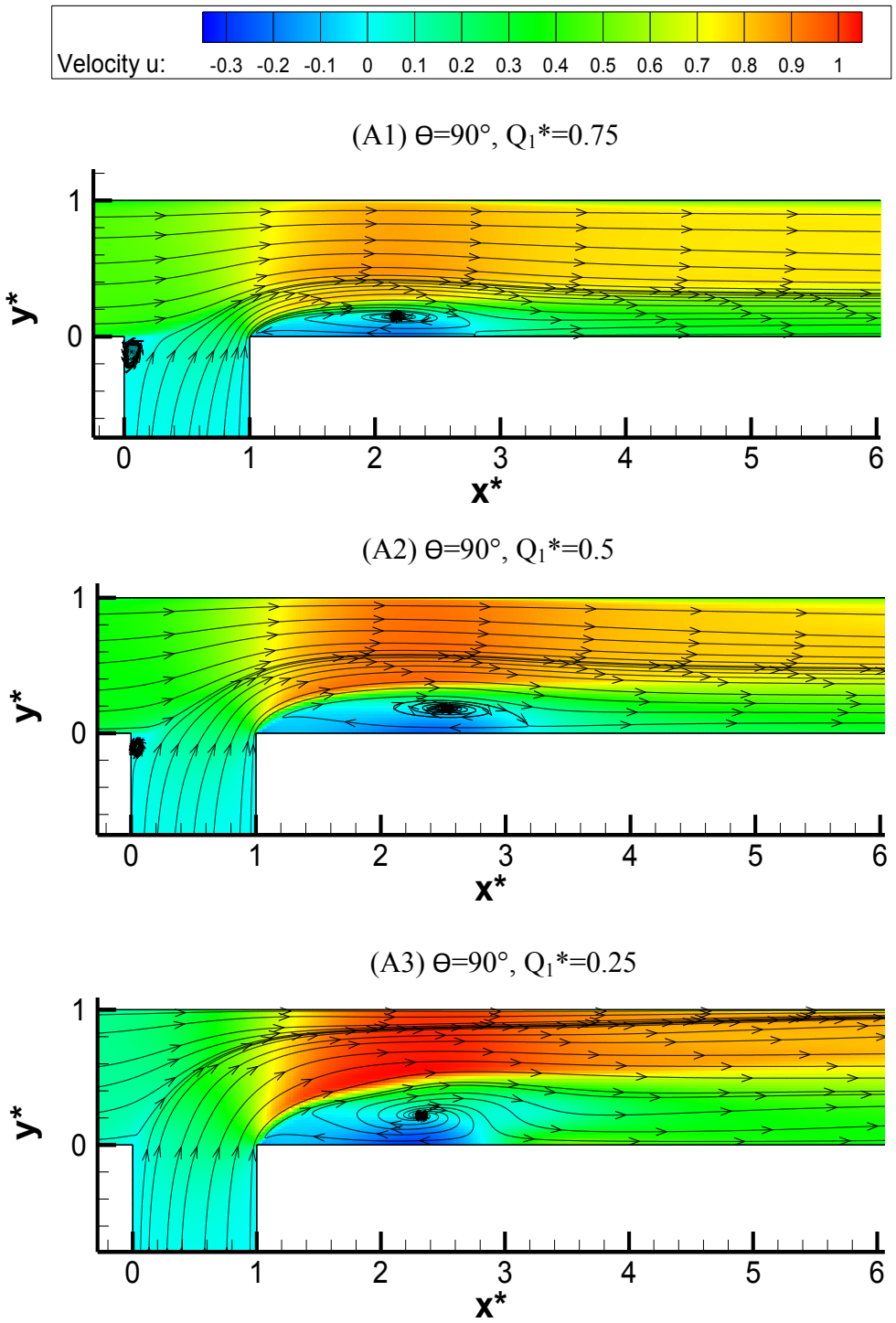

Figure 4-1: Plane view of longitudinal velocity u contours and streamlines for different discharge ratios at 90°-angled confluences at z=0.15m

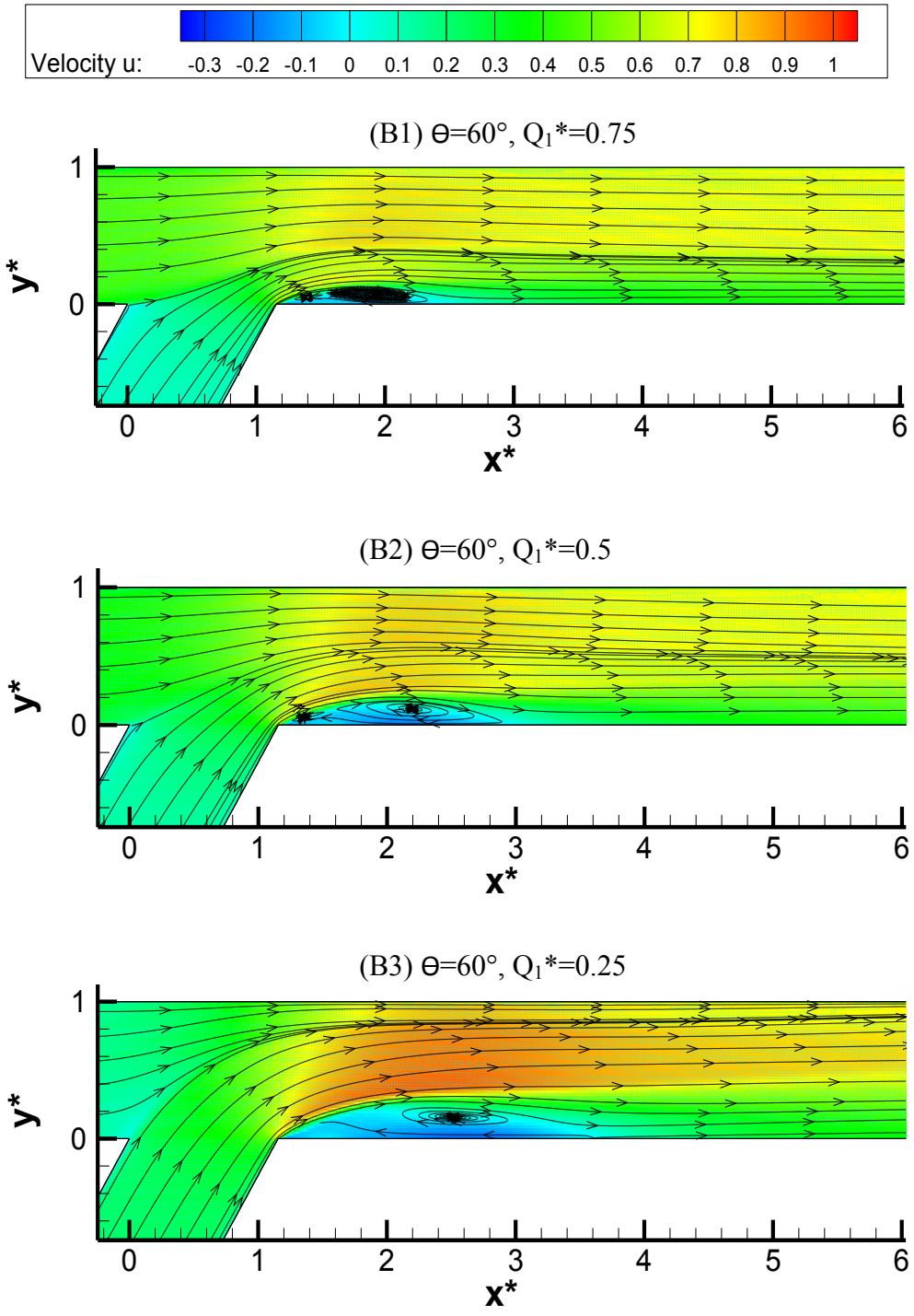

Figure 4-2: Plane view of longitudinal velocity u contours and streamlines for different discharge ratios at 60°-angled confluence at z=0.15m

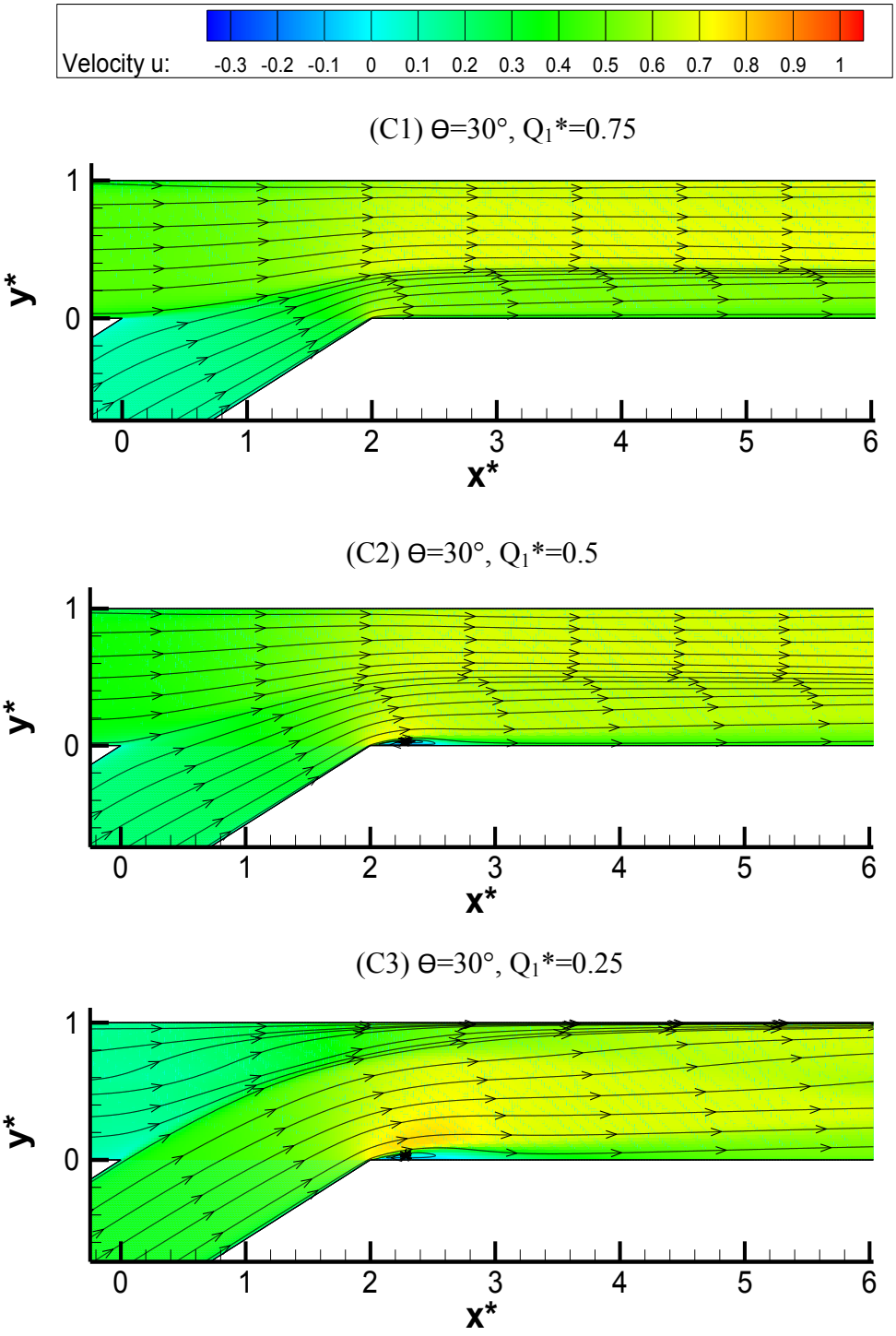

Figure 4-3: Plane view of longitudinal velocity u contours and streamlines for different discharge ratios at 30°-angled confluence at z=0.15m

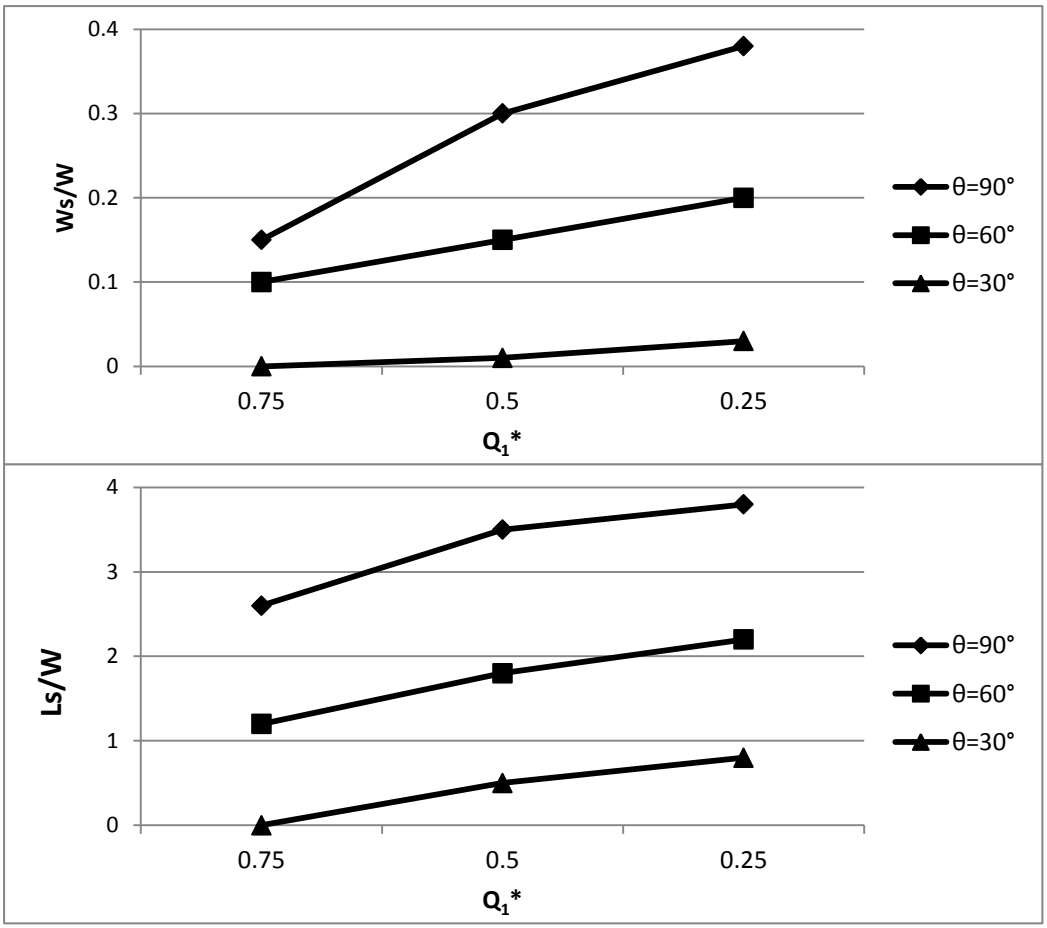

Figure 4-4: Non-dimensional width W_s and length L_s of separation zone for all nine simulation cases

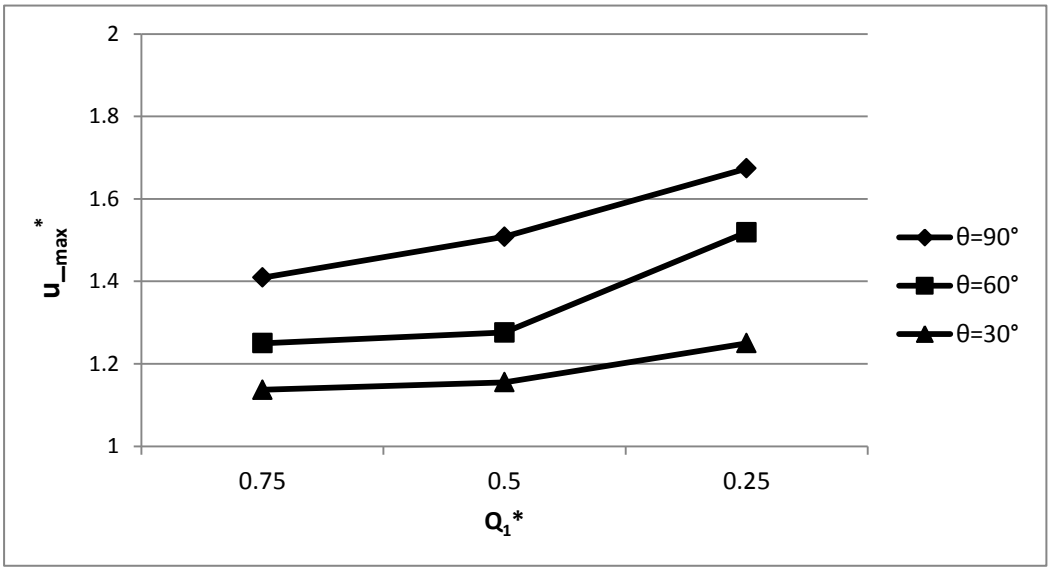

Figure 4-5: Comparison of non-dimensional maximum longitudinal velocities for all nine simulation cases

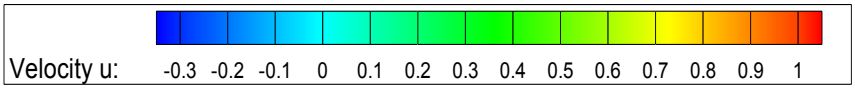

(A1) Θ=90°, Q_1*=0.75

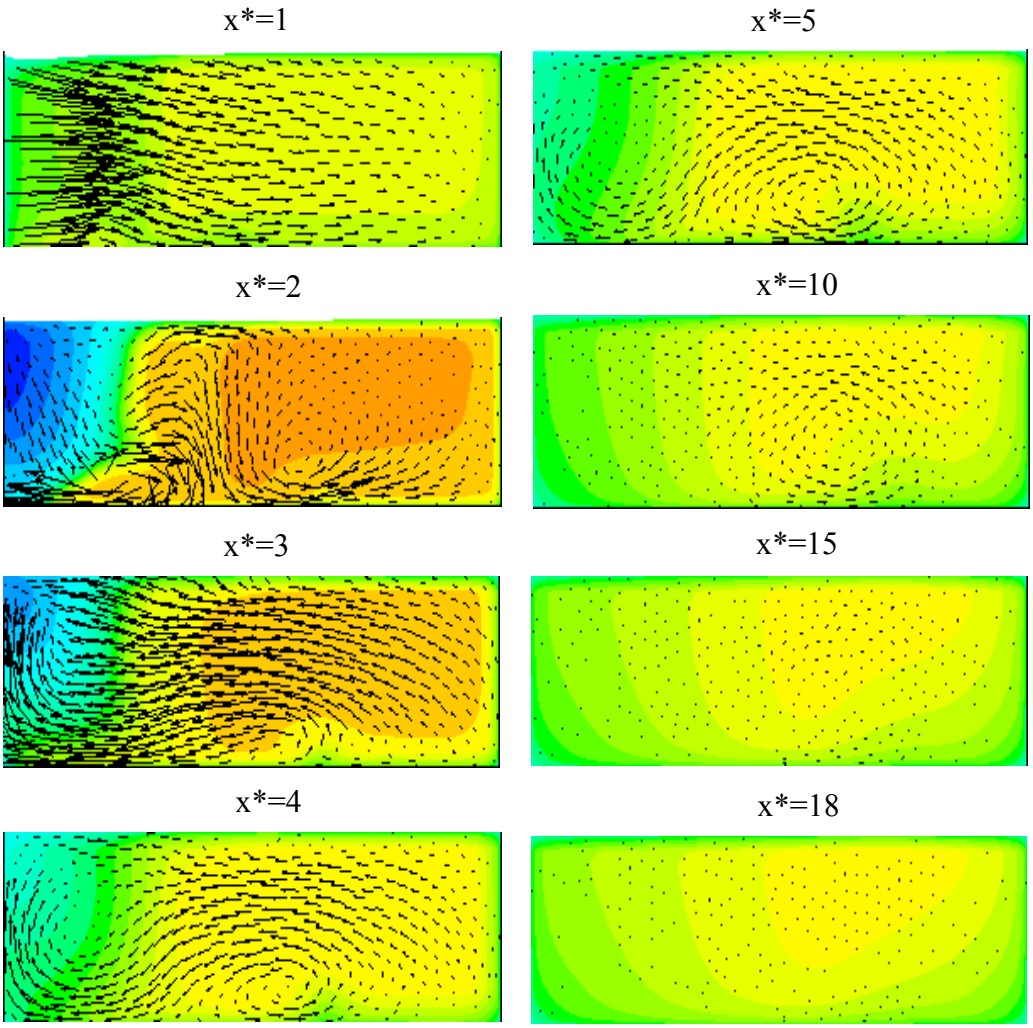

Figure 4-6: Eight cross sections showing secondary currents and streamwise flow contour for case A1

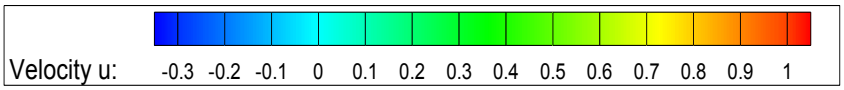

(A2) Θ=90°, Q_1*=0.5

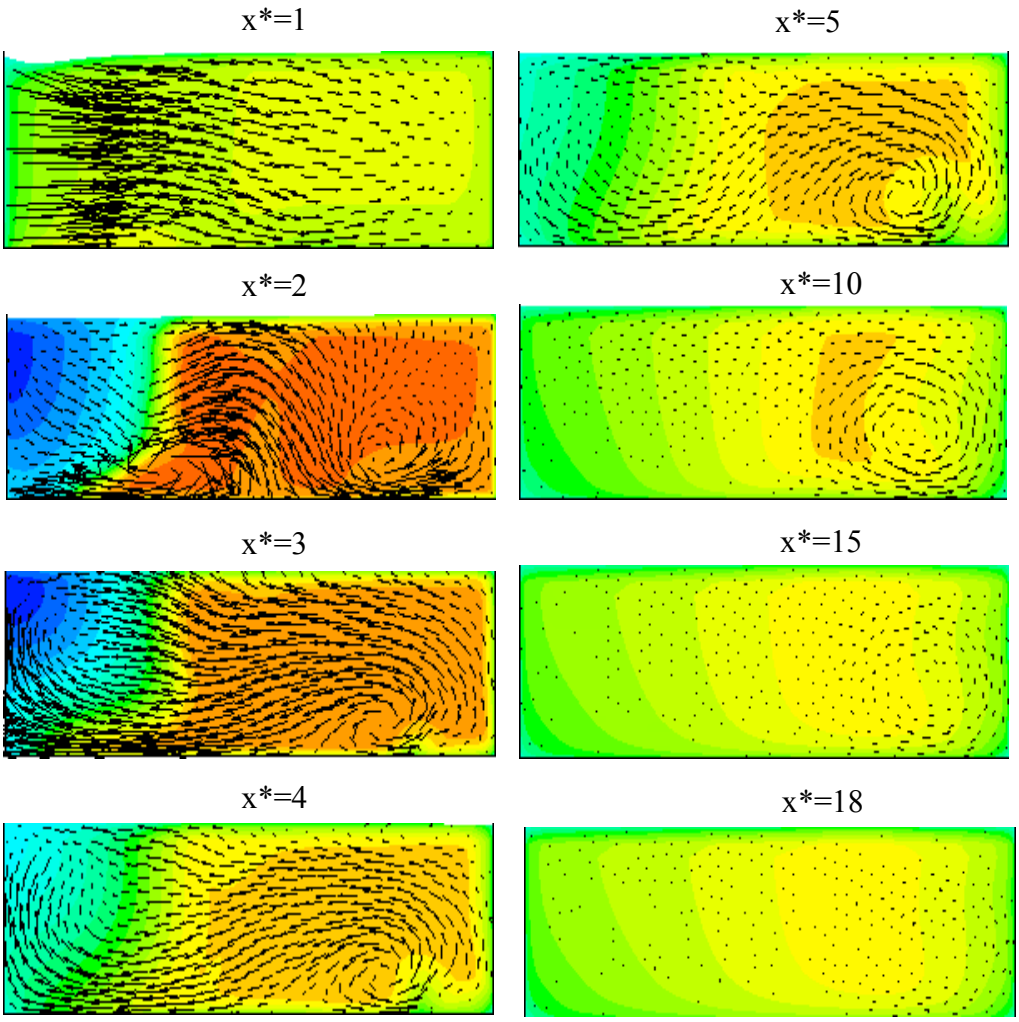

Figure 4-7: Eight cross sections showing secondary currents and streamwise flow contour for case A2

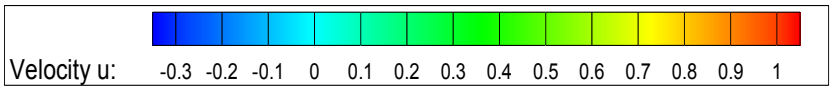

(A3) Θ=90°, Q_1*=0.25

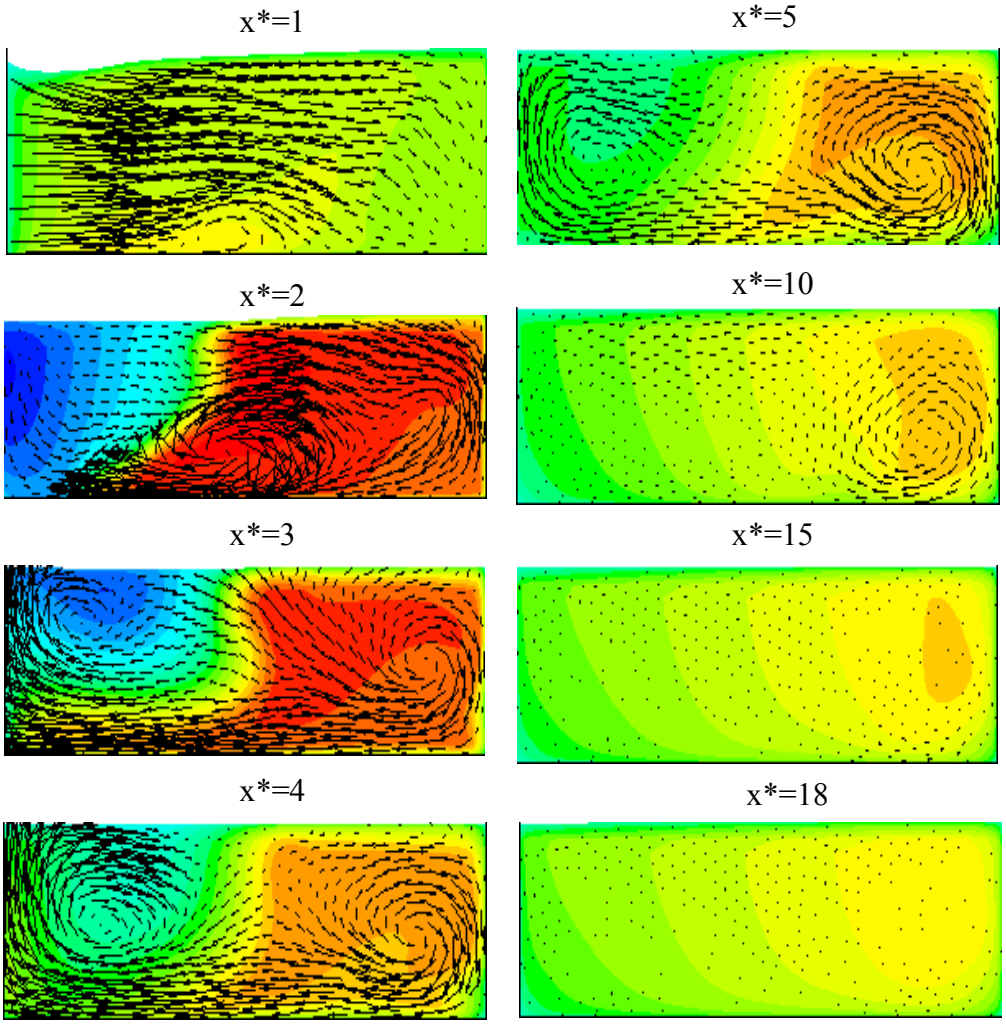

Figure 4-8: Eight cross sections showing secondary currents and streamwise flow contour for case A3

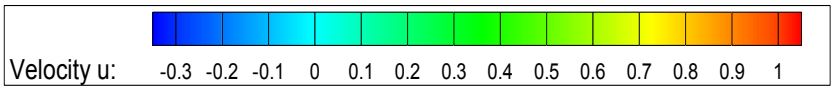

(B1) Θ=60°, Q_1*=0.75

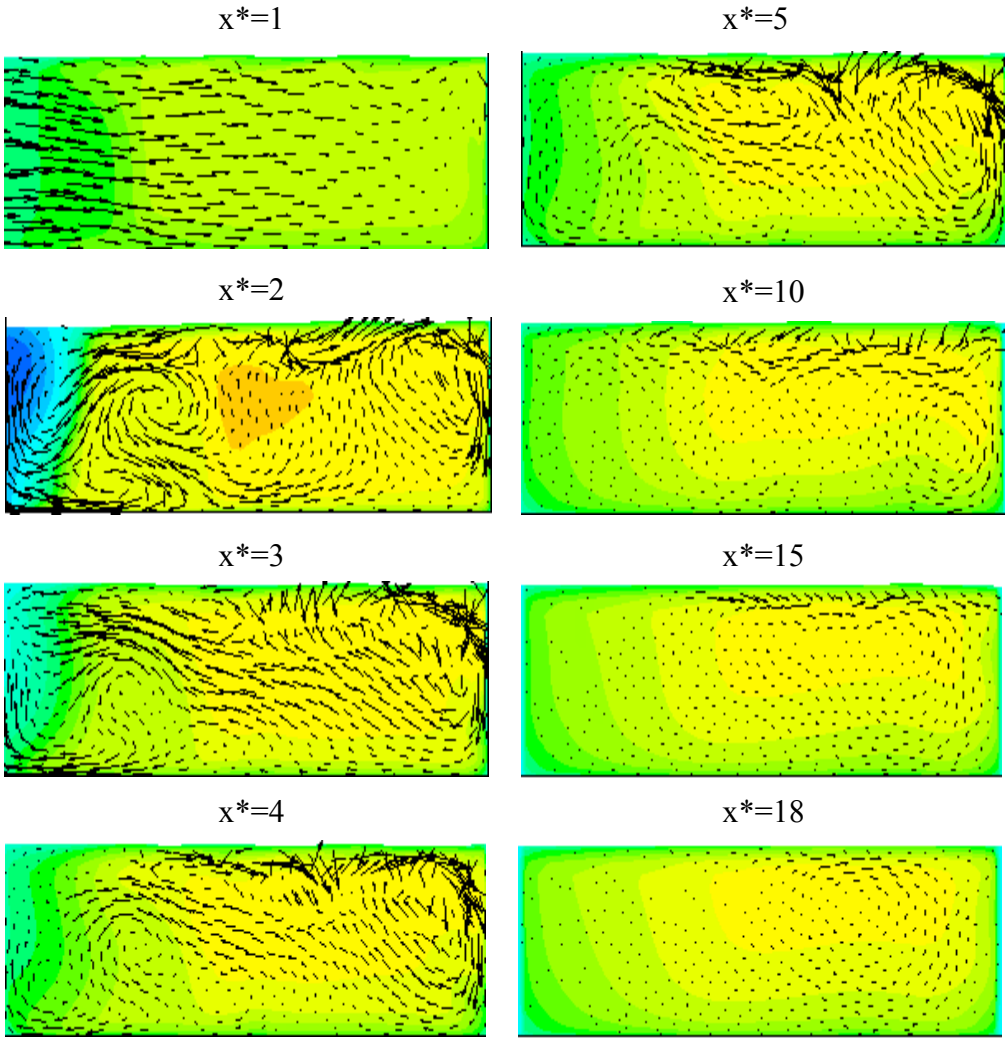

Figure 4-9: Eight cross sections showing secondary currents and streamwise flow contour for case B1

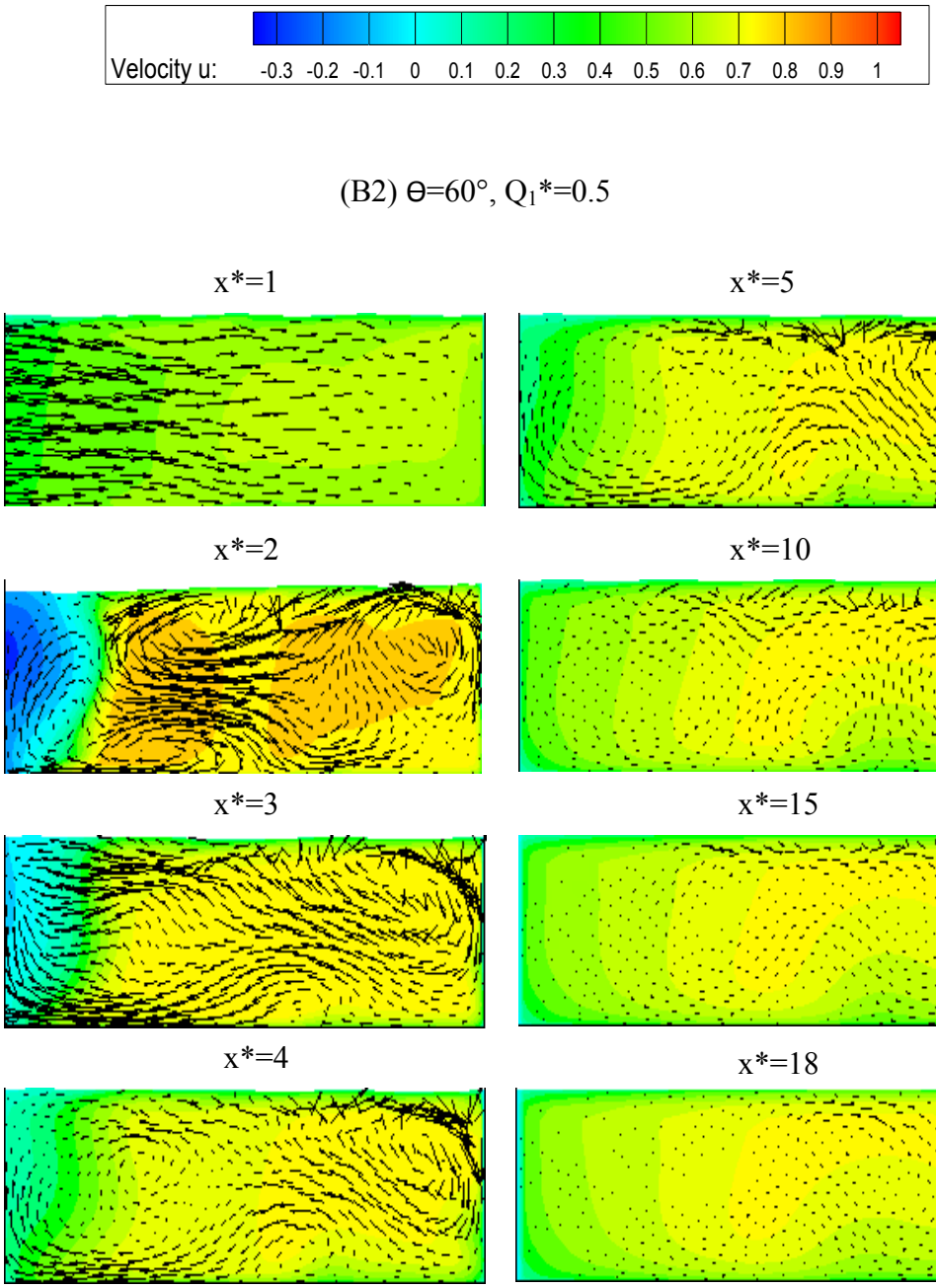

Figure 4-10: Eight cross sections showing secondary currents and streamwise flow contour for case B2

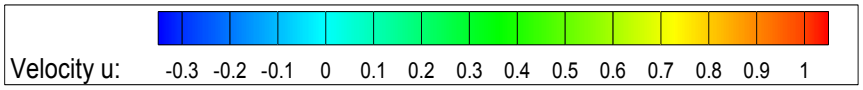

(B3) Θ=60°, Q_1*=0.25

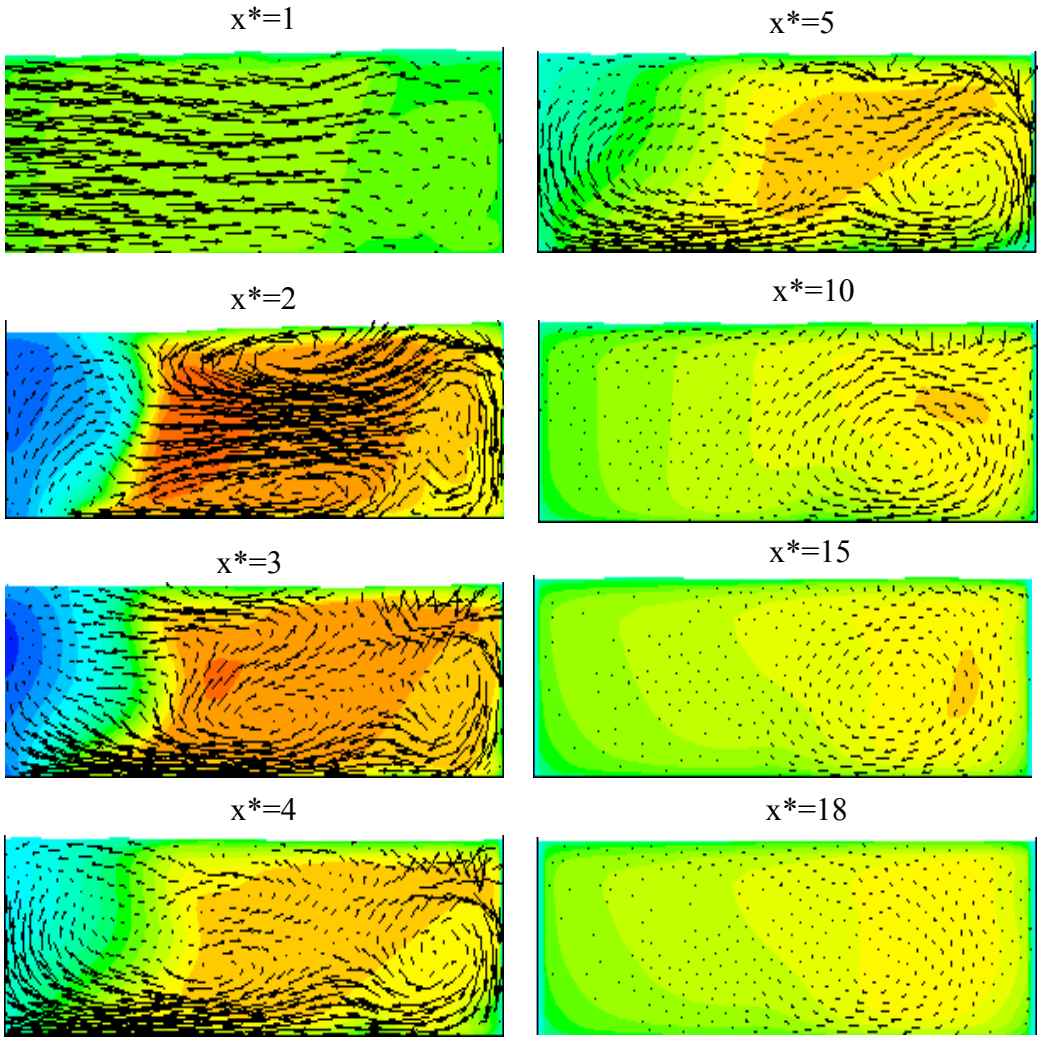

Figure 4-11: Eight cross sections showing secondary currents and streamwise flow contour for case B3

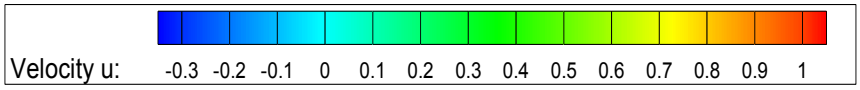

(C1) ϴ=30°, Q_1*=0.75

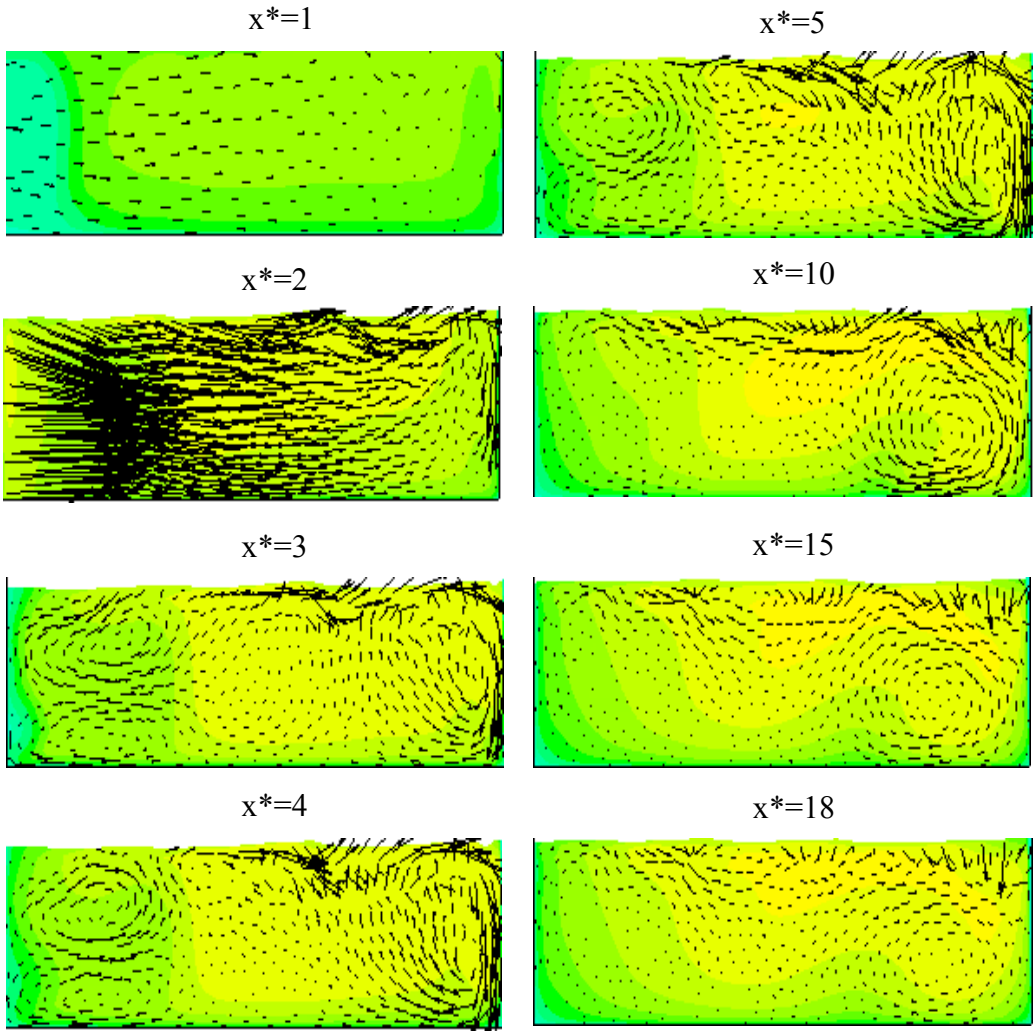

Figure 4-12: Eight cross sections showing secondary currents and streamwise flow contour for case C1

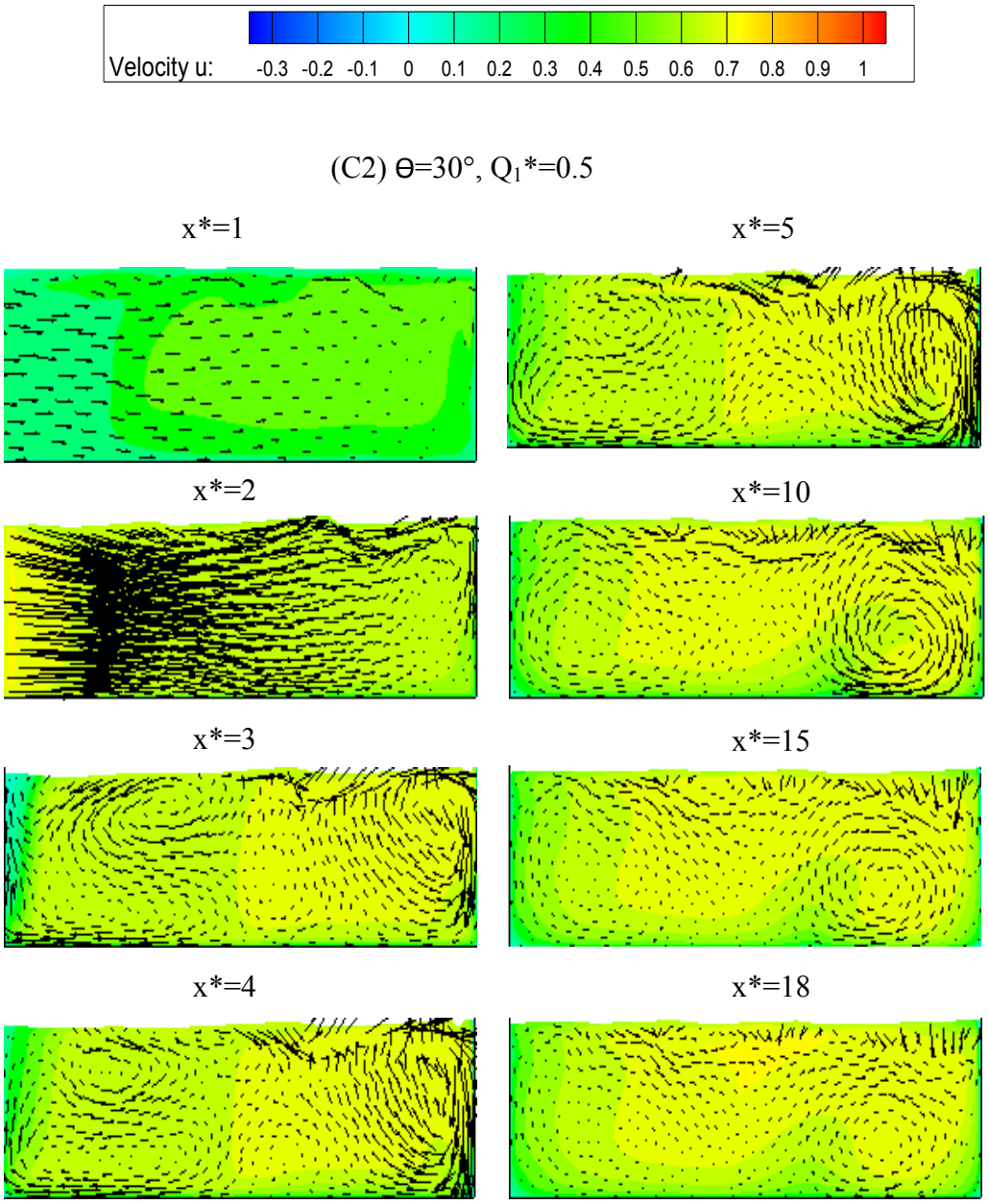

Figure 4-13: Eight cross sections showing secondary currents and streamwise flow contour for case C2

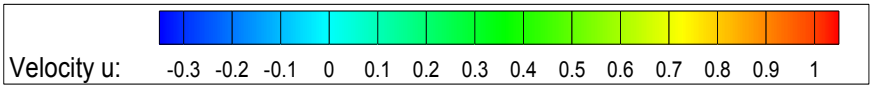

(C3) Θ=30°, Q_1*=0.25

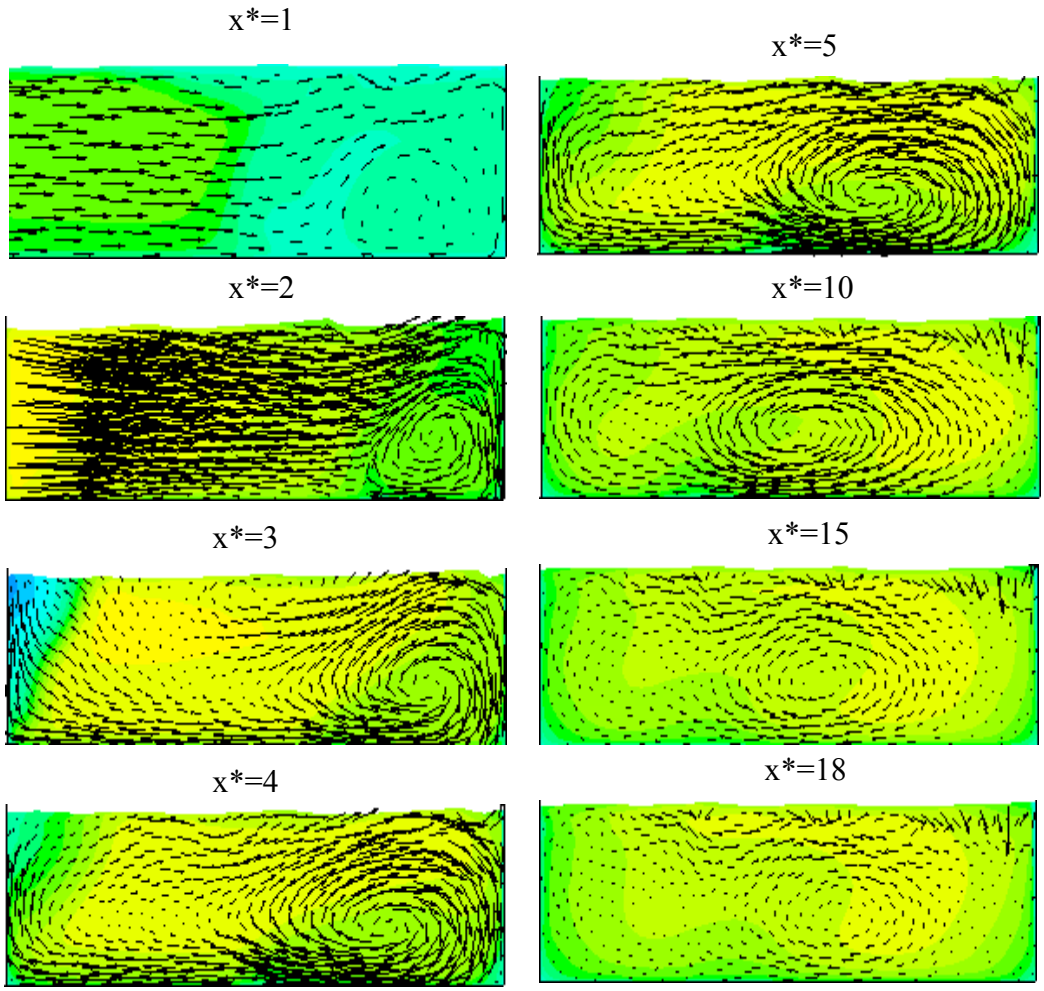

Figure 4-14: Eight cross sections showing secondary currents and streamwise flow contour for case C3

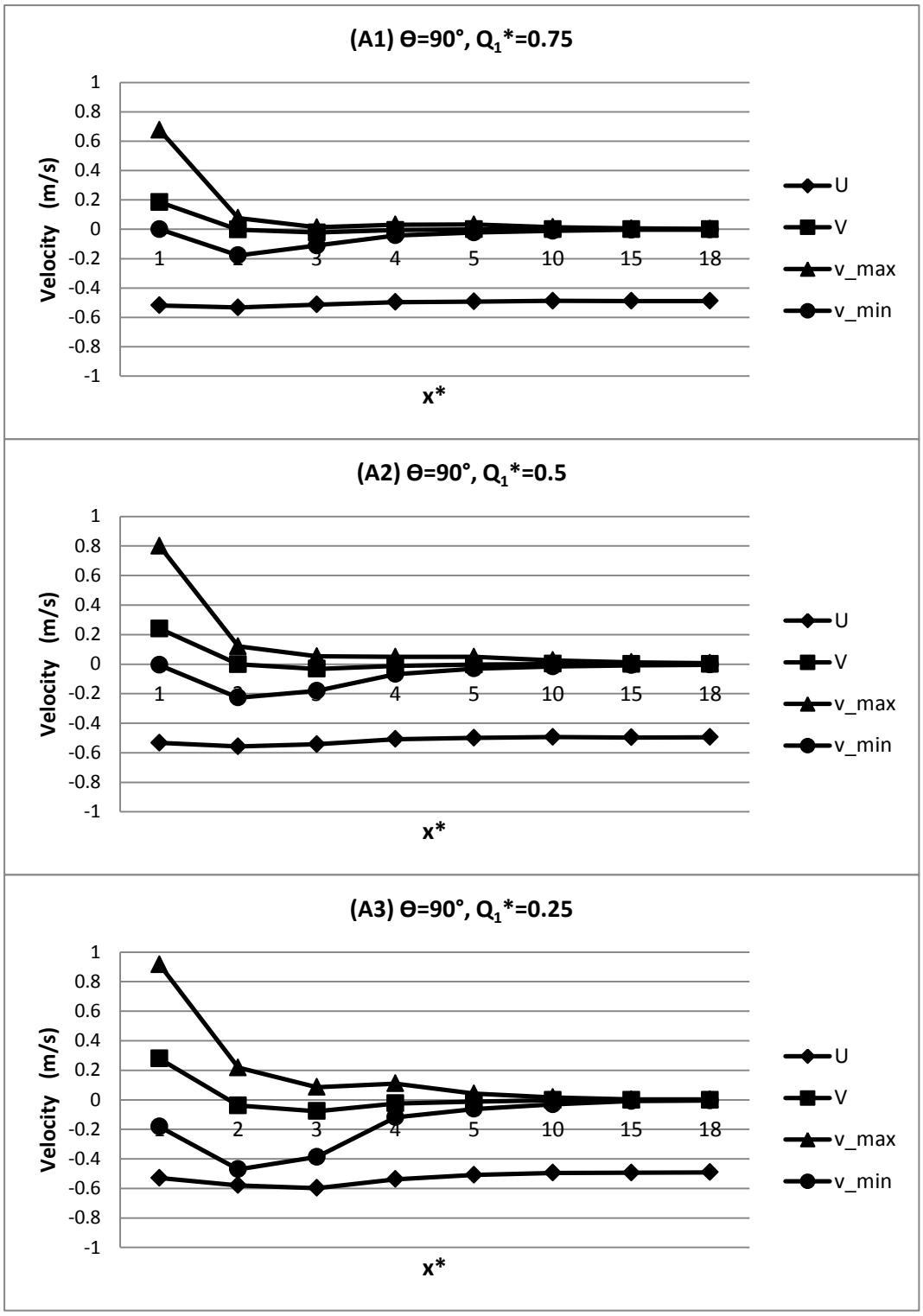

Figure 4-15: Transverse velocities magnitude along the channel for Case A1, A2 and A3

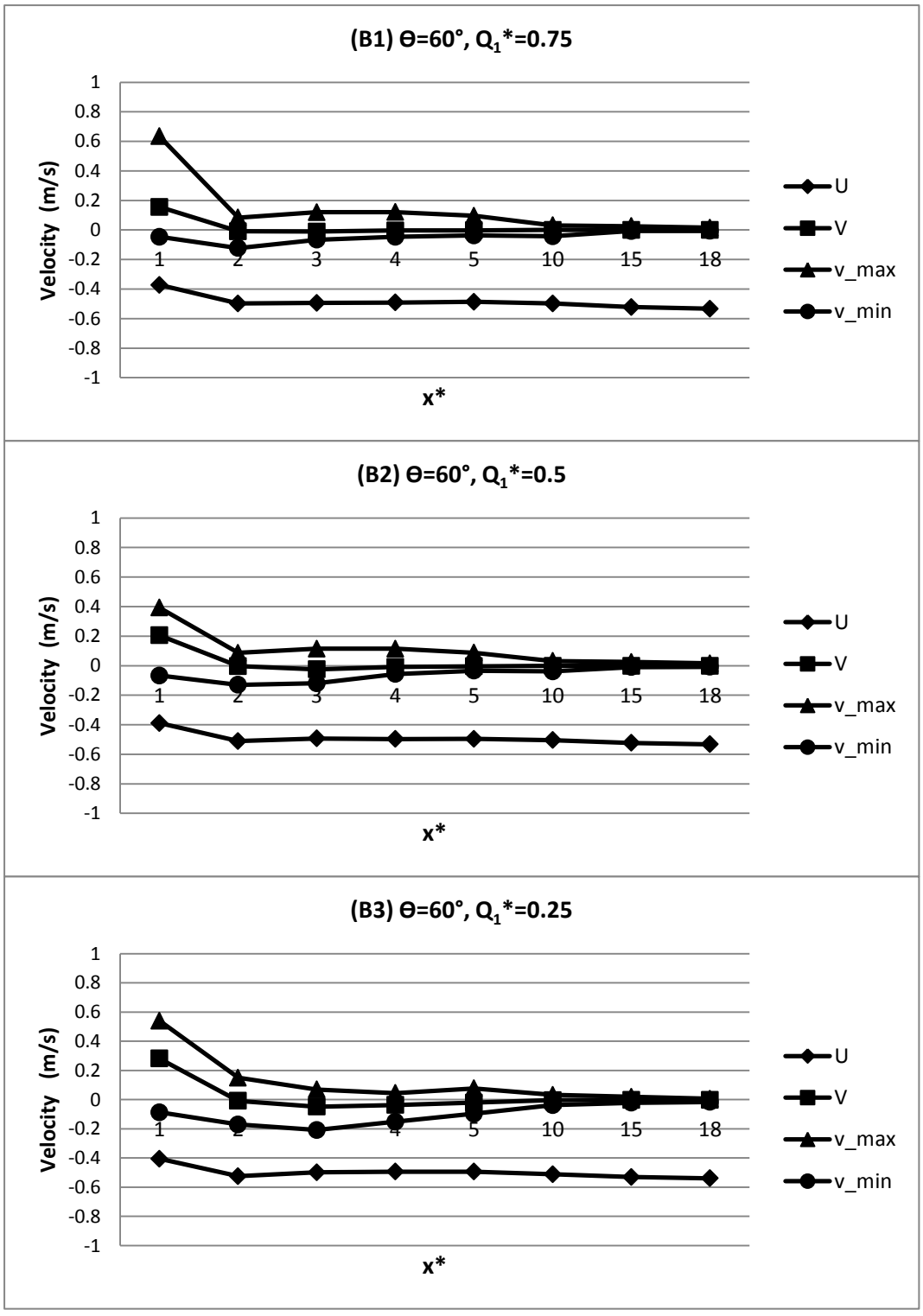

Figure 4-16: Transverse velocities magnitude along the channel for Case B1, B2 and B3

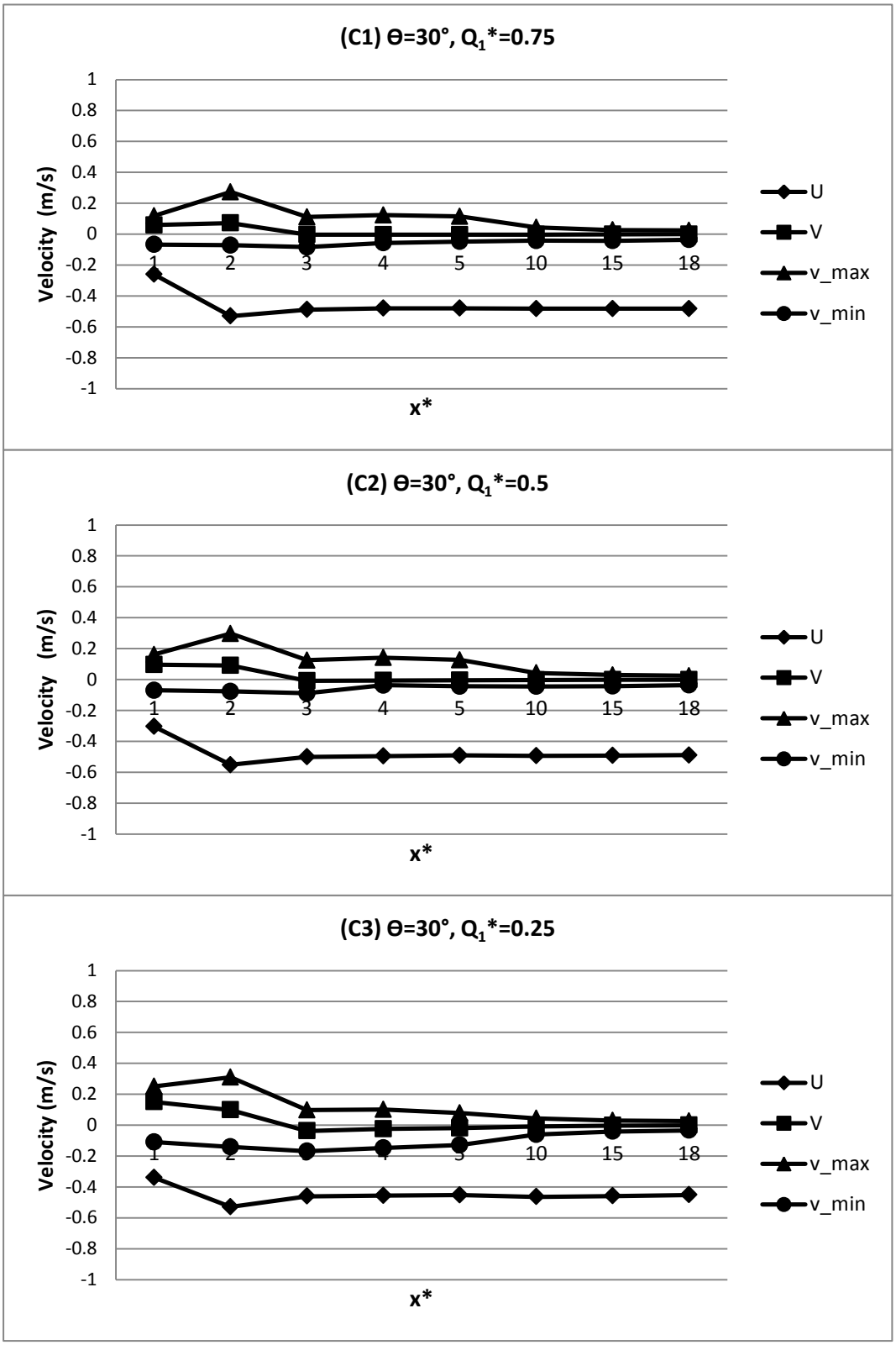

Figure 4-17: Transverse velocities magnitude along the channel for Case C1, C2 and C3

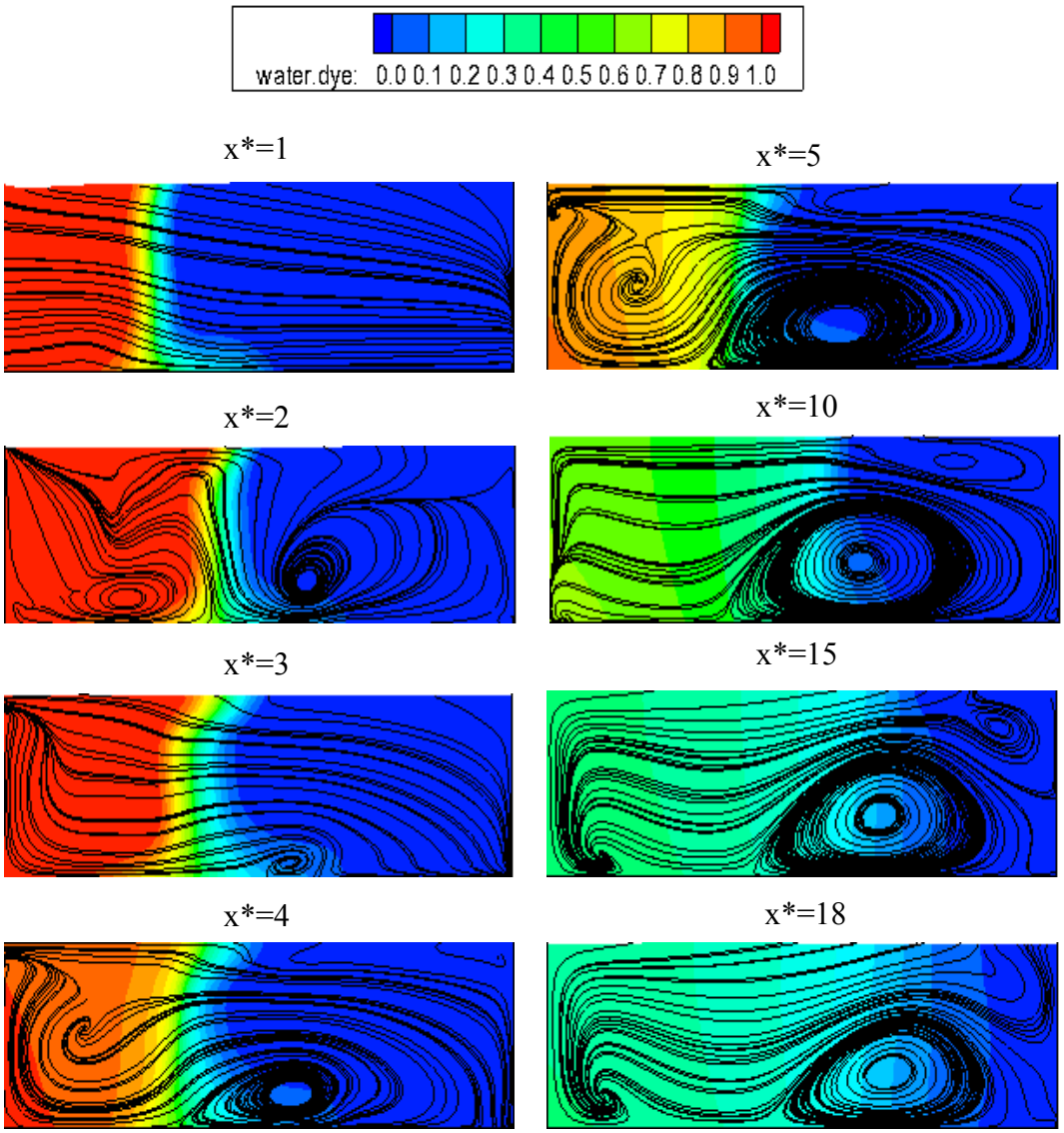

Figure 4-18: Eight cross sections showing water dye concentration with streamlines for case A1

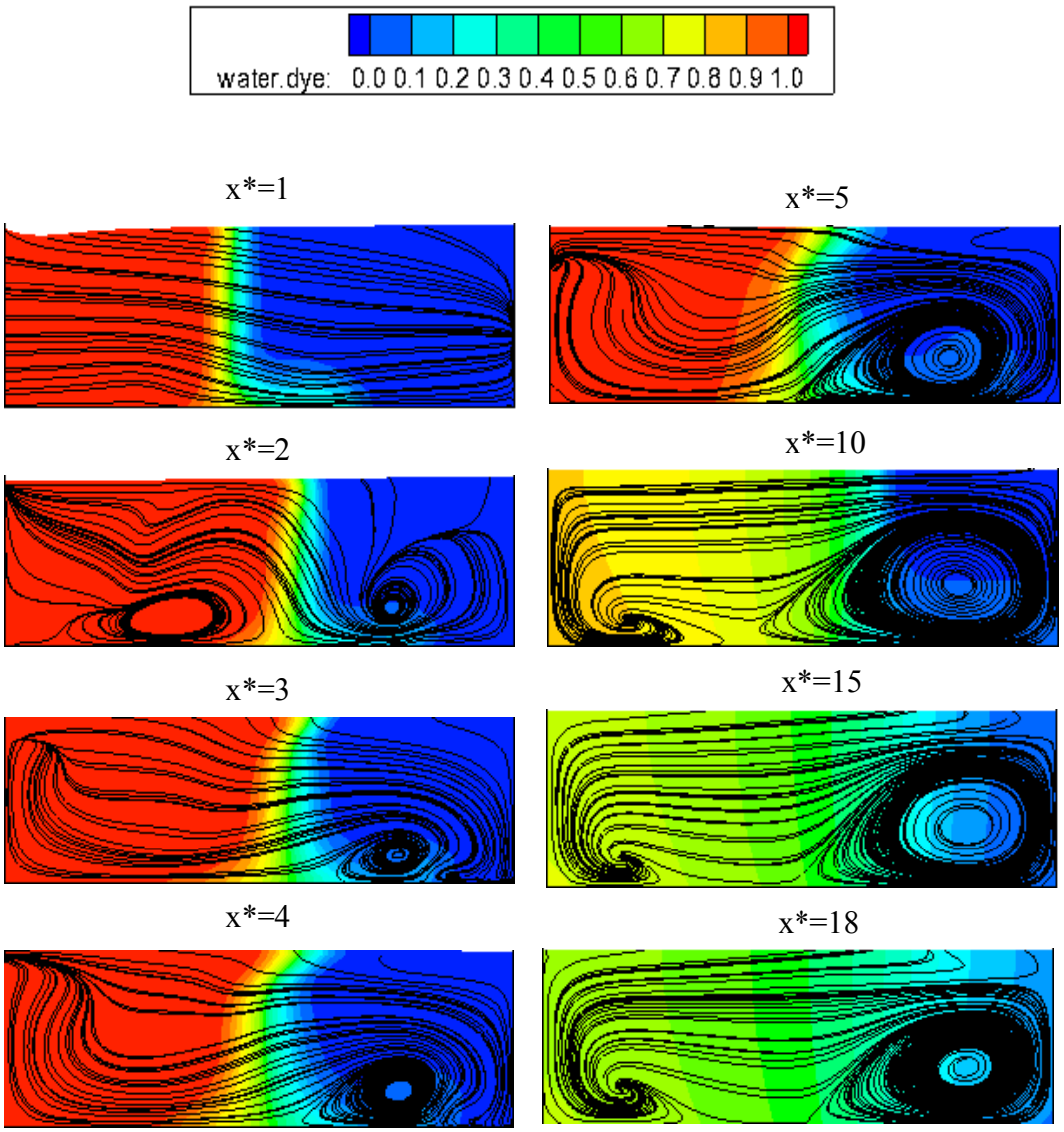

Figure 4-19: Eight cross sections showing water dye concentration with streamlines for case A2

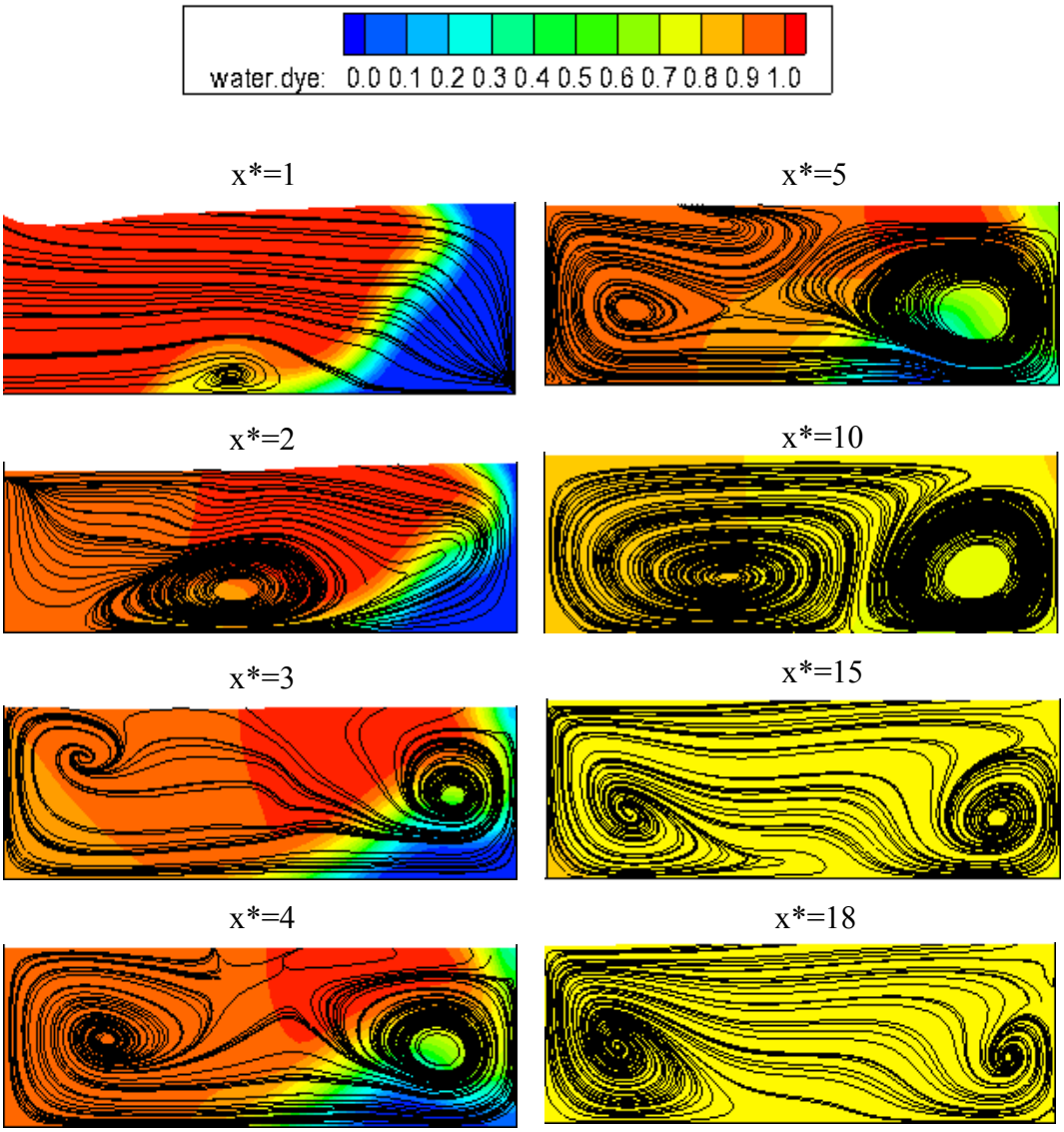

Figure 4-20: Eight cross sections showing water dye concentration with streamlines for case A3

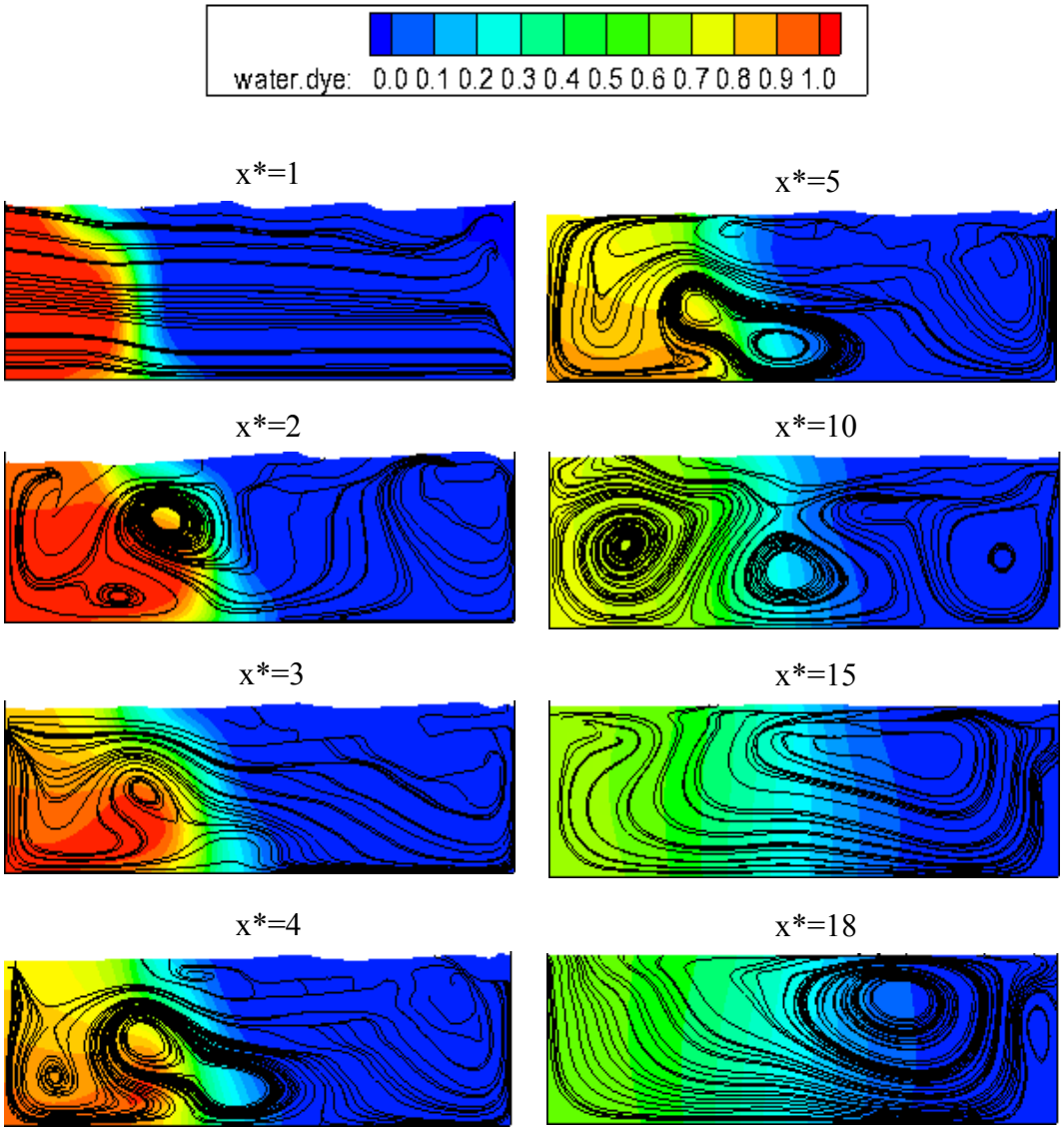

Figure 4-21: Eight cross sections showing water dye concentration with streamlines for case B1

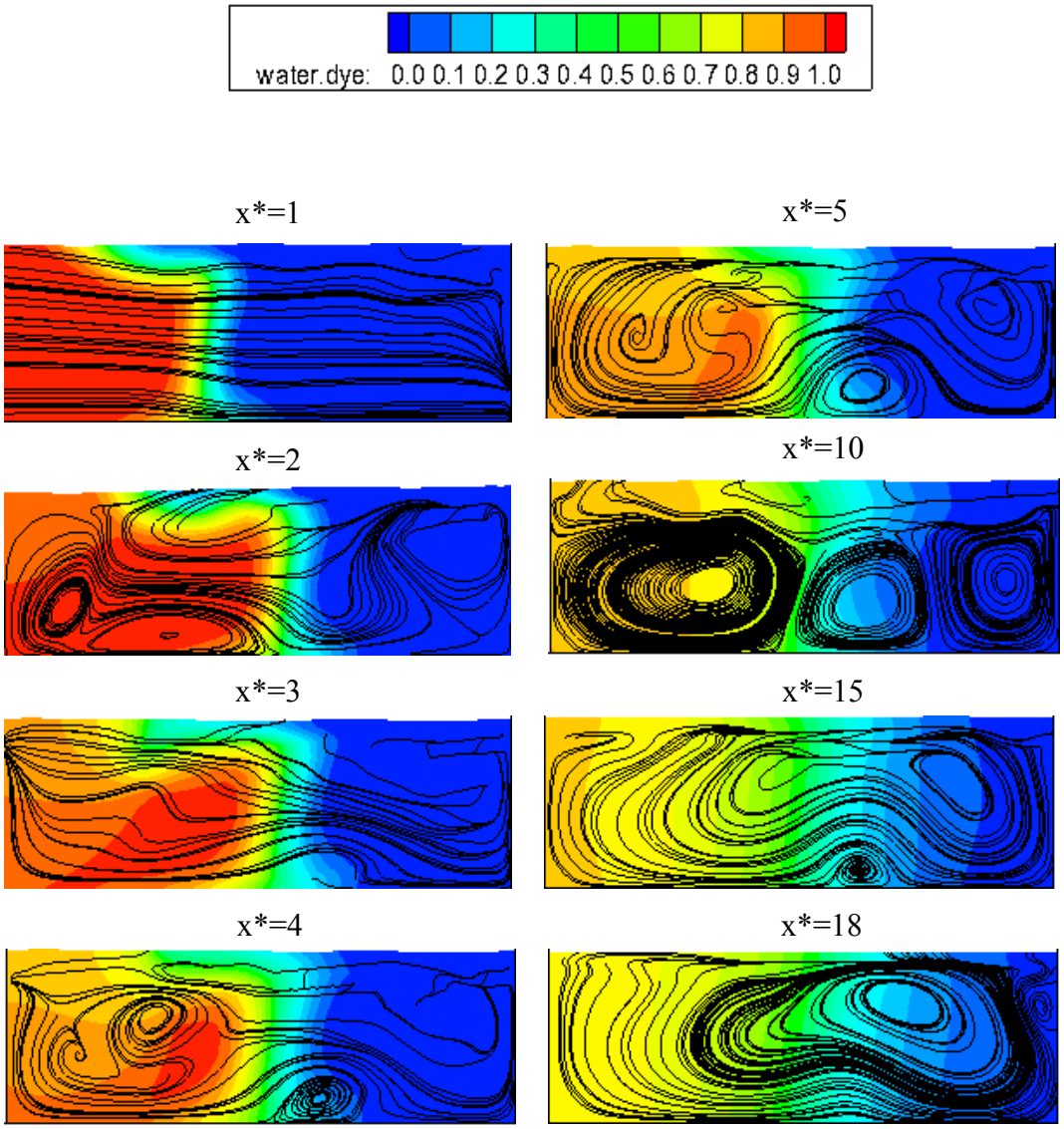

Figure 4-22: Eight cross sections showing water dye concentration with streamlines for case B2

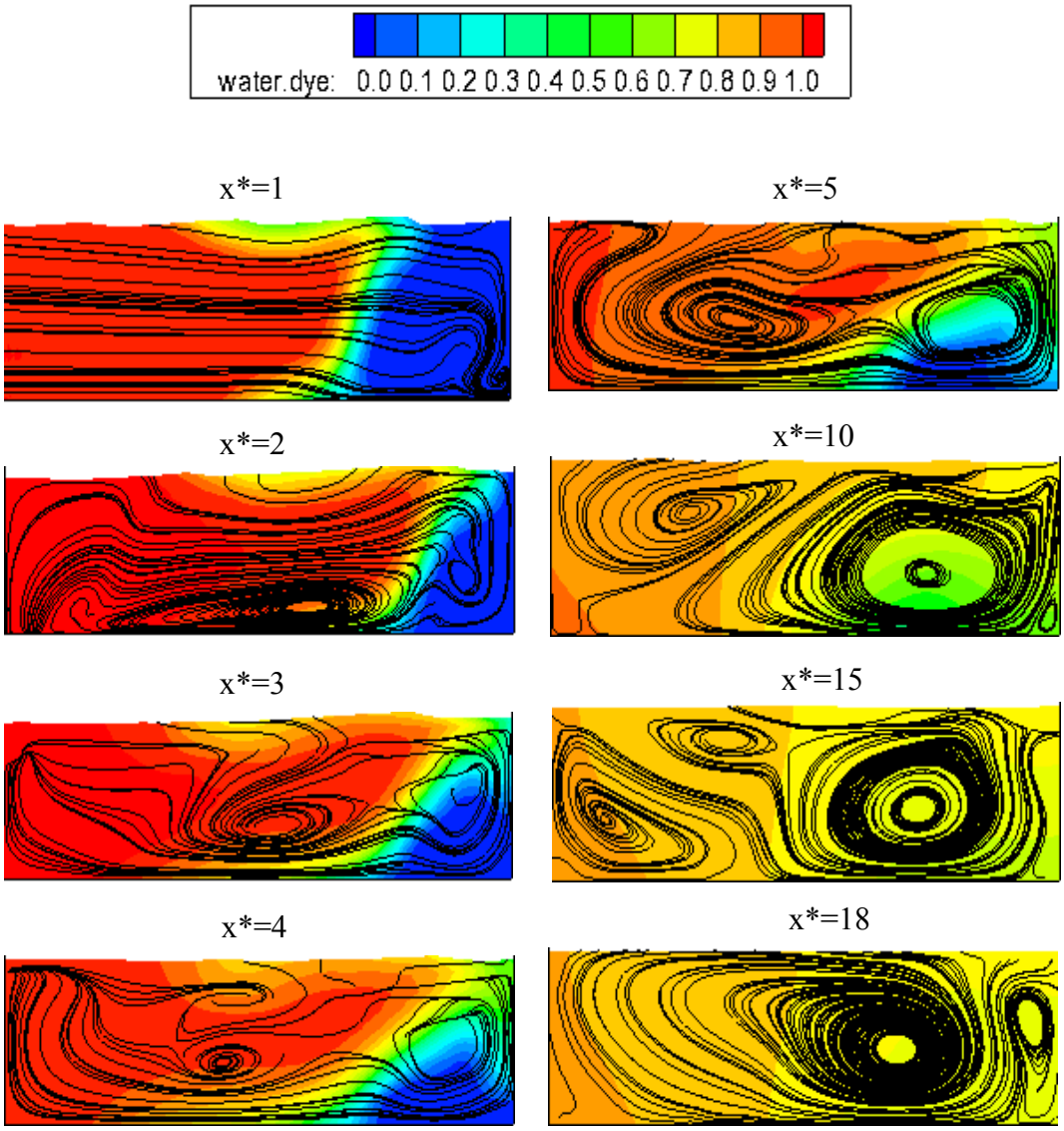

Figure 4-23: Eight cross sections showing water dye concentration with streamlines for case B3

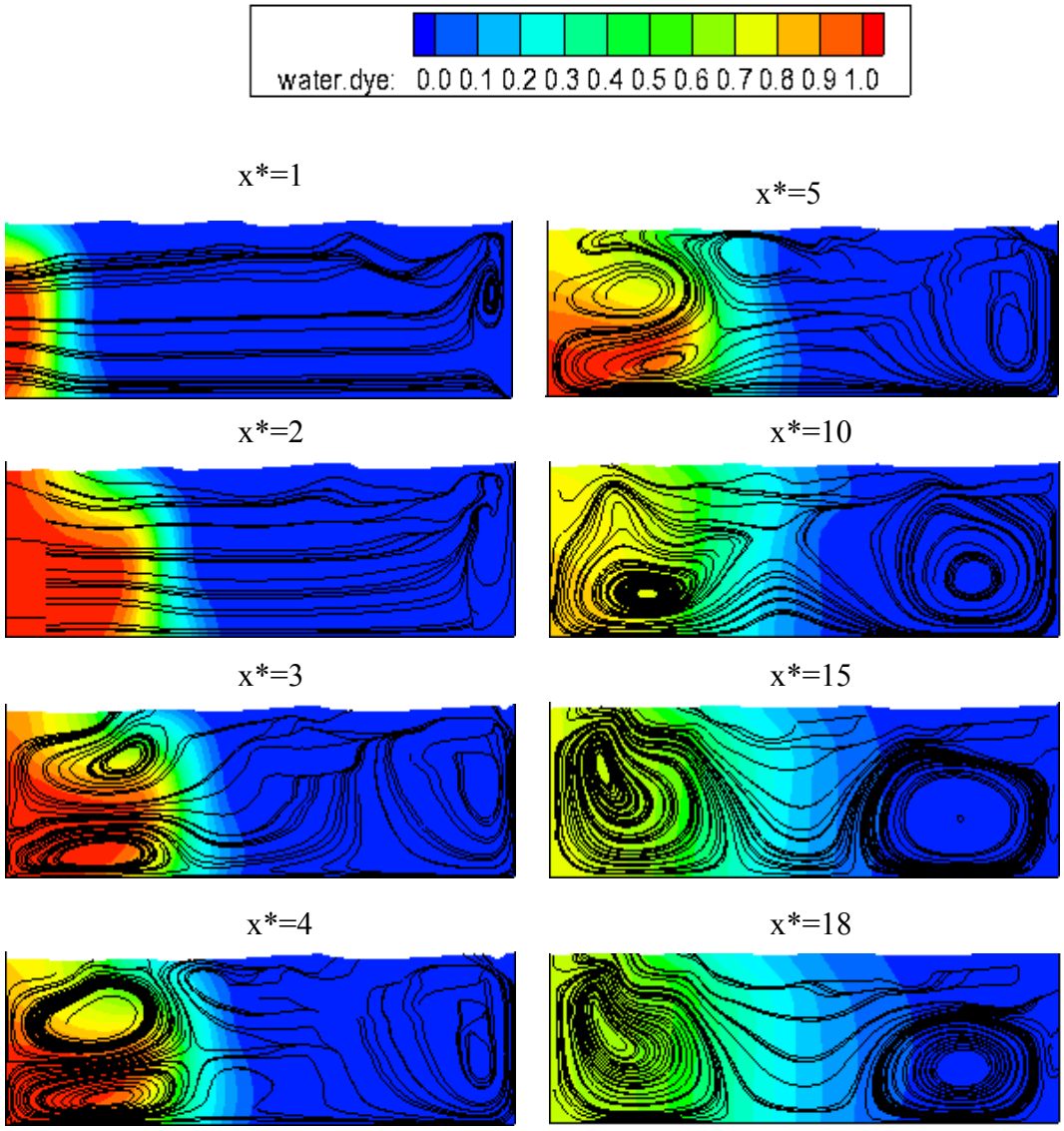

Figure 4-24: Eight cross sections showing water dye concentration with streamlines for case C1

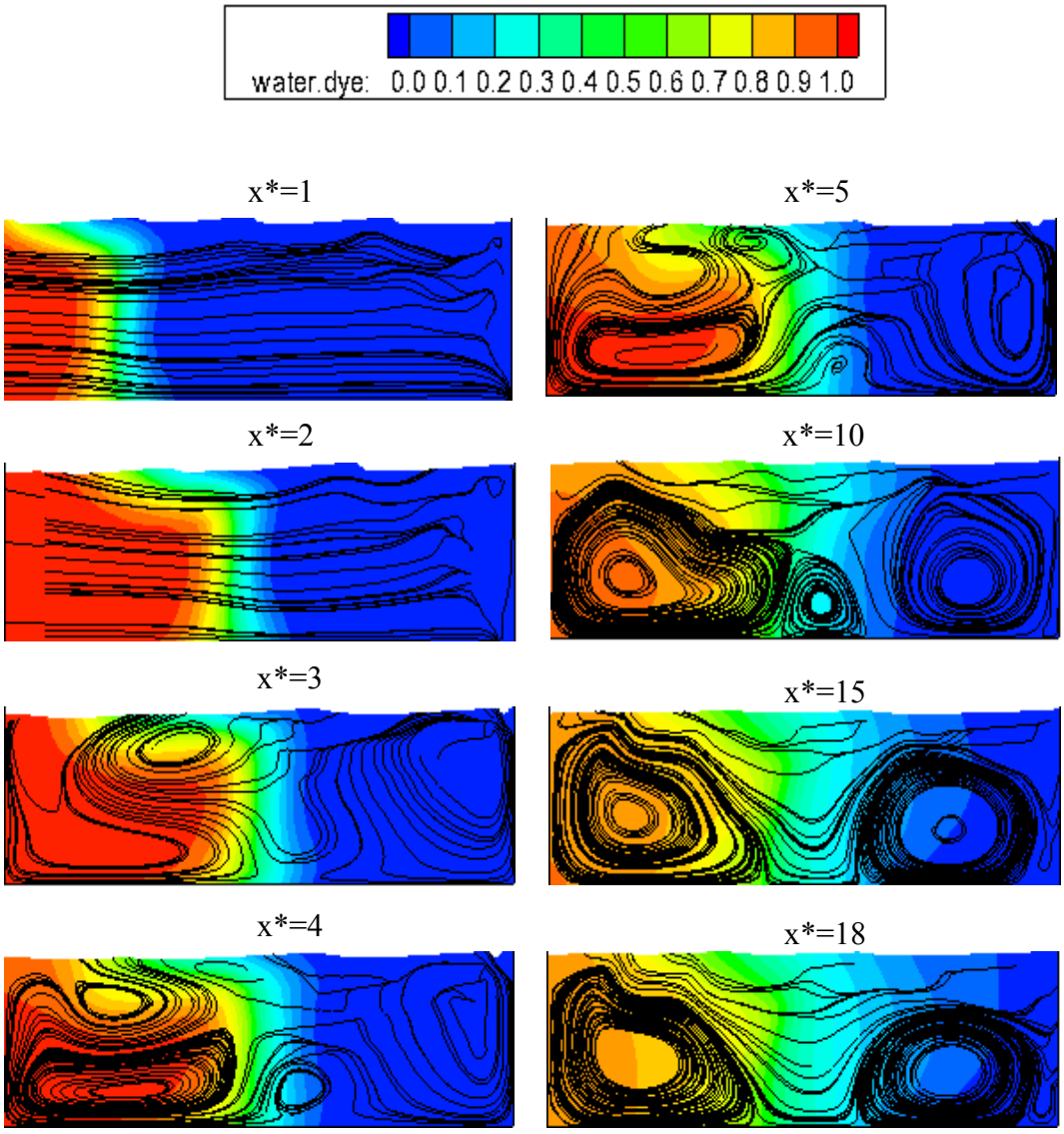

Figure 4-25: Eight cross sections showing water dye concentration with streamlines for case C2

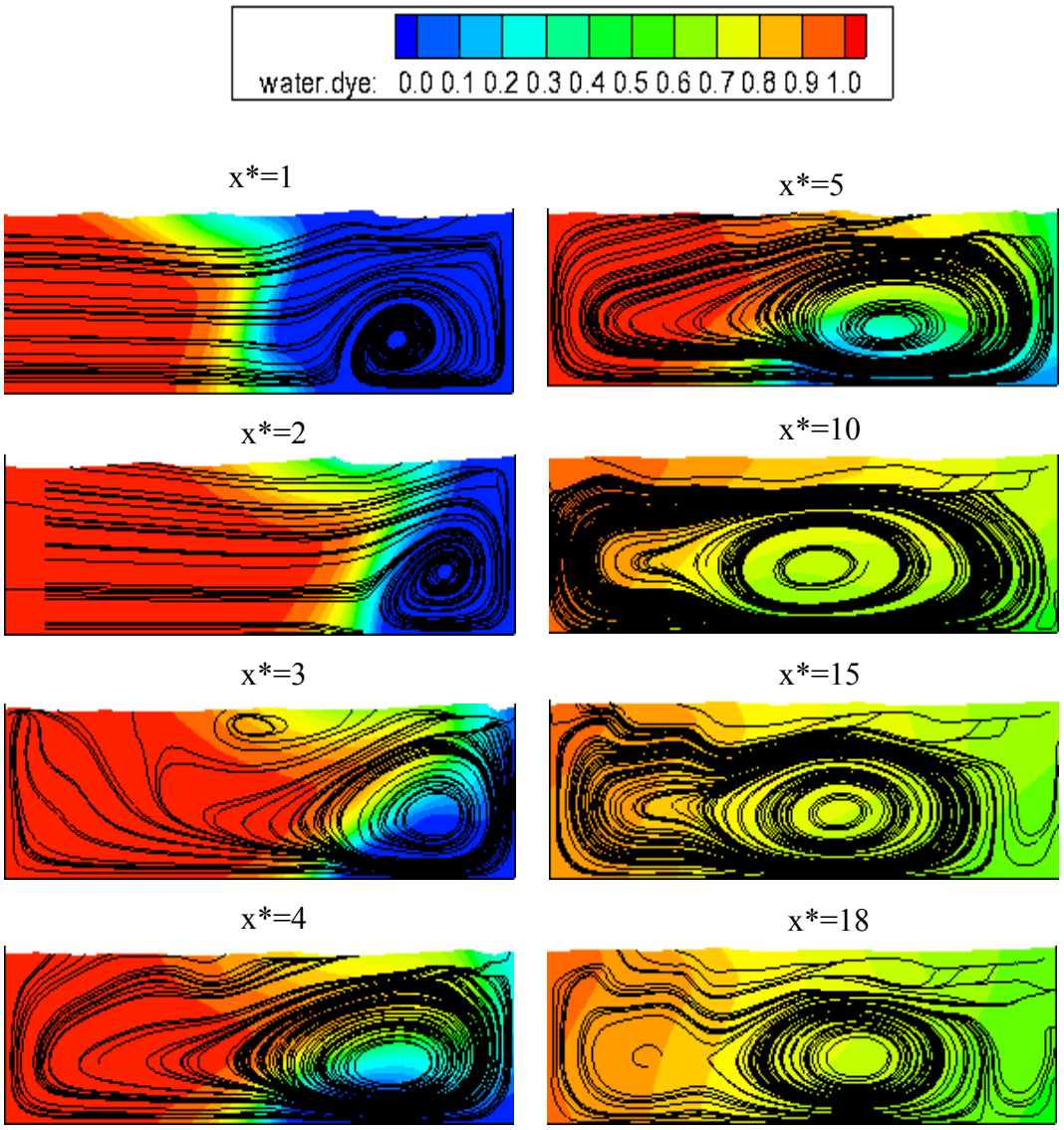

Figure 4-26: Eight cross sections showing water dye concentration with streamlines for case C3

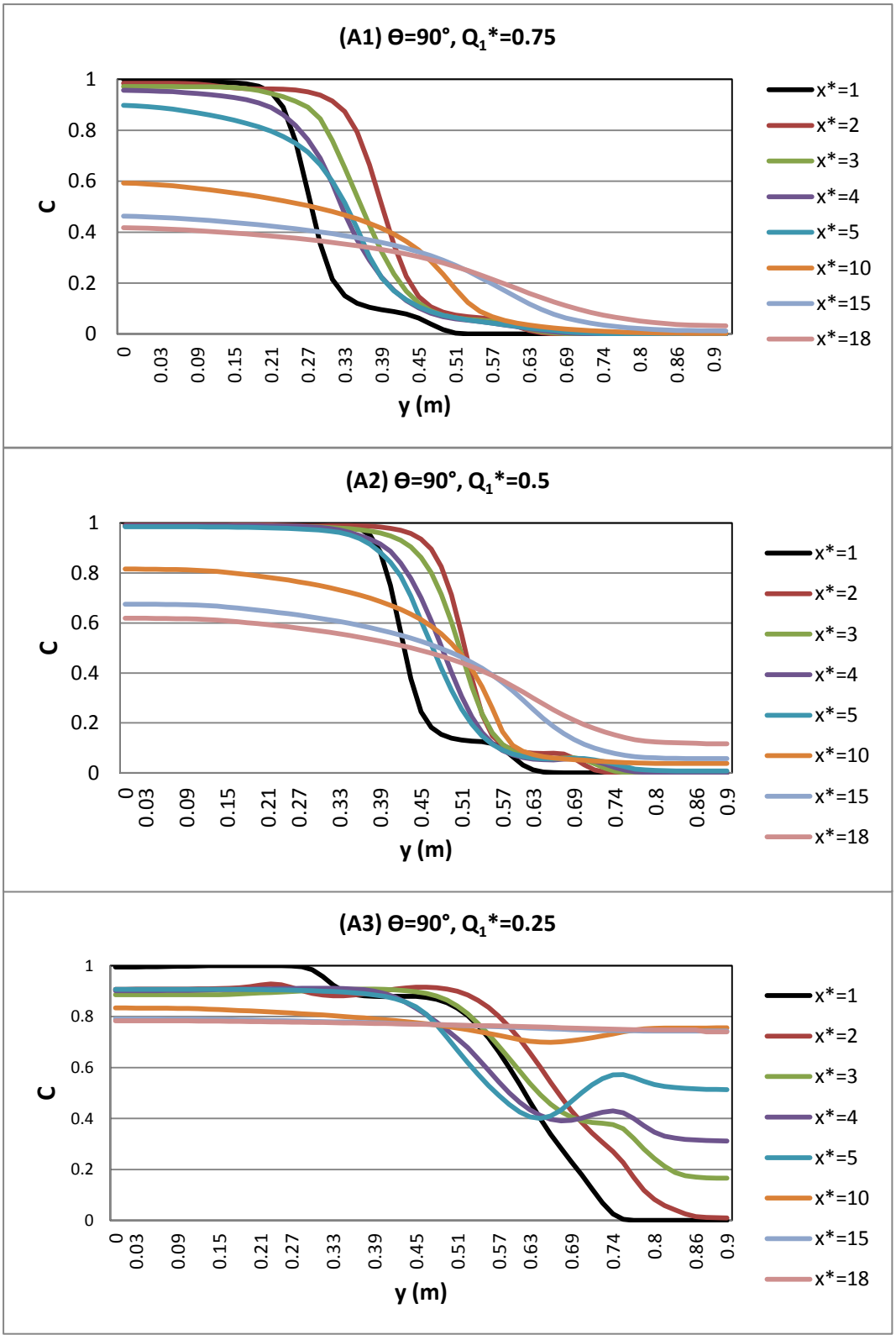

Figure 4-27: Depth averaged dye concentration *C* versus transverse distance at eight cross sections for case A1, A2 and A3

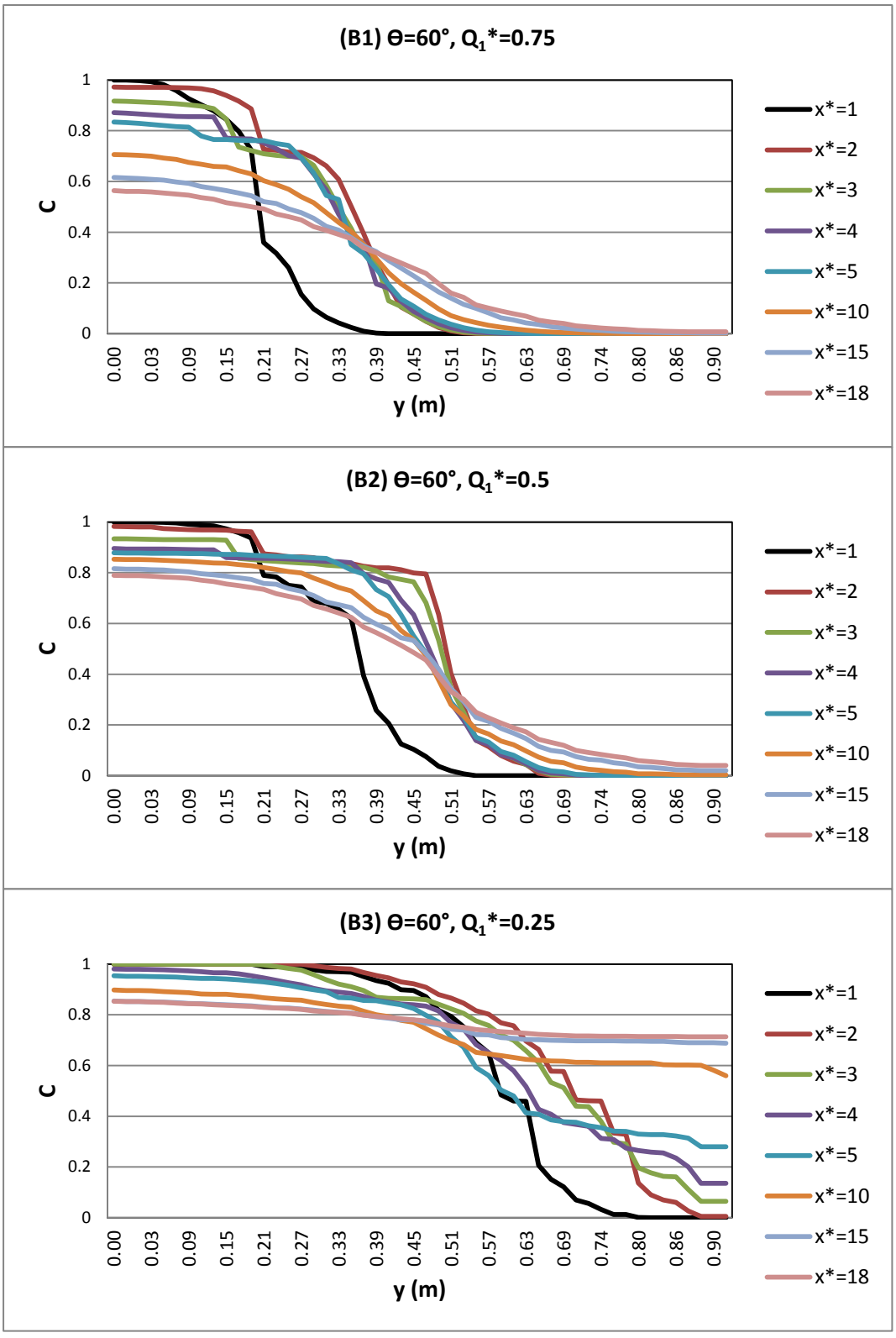

Figure 4-28: Depth averaged dye concentrations versus transverse distance at eight cross sections for case B1, B2 and B3

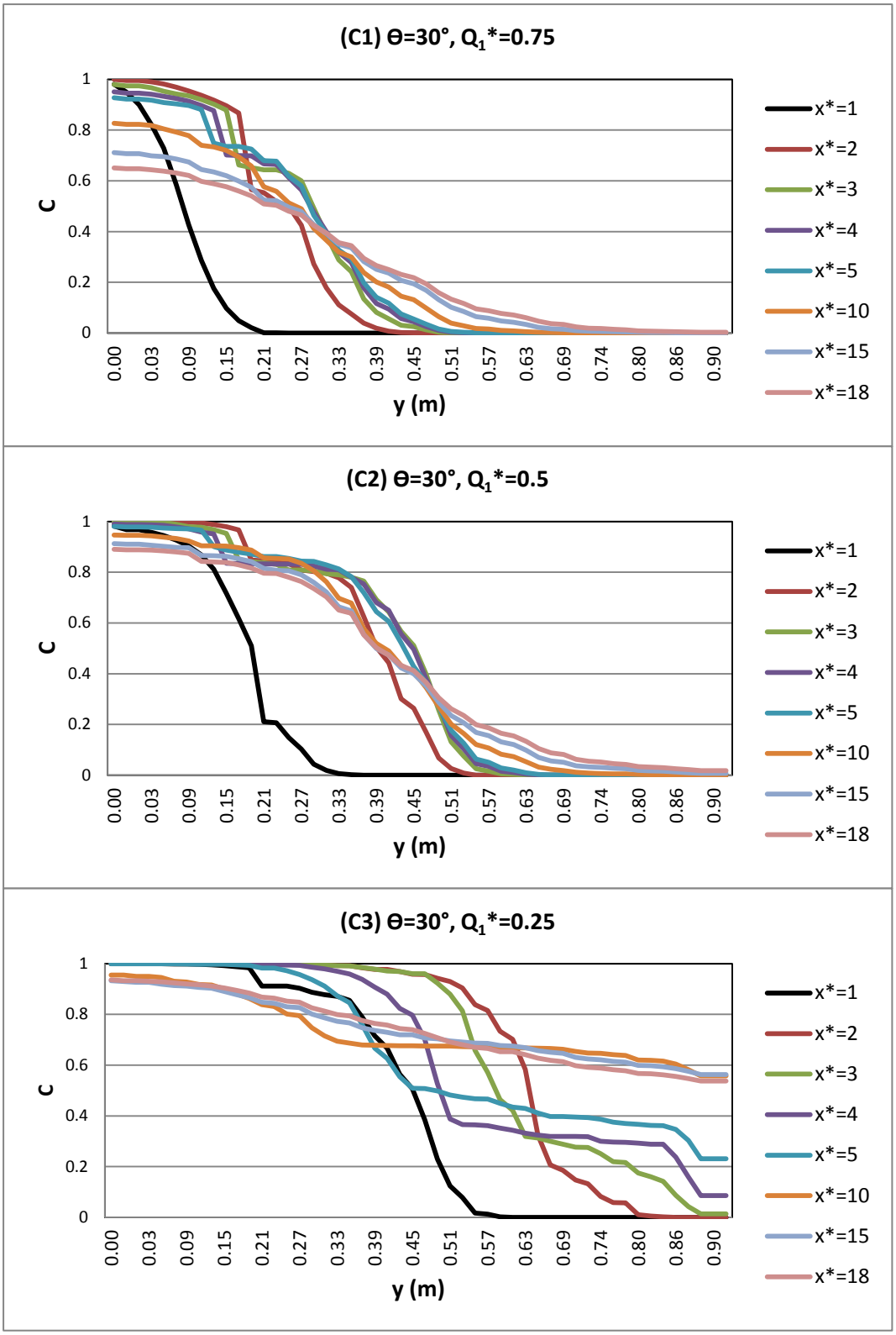

Figure 4-29: Depth averaged dye concentrations versus transverse distance at eight cross sections for case C1, C2 and C3

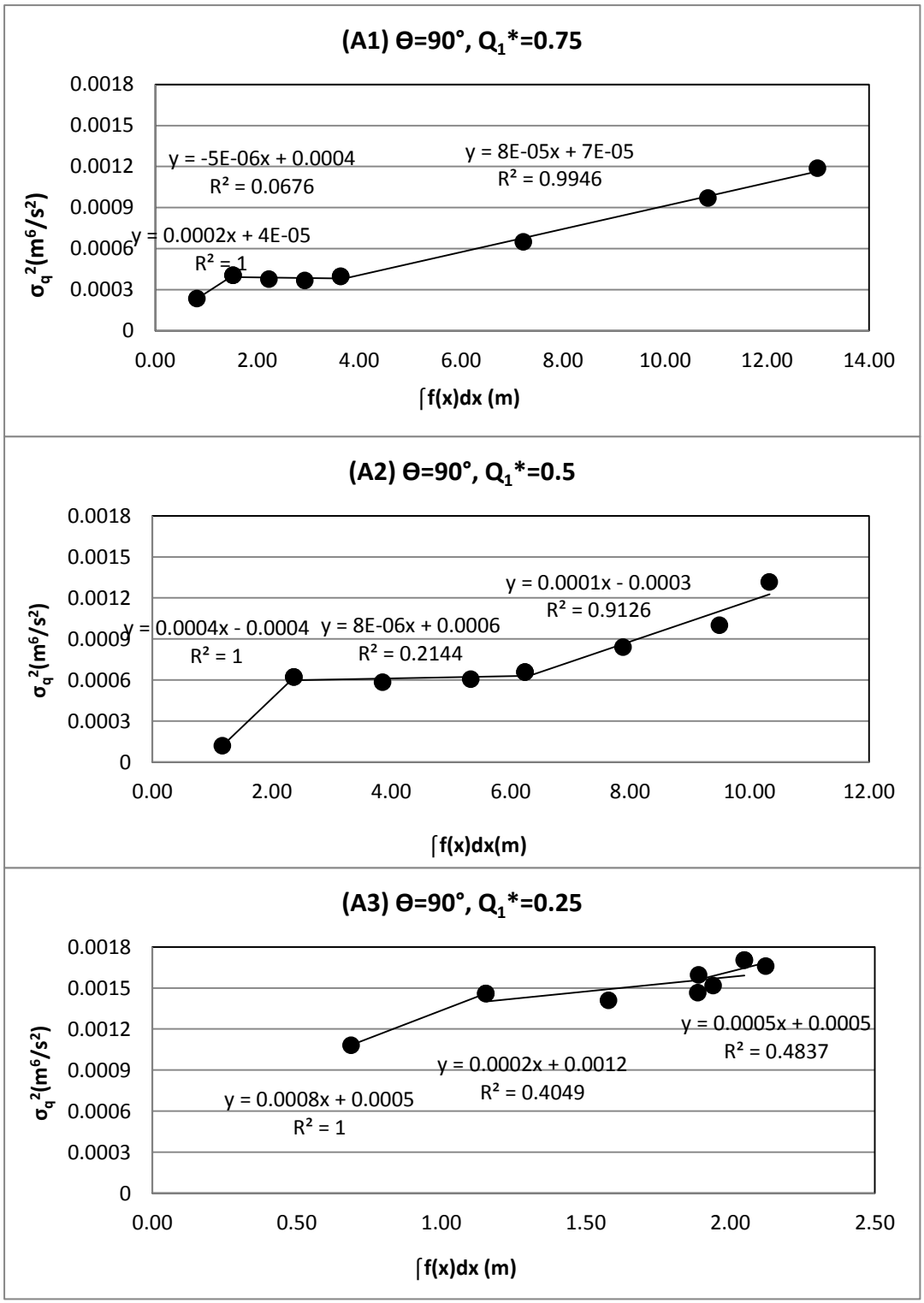

Figure 5-1: Change of variance of transverse concentration profiles along the channel by using generalized moment method for Case A1, A2 and A3

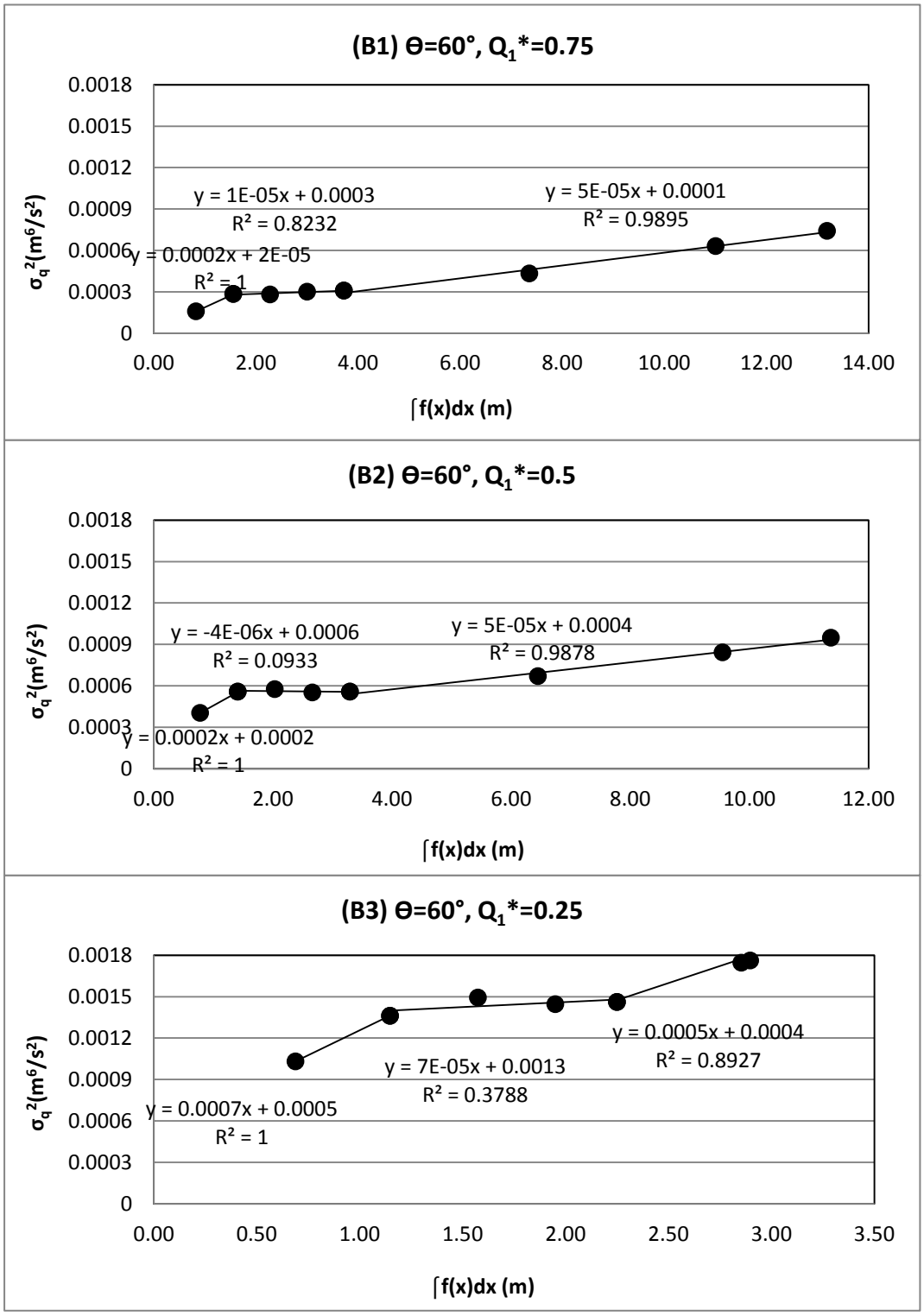

Figure 5-2: Change of variance of transverse concentration profiles along the channel by using generalized moment method for Case B1, B2 and B3

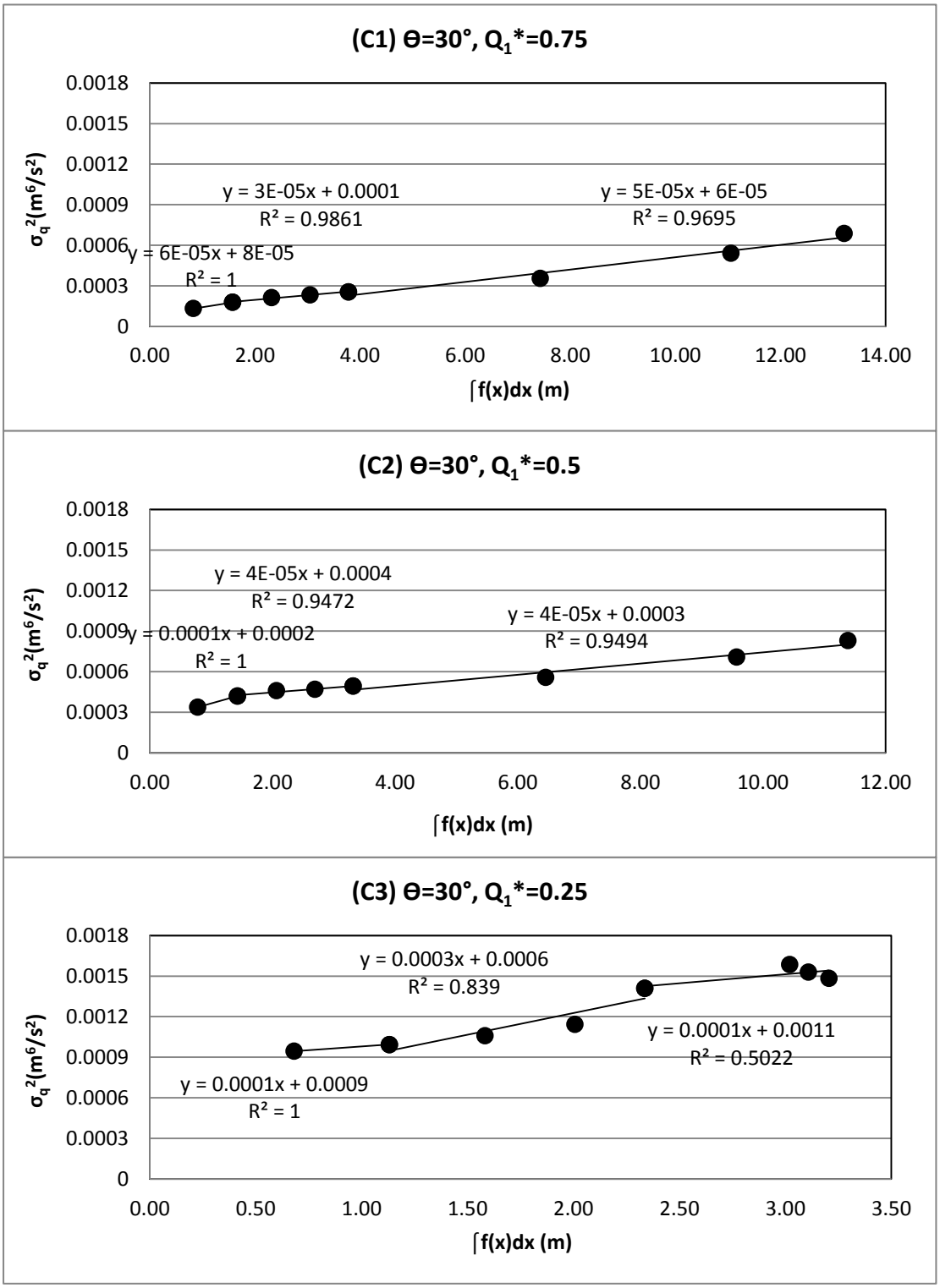

Figure 5-3: Change of variance of transverse concentration profiles along the channel by using generalized moment method for Case C1, C2 and C3

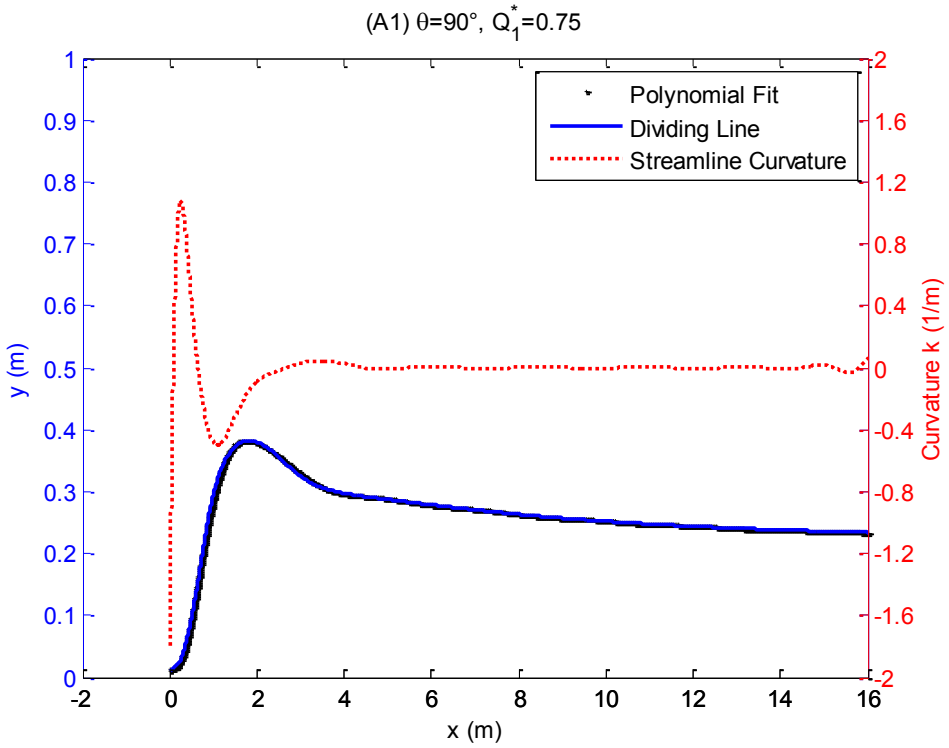
(A1) θ=90°, Q_1^*=0.75
Polynomial Fit
Dividing Line
Streamline Curvature
y (m)
x (m)
Curvature k (1/m)

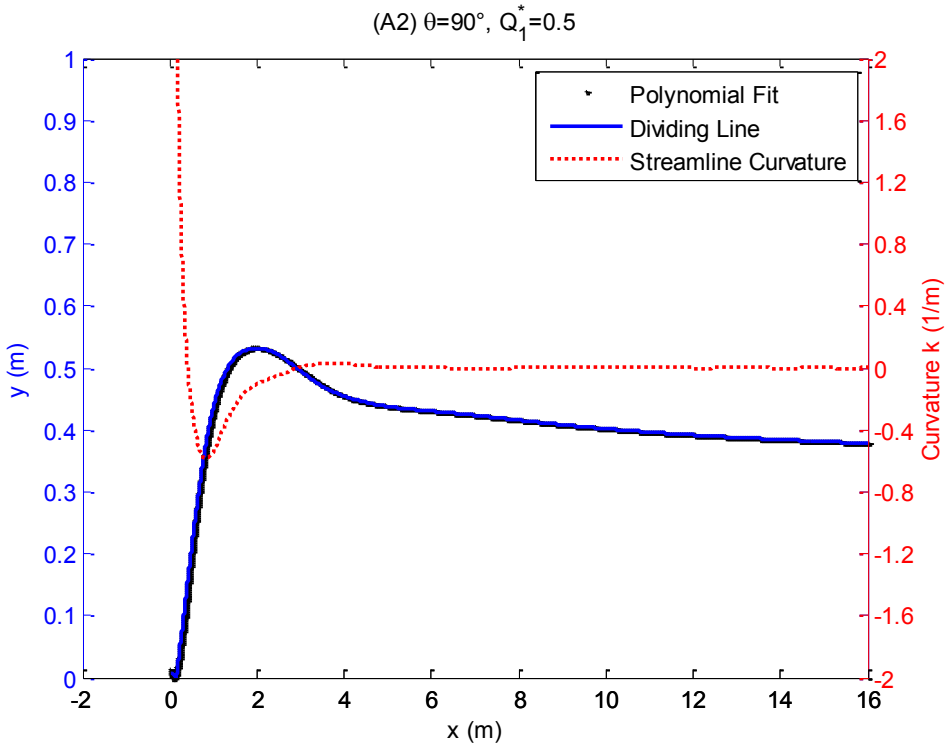
(A2) θ=90°, Q_1^*=0.5
Polynomial Fit
Dividing Line
Streamline Curvature
y (m)
x (m)
Curvature k (1/m)

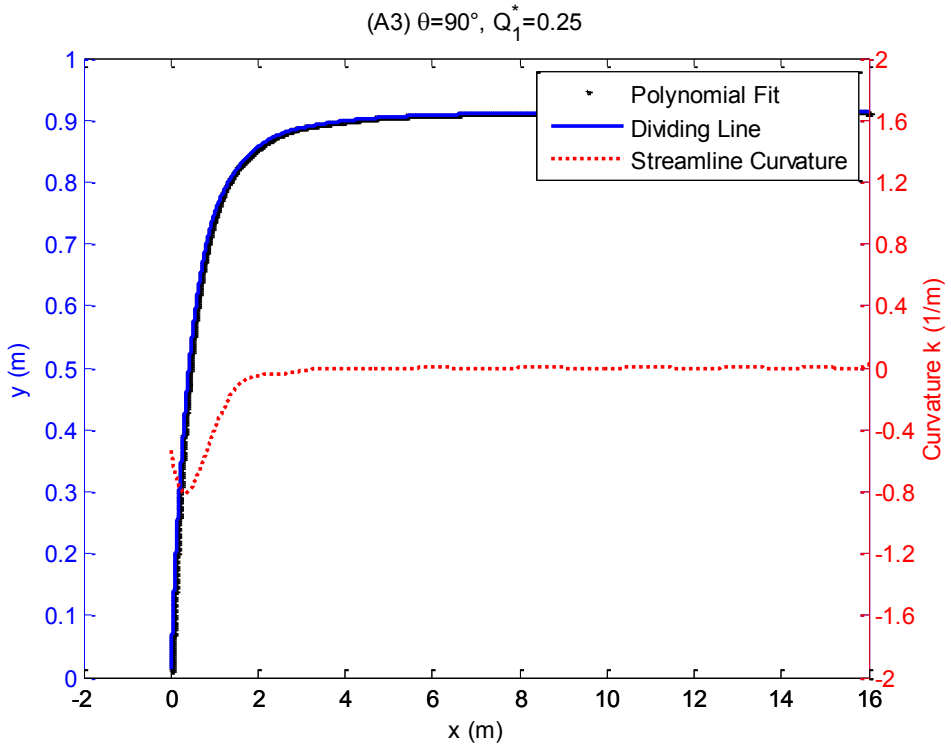
(A3) θ=90°, Q_1^*=0.25
Polynomial Fit
Dividing Line
Streamline Curvature
y (m)
x (m)
Curvature k (1/m)

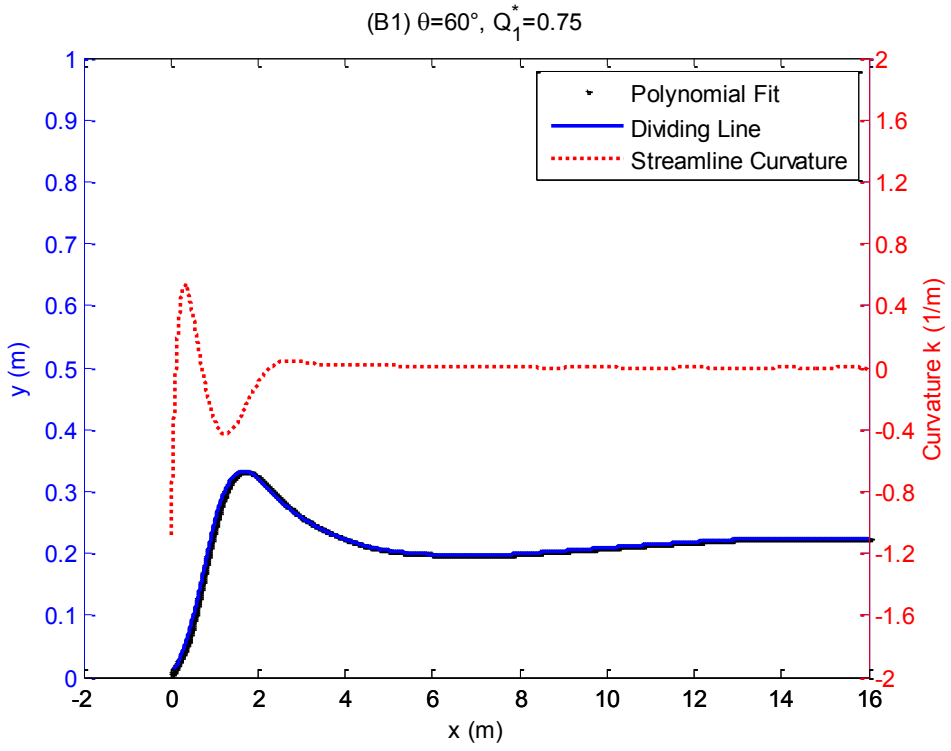
(B1) θ=60°, Q_1^*=0.75
Polynomial Fit
Dividing Line
Streamline Curvature
y (m)
x (m)
Curvature k (1/m)

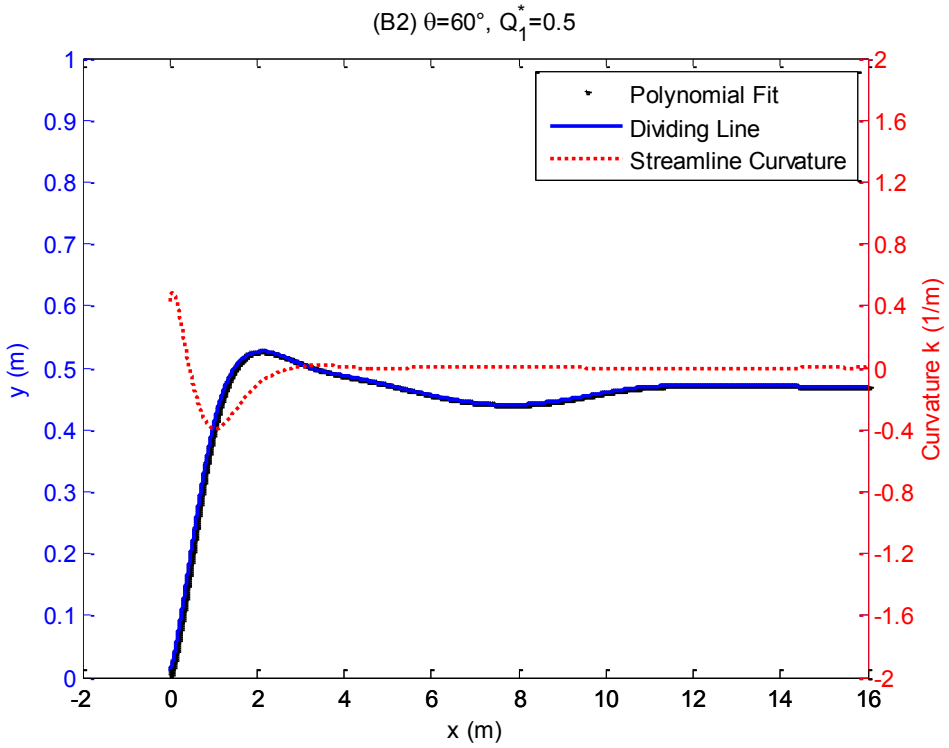
(B2) θ=60°, Q_1^*=0.5
Polynomial Fit
Dividing Line
Streamline Curvature
y (m)
Curvature k (1/m)
x (m)

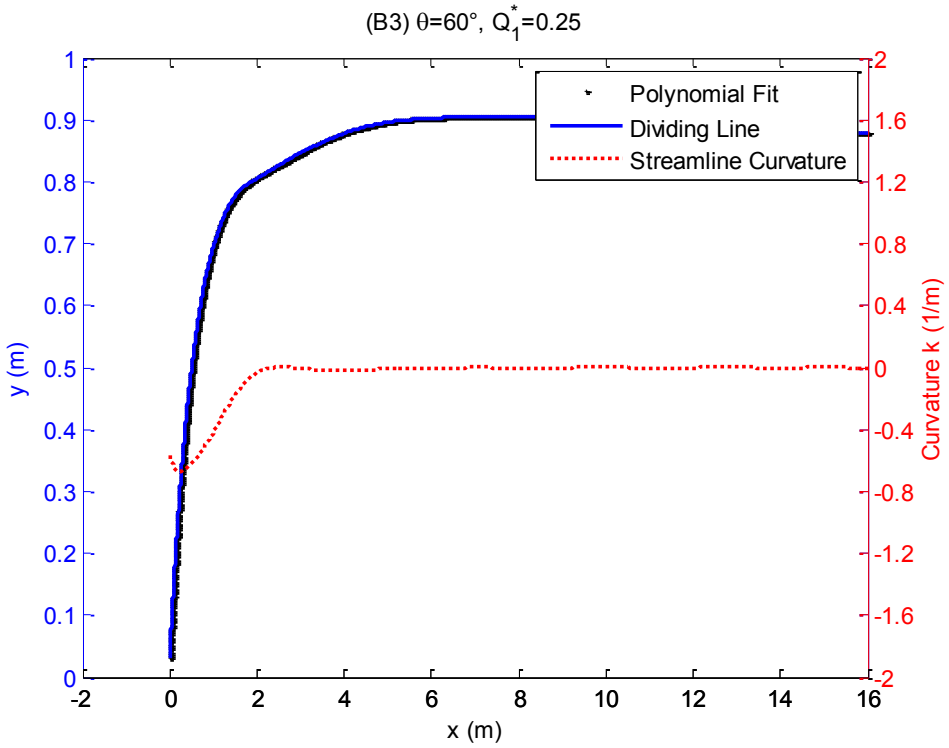
(B3) θ=60°, Q_1^*=0.25
Polynomial Fit
Dividing Line
Streamline Curvature
y (m)
Curvature k (1/m)
x (m)

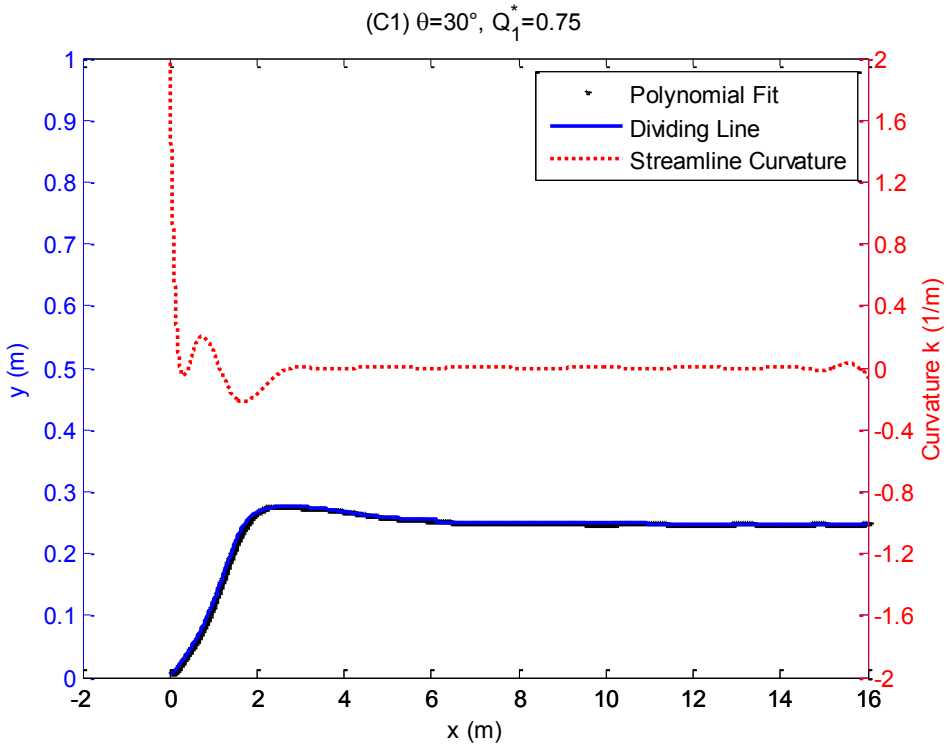
(C1) θ=30°, Q_1^*=0.75
Polynomial Fit
Dividing Line
Streamline Curvature
y (m)
x (m)
Curvature k (1/m)

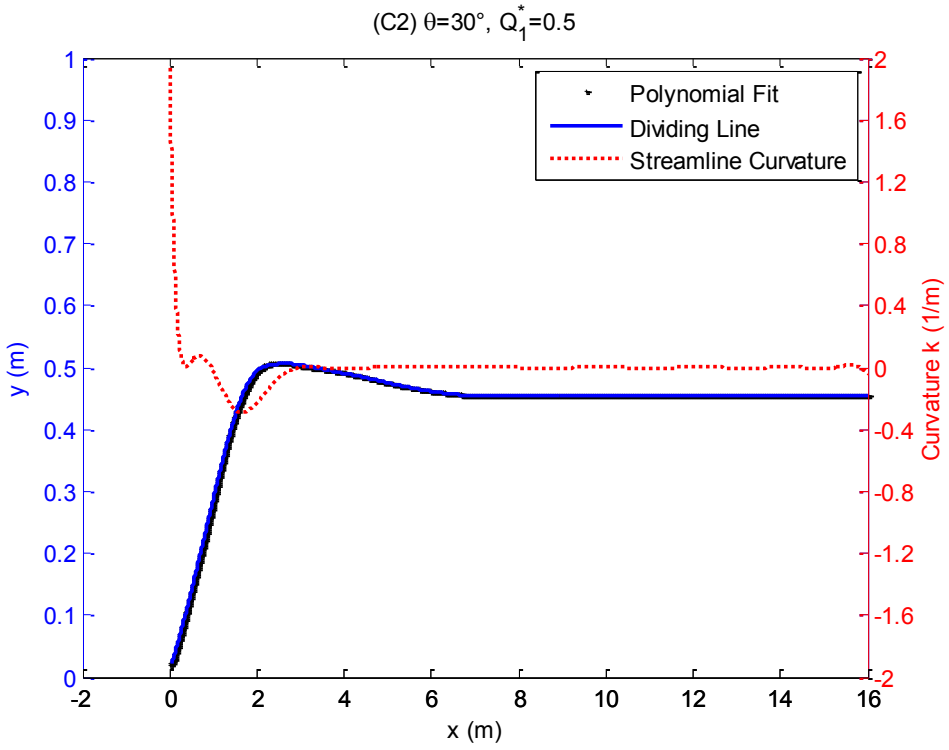
(C2) θ=30°, Q_1^*=0.5
Polynomial Fit
Dividing Line
Streamline Curvature
y (m)
x (m)
Curvature k (1/m)

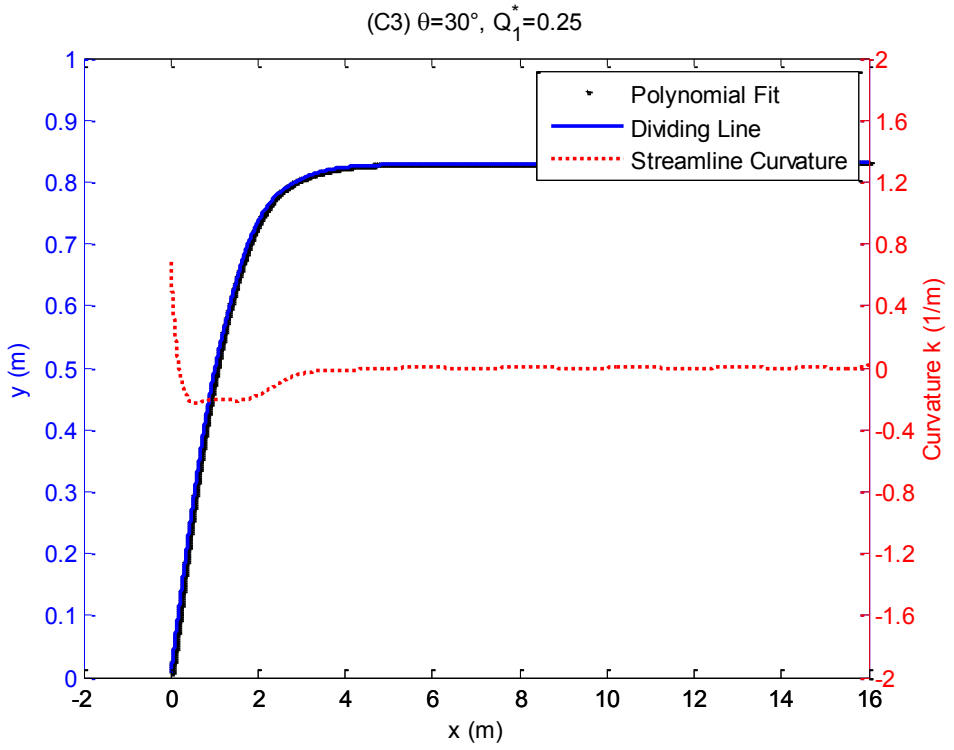

Figure 5-4: Plots of dividing line with its polynomial fit and calculated streamline curvature for nine cases

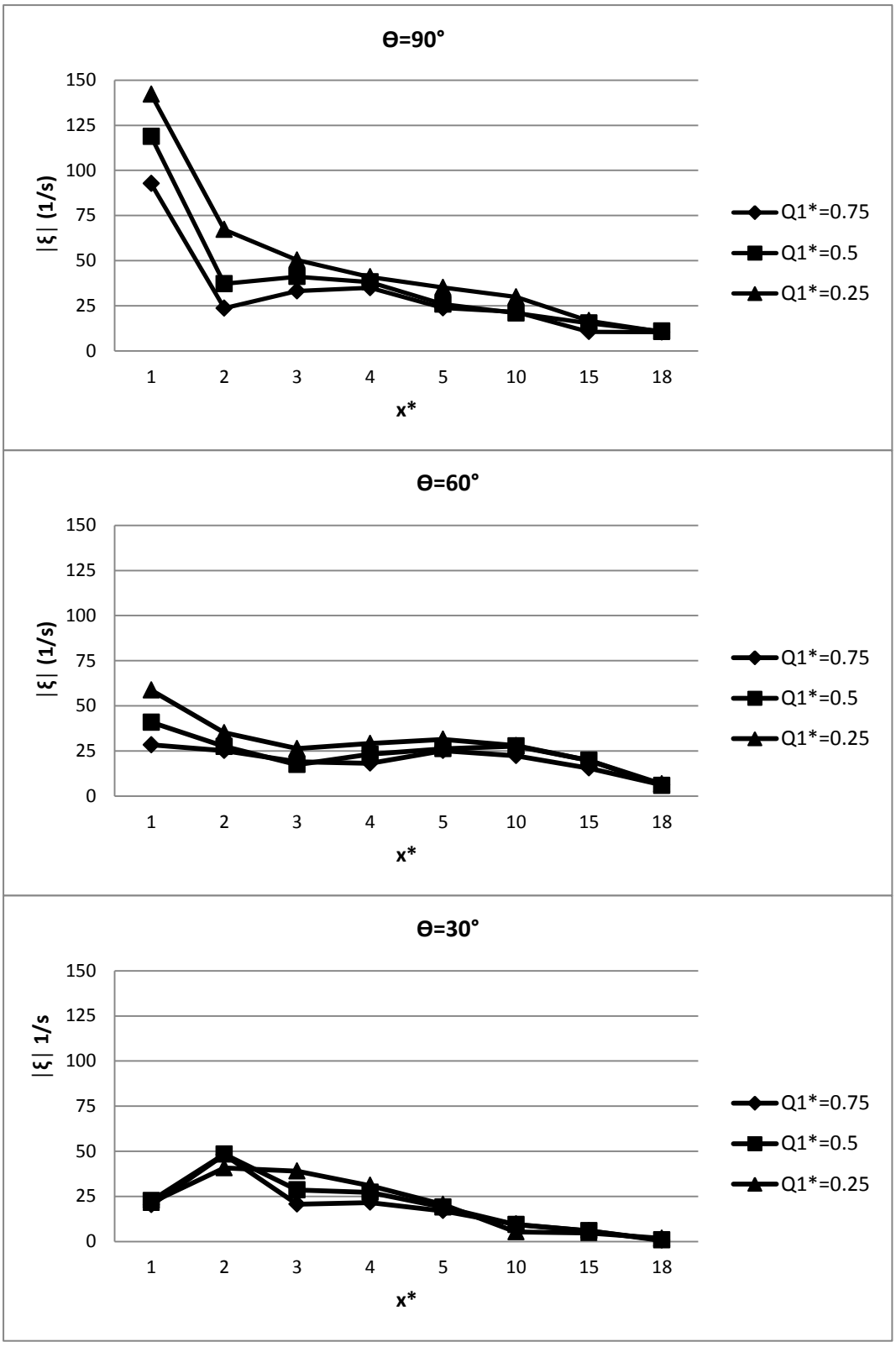

Figure 5-5: Plots of the maximum absolute value of streamwise component of velocity vorticity at eight cross sections for nine cases

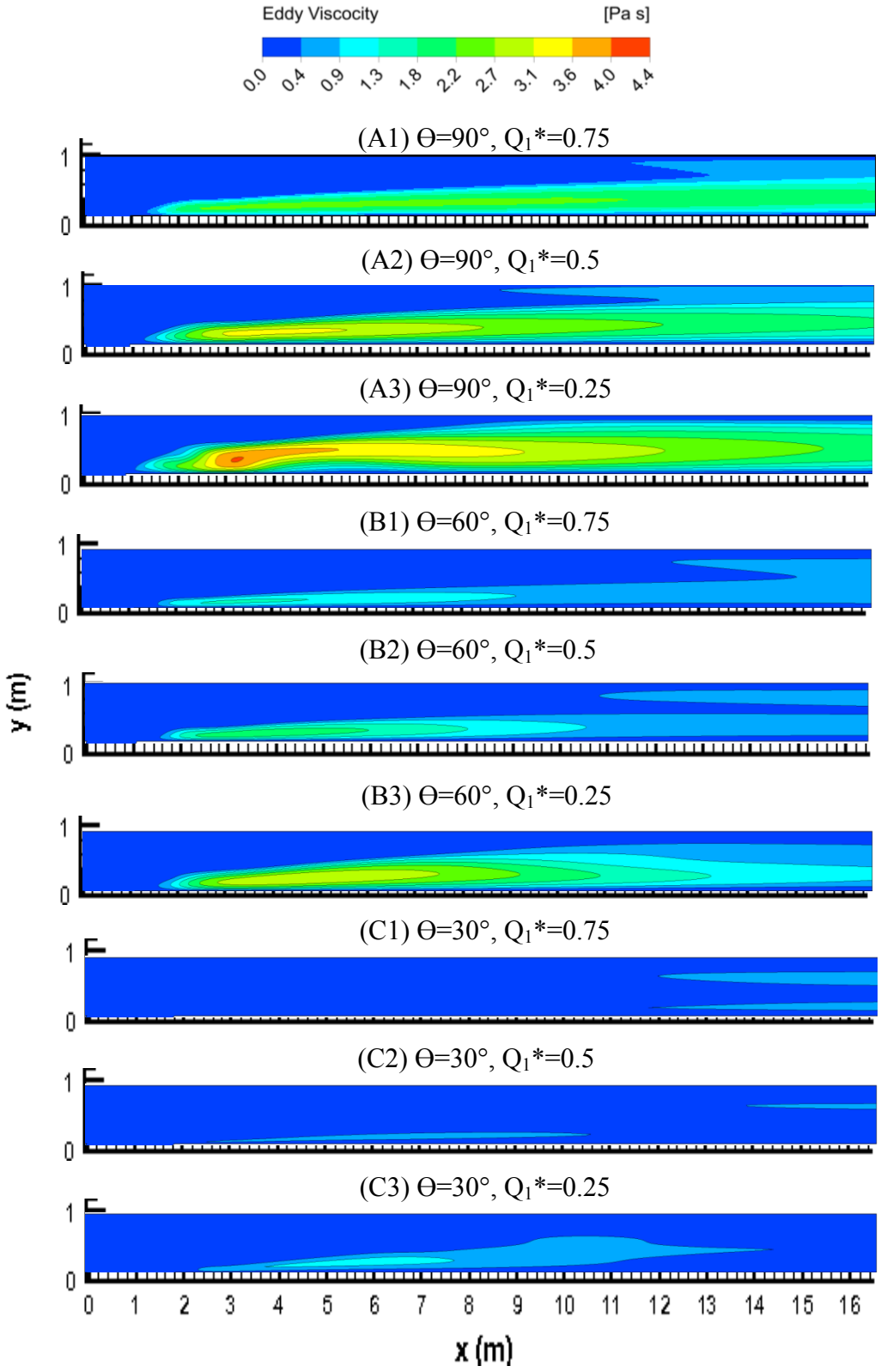

Figure 5-6: Contour map showing the water eddy viscosity for nine cases

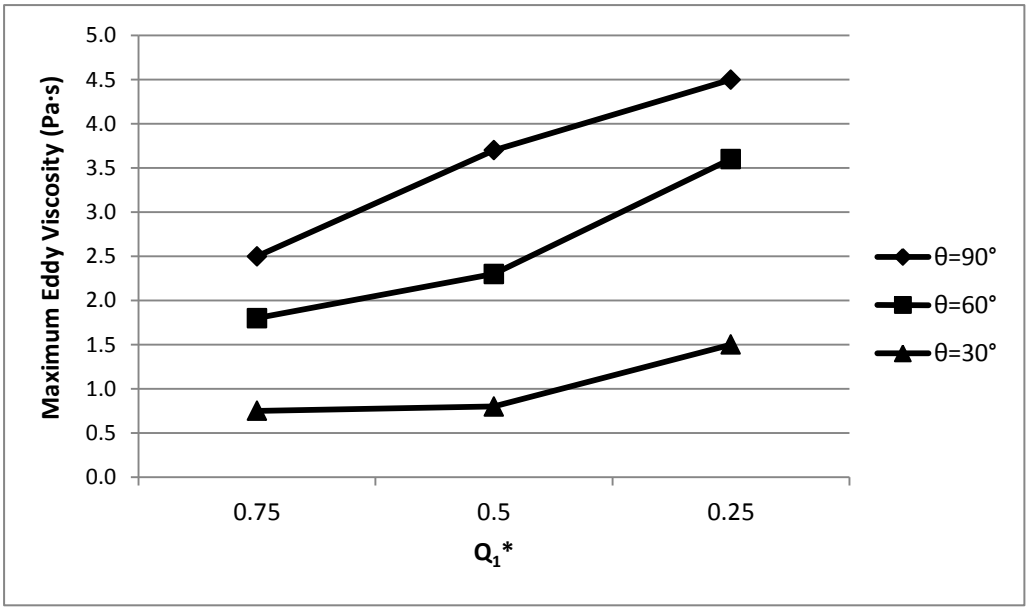

Figure 5-7: Comparison of maximum eddy viscosity for each case

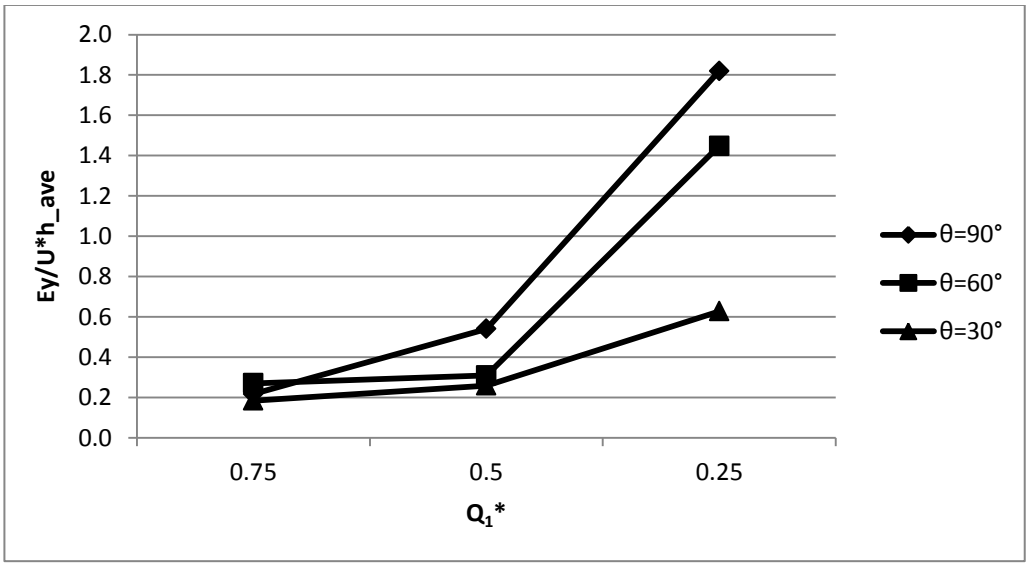

Figure 5-8: Comparison of averaged dimensionless transverse mixing coefficients for each case

References:

Albers, C., and Steffler, P. (2007). "Estimating transverse mixing in open channels due to secondary current-induced shear dispersion." *Journal of Hydraulic Engineering*, 133(2).

Ashmore, P. E., Ferguson, R. I., Prestegaard, K. L., Ashworth, P. J., and Paola, C. (1992). "Secondary flow in anabranch confluences of a braided, gravel-bed stream." *Earth Surface Processes and Landforms*, 17, 299-311.

Baek, K. O., and Seo, I. W. (2008). "Prediction of transverse dispersion coefficient using vertical profile of secondary flow in meandering channels." *KSCE Journal of Civil Engineering*, 12(6), 417-426.

Beltaos, S. (1979). "Transverse mixing in natural streams." *CAN. J. CIV. ENG.*, 6, 575-591.

Best, J. L. (1986). "The morphology of river channel confluences." *Progress in Physical Geography*, 10(2), 157-174.

Best, J. L. (1987). "Flow dynamics at river channel confluences implications for sediment transport and bed morphology." *The Society of Economic Paleontologists and Mineralogists*.

Best, J. L. (1988). "Sediment transport and bed morphology at river channel confluence." *Sedimentology*, 35, 481-498.

Best, J. L., and Ashworth, P. J. (1997). "Sour in large braided rivers." *Nature*, 387(15), 275-277.

Best, J. L., and Reid, I. (1984). "Separation zone at open channel junctions." *Journal of Hydraulic Engineering*, 110(11), 19270.

Best, J. L., and Roy, A. G. (1991). "Mixing-layer distortion at the confluence of channels of different depth." *Nature*, 350.

Biron, P. M., Best, J. L., and Roy, A. G. (1996a). "Effects of bed discordance on flow dynamics at open channel confluences." *Journal of Hydraulic Engineering*, 122(12), 8609.

Biron, P. M., Ramamurthy, A. S., and Han, S. (2004). "Three-dimensional numerical modeling of mixing at river confluence." *Journal of Hydraulic Engineering*, 130(3).

Boxall, J. B., and Guymer, I. (2003). "Analysis and prediction of transverse mixing coefficients in natural channels." *Journal of Hydraulic Engineering*, 129(2).

Bradbrook, K. F., Biron, P. M., Lane, S. N., Richards, K. S., and Roy, A. G. (1998). "Investigation of controls on secondary circulation in a simple confluence geometry using a three dimenstional numerical model." *Hodrological Processes*, 12, 1371-1396.

Bradbrook, K. F., Lane, S. N., and Richards, K. S. (2000). "Numerical simulation of three-dimensional time-averaged flow structure at river channel confluence." *Water Resources Research*, 36(9), 2731-2746.

Bradbrook, K. F., Lane, S. N., Richards, K. S., Biron, P. M., and Roy, A. G. (2001). "Role of bed discordance at asymmetrical river confluences." *Journal of Hydraulic Engineering*, 127(5), 19037.

CFX, A. (2009). "ANSYS CFX Sover Theory Guide." ANSYS Inc.

Constantinescu, G., Miyawaki, S., Rhoads, B., Sukhodolov, A., and Kirkil, G. (2011). "Structure of turbulent flow at a river confluence with momentum and velocity ratios close to 1: Insight provided by an eddy-resolving numerical simulation." *Water Resources Research*, 47(5).

Dow, K. E., Steffler, P. M., and Zhu, D. Z. (2009). "Case study: intermediate field mixing for a bank discharge in a natural river." *Journal of Hydraulic Engineering*, 135(1).

Elhadi, N., Harrington, A., Hill, I., Lau, Y. L., and Krishnapp, B. G. (1984). "River mixing-A state-of-the-art report." *Can. J. Civ. Eng.*, 11, 585-609.

Ferziger, J. H., and Peric, M. (2002). *Computational methods for fluid dynamics*, Springer, N.Y.

Fischer, H. B., List, E. J., Imberger, J., and Brooks, N. H. (1979). *Mixing in island and coastal waters*, San Diego.

Gaudet, J. M., and Roy, A. G. (1995). "Effect of bed morphology on flow mixing length at river confluences." *Nature*, 373.

Ghostine, R., Mose, R., Vazquez, J., Ghenaim, A., and Grégoire, C. (2010). "Two-dimensional simulation of subcritical flow at a combining junction: Luxury or Necessity?" *Journal of Hydraulic Engineering*, 136(10).

Greated, N. B. W. C. A. (1966). "An investigation of flow behaviour at the junction of rectangular channels."

Gurram, S. K., Karki, K. S., and Hager, W. H. (1997). "Subcritical junction flow." *Journal of Hydraulic Engineering*, 123(5), 11255.

Hirt, C. W., and Nichols, B. D. (1981). "Volume of fluid (VOF) method of the dynamics of free boundaries." *Journal of Computational Physics*, 39, 201-225.

Hsu, C.-C., Lee, W.-J., and Chan, C.-H. (1998b). "Subcritical open-channel junction flow." *Journal of Hydraulic Engineering*, 124(8), 11866.

Hsu, C.-C., Wu, F.-S., and Lee, W.-J. (1998a). "Flow at 90° equal-width open-channel junction." *Journal of Hydraulic Engineering*, 124(2), 9516.

Huang, J., Weber, L. J., and Lai, Y. G. (2002). "Three-dimensional numerical study of flows in open-channel junctions." *Journal of Hydraulic Engineering,*, 128(3).

Khan, A. A., Cadavid, R., and Wang, S. S. Y. (2000). "Simulation of channel confluence and bifurcation using the CCHE2D model." *Proc. Instn Civ. Engrs Water & Mar. Engng*, 142(97-102).

Lane, S. N., Bradbrook, K. F., Richards, K. S., Biron, P. A., and Roy, A. G. (1999). "The application of computational fluid dynamics to natural river channels three-dimensional versus two-dimensional approaches " *Geomorphology*, 29, 1-20.

Lane, S. N., Bradbrook, K. F., Richards, K. S., Biron, P. M., and Roy, A. G. (2000). "Secondary circulation cells in river channel confluences: measurement artefacts or coherent flow structures?" *Hydrological Processes*, 14, 2047-2071.

Lane, S. N., Parsons, D. R., Best, J. L., Orfeo, O., Kostaschuk, R. A., and Hardy, R. J. (2008). "Causes of rapid mixing at a junction of two large rivers: Río

Paraná and Río Paraguay, Argentina." *Journal of Geophysical Research*, 113(F2).

Laraque, A., Guyot, J. L., and Filizola, N. (2009). "Mixing processes in the Amazon River at the confluences of the Negro and Solimões Rivers, Encontro das Águas, Manaus, Brazil." *Hydrological Processes*, 23(22), 3131-3140.

Launder, B. E., and Spalding, D. B. (1974). "The numerical computation of turbulent flows." *Computre Methods in Applied Mechanics and Engineering*, 3, 269-289.

Ma, L., Ashorth, P. I., Best, J. L., Elliott, L., Ingham, D. B., and Whitcombe, L. J. (2002). "Computational fluid dynamics and the physical modelling of an upland urban river." *Geomorphology*, 44, 375-391.

Manninen, M., V., T., and S., K. (1996). "On the mixture model for multiphase flow." *Espoo*, Technical Research Center of Finland, Finland.

Maurice-Bourgoin, L., Quemerais, B., Moreira-Turcq, P., and Seyler, P. (2003). "Transport, distribution and speciation of mercury in the Amazon River at the confluence of black and white waters of the Negro and Solimões Rivers." *Hydrological Processes*, 17(7), 1405-1417.

Mosley, M. P. (1976). "An experimental study of channel confluences." *Journal of Geology*, 84(5), 535-562.

Orfeo, O., Parsons, D. R., Best, J. L., Lane, S. N., Hardy, R. J., Kostaschuk, R., Szupiany, R. N., and Amsler, M. L. (2006). "Morphology and flow structures in a large confluence-diffluence." *Taylor & Francis Group plc*London, UK.

Parsons, D. R., Best, J. L., Lane, S. N., Orfeo, O., Hardy, R. J., and Kostaschuk, R. (2007). "Form roughness and the absence of secondary flow in a large confluence–diffluence, Rio Paraná, Argentina." *Earth Surface Processes and Landforms*, 32(1), 155-162.

Ramamurthy, A. S., Carballada, L. B., and Tran, D. M. (1988). "Combining open channel flow at right angled junctions." *Journal of Hydraulic Engineering*, 114(12), 23003.

Ramón, C. L., Hoyer, A. B., Armengol, J., Dolz, J., and Rueda, F. J. (2013). "Mixing and circulation at the confluence of two rivers entering a meandering reservoir." *Water Resources Research*, 49(3), 1429-1445.

Rathbun, R. E., and Rostad, C. E. (2004). "Lateral mixing in the Mississippi River below the confluence with the Ohio River." *Water Resources Research*, 40(5), n/a-n/a.

Rhoads, B. L., and Kenworthy, S. T. (1995). "Flow structure at an asymmetrical stream confluence." *Geomorphology*, 11, 273-293.

Rhoads, B. L., and Kenworthy, S. T. (1998). "Time-averaged flow structure in the central region of a stream confluence." *Earth Surface Processes and Landforms*, 23, 171-191.

Rhoads, B. L., and Sukhodolov, A. N. (2001). "Field investigation of three-dimensional flow structure at stream confluences 1. Thermal mixing and time-averaged velocities." *Water Resources Research*, 37(9), 2393-2410.

Rhoads, B. L., and Sukhodolov, A. N. (2004). "Spatial and temporal structure of shear layer turbulence at a stream confluence." *Water Resources Research*, 40(6), n/a-n/a.

Rhoads, B. L., and Sukhodolov, A. N. (2008). "Lateral momentum flux and the spatial evolution of flow within a confluence mixing interface." *Water Resources Research*, 44(8), n/a-n/a.

Rice, S. P., Roy, A. G., and Rhoads, B. L. (2008). *River confluences, tributaries, and the fluvial network*, Wiley, England.

Romero-Gomez, P., C.K.Ho, and Choi, C. Y. (2008). "Mixing at Cross Junctions in Water Distribution Systems. I: Numerical Study." *Journal of Water Resources Planning and Management*, 134(3).

Rozovskiĭ, I. L., and Prushansky, J. (1961). *Flow of water in bends of open channels / I.L. Rozovskii, translated by: Y. Prushansky*, Jerusalem : published for the National Science Foundation, Washington, D.C. and the Dept. of the Interior , U.S.A. by the Israel Program for Scientific Translations, 1961.

Rutherford, J. C. (1994). *River mixing*, Wiley, England.

Serres, B. D., Roy, A. G., Biron, P. M., and Best, J. L. (1999). "Three dimensional structure of flow at a confluence of river channels with discordant beds." *Geomorphology*, 26, 313-335.

Shakibainia, A., Tabatabai, M. R. M., and Zarrati, A. R. (2010). "Three-dimensional numerical study of flow structure in channel confluences." *Can. J. Civ. Eng.*, 37, 772-781.

Shen, Y. (2009). "Evaluating ecological influences of altered flow regimes using two-and three-dimensional hydrodynamic models." Doctor of Philosophy, Virginia Polytechnic Institute and State University, Blacksburg, Virginia.

Szupiany, R. N., Amsler, M. L., Parsons, D. R., and Best, J. L. (2009). "Morphology, flow structure, and suspended bed sediment transport at two large braid-bar confluences." *Water Resources Research*, 45(5), n/a-n/a.

Talor, E. H. (1944). "Flow characteristics at rectangular open-channel junctions." *Trans. ASCE*, 109, 893-902.

Wang, X., and Cheng, L. (2000). "Three dimensional simulation of a side discharge into a cross channel flow." *Computers & Fluids*, 29, 415-433.

Weber, L. J., Schumate, E. D., and Mawer, N. (2001). "Experiments on flow at a 90° open-channel junction." *Journal of Hydraulic Engineering*, 127(5).

Weerakoon, S. B., Kawahara, Y., and Tamai, N. (1991). "Three-dimensional flow structure in channel confluences of rectangular section." *Proc. 24th IAHR Congr.*, 373-380.

Weerakoon, S. B., Tamai, N., and Kawahara, Y. (2003). "Depth average flow computation at a river confluence." *Water & Maritime Engineering*, 156(1), 73-83.

Wörner, M. (2003). "A compact introduction to the numerical modeling of multiphase flows." Forschungszentrum Karlsruhe GmbH, Karlsruhe, Germany.

Yahata, E., Kimura, I., Iwasaki, T., and Shimizu, Y. "Comparisons of various CFD models for computing river flows focusing on secondary currents." *Proc., River Flow*.

Yakhot, V., and Orszag, S. A. (1986). "Renormalization group analysis of turbulence. I. Basic theory." *Journal of Scientific Computing*, 1(1).

Yang, Q.-Y., Wang, X.-Y., Lu, W.-Z., and Wang, X.-K. (2009). "Experimental study on characteristics of separation zone in confluence zones in rivers." *Journal of Hydrologic Engineering*, 14(2).

Yotsukura, N., and Sayre, W. W. (1976). "Tansverse mixing in natural channels." *Water Resources Research*, 12(4).

Zhang, W., and Zhu, D. Z. (2011). "Transverse mixing in an unregulated northern river." *Journal of Hydraulic Engineering*, 137(11), 1426-1440.

Appendix: River confluence of Peace River and Smoky River

The Peace River is a regulated river, with a monthly mean flow ranging from 1,370 m^3/s in March to 2,990 m^3/s in June and an annual mean discharge of 1,860 m^3/s at the Town of Peace River. The Smoky River is the largest tributary stream entering the Peace River approximately 4 km upstream of the Town of Peace River with an overall annual mean discharge of 345 m^3/s. The Town of Peace River is approximately 486 km northwest of the City of Edmonton and 195 km northeast of the City of Grande Prairie.

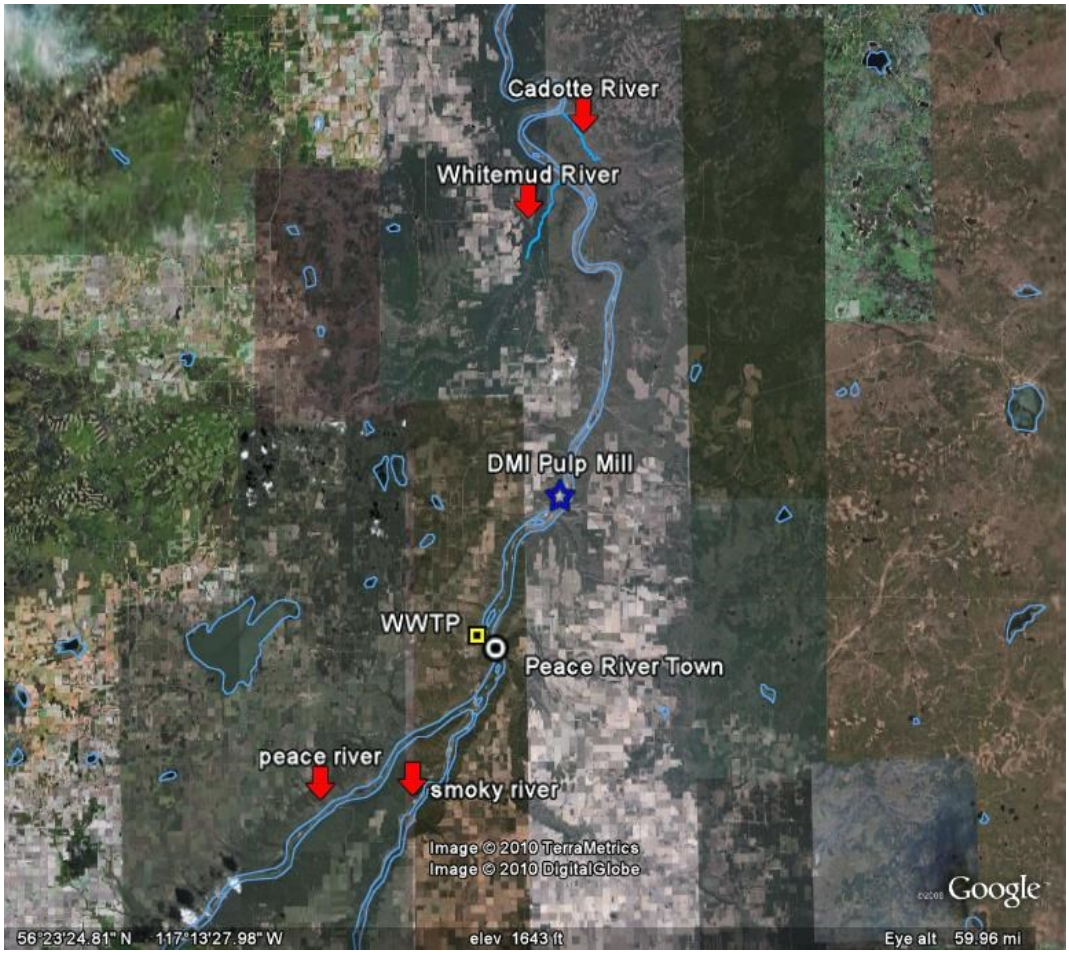

Figure 1 Peace River and Smoky River confluence (source: Google earth map)

The Smoky River receives effluent from the Weyerhaeuser Canada pulp mill through one of its major tributaries (the Wapiti River). The Smoky River drainage basin has extensive activities related to forestry, agriculture, coal, oil and gas. Other major tributaries to the Peace River downstream of the Town of the Peace River include the Whitemud River (54 km downstream), and Cadotte River (66 km downstream). The Cadotte River is not a major tributary to the Peace, but it drains an area that is underlain by a relatively large oil sands deposit. The extraction process typically involves injecting pressurized steam into the deposit to melt the tar and thus places demand on local surface water supplies. Figure 1 shows the relative locations of these Rivers.

This section of the River is unique as a result of the slow mixing of the Smoky River and the Peace River. Noton (1988) noted that "At the site 30 km downstream of the Smoky River, the "Smoky" plume was contained primarily within the right half of the mainstem channel." Also in this reach, the Peace River receives effluents from the Town of Peace River's wastewater treatment plant (WWTP), as well as the effluent from the Daishowa-Marubeni International Ltd. (DMI) pulp mill, which is located on the west bank of the Peace River about 15 km downstream of the Town of Peace River. In addition to the Town of Peace River's municipal water intake, Shell also has a water intake to draw water from the Peace River for its stream-assisted bitumen recovery (SAGD) oilsands operations. Other potential industrial activities within this river reach include a proposed nuclear power plant.

DMI pulp mill

The Peace River Pulp Division (PRPD) of Daishowa-Marubeni International Ltd. (DMI) mill is located on the west bank of the Peace River, approximately 15 km downstream of the town of Peace River. A topographical map of the region and property boundary map of the PRPD mill site are shown in Figures 2 (a) and (b), respectively. The mill was constructed in 1989 and commenced operation in July of 1990. The mill operates approximately 355 days a year. The other 10 days are used for a maintenance shutdown, which is usually scheduled in the first half of June. The Peace River pulp mill produces approximately 430,000 air-dried metric tones (ADMT) of bleached kraft pulp (BKP) annually. One-quarter of this total is softwood and three-quarters hardwood. A single line pulping system produces 1,350 ADMT per day of hardwood BKP, or 1,060 ADMT per day of softwood BKP (www.DMI.com).

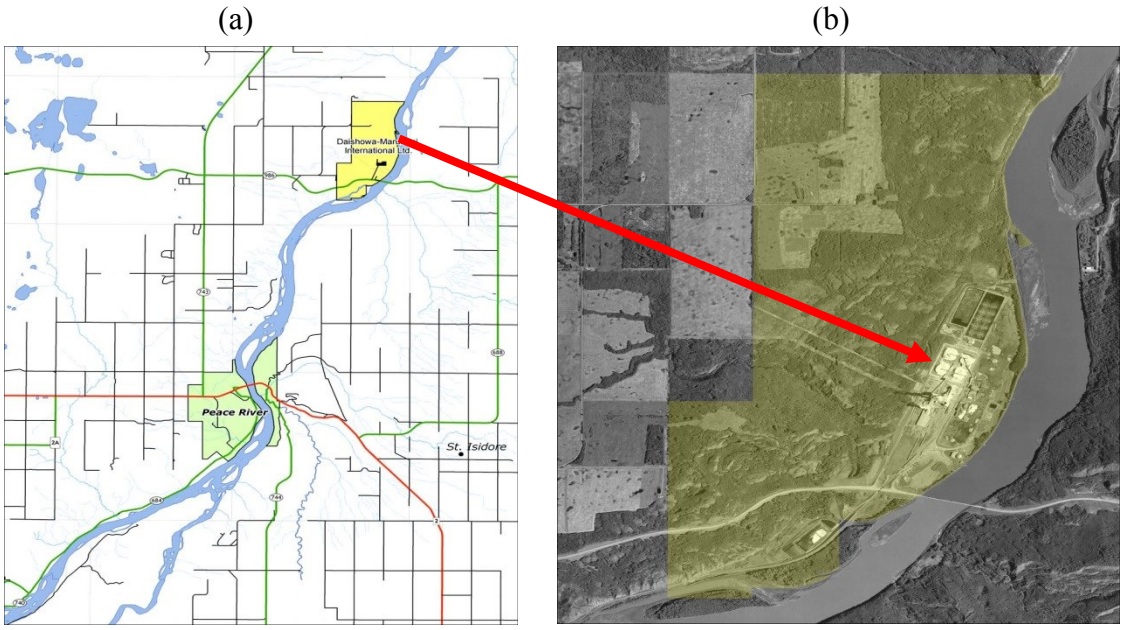

Figure 2: (a) General Location of the Peace River Pulp Mill (b) Peace River Pulp Division Property Area Highlighted (source: www.DMI.com)

From the Environmental Effects Monitoring (EEM) studies for DMI in cycle 4, the DMI production rate has ranged from 357,794 to 480,999 ADdt between 1994 and 2005, with a slight increasing trend over the last twelve years. The mean daily flow rate for the DMI treated effluent between 2002 and 2005 ranged from 47,993 to 69,185 m^3/day (see Fig. 3). The low value of mean daily flow rate happened in June 2004 is due to the shutdown months. The maximum daily flow rate never exceeds the value of 80,000 m^3/day.

The effluent quality information for DMI from the EEM study report is provided in Table1. The EEM report compared historical data with the data in 2002-2005 showing that the PH values and conductivity values have been similar over the years. The BOD_5 discharges and the TSS discharge from DMI mill have shown a decreasing trend over the past 12 years.

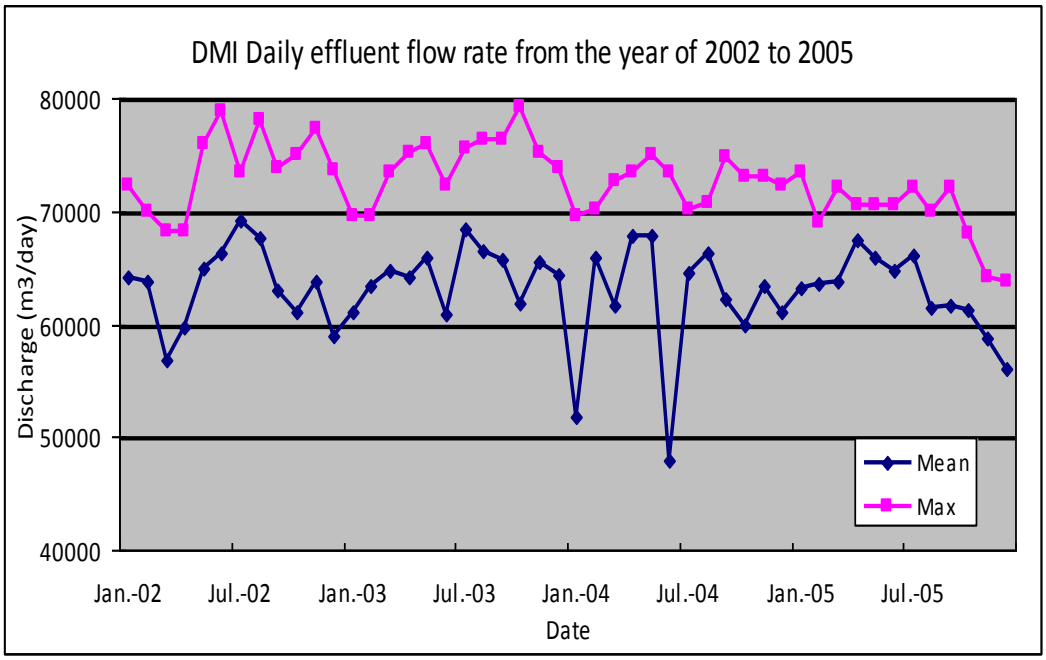

Figure 3: DMI Daily effluent flow rate from the year of 2002 to 2005

Table 1: Effluent Quality information

Parameters	2002-2005		
	Min.	Max.	Unit
PH	6.6	8.2	
Conductivity	2.5	2.97	µs/m
BOD5	373	706	kg/day
TSS	2170	2670	kg/day

The DMI diffuser occupies the centre of the river and consists of 14 outlet ports (only 7 are used). The diffuser is designed to achieve 1:100 dilutions within 20 to 30 m downstream of the diffuser under all flow conditions. Plume delineation study conducted in October 1993 showed that the isopleths delineating 1% concentration occurred within 50 m downstream of the diffuser (Stantec 2004). In their recent Environmental Effects Monitoring (EEM), DMI reported some mild nutrient enrichment evident in a localized area in the upper part of the reference area. Given the effectiveness of its diffuser in effluent mixing, it is DMI's belief that these local nutrient enrichments were likely due to the Town of Peace River sewage treatment effluent, and possibly some other unknown sources. Thus an improved study on the DMI effluent plume will help in understanding the effect of its effluent on the river water quality.

Peace River WWTP

The Waste Water Treatment Plant (WWTP) of the town of Peace River release the final effluent discharge rate generally below 0.2 m^3/s, while the average river flow at the Town of Peace River is about 2,700 m^3/s. While the river has a very high dilution potential, if effluent dispersion does not occur rapidly, the plume

below the discharge point may maintain toxic levels of Ammonia or exceed the surface water quality guidelines. According to Alina Wolanski (AENV, private communication), monitoring data collected from the Town of the Peace River's WWTP showed that between February and April 2008 levels of Ammonia Nitrogen in the final effluent increased significantly and ranged between 9.2 and 21.8 mg/L. Discharges of effluent with high Ammonia levels are highly undesirable and can be detrimental to the aquatic biota. The above Ammonia levels are at levels toxic to aquatic biota. While the river has a very high dilution potential, it is still important to delineate the effluent plume to identify the region where Ammonia level exceeds the surface water quality guidelines.

The locations of the contaminant sources are shown in *Fig. 4*.

Grande Prairie mill

The Grande Prairie mill, which was built in 1972, is located approximately 16 km south of Grande Prairie, Alberta, Canada, which, in turn, is located some 450 road km northwest of Edmonton. According to the study by S. M. Swanson et. in 1998, the Grande Prairie Kraft pulp mill produced about 300,000 air dry metric tons annually of fully bleached softwood pulp with spruce and pine as the fibre supply. The water used in the pulping process is taken from the Wapiti River, and treated effluent is returned to the Wapiti River. Since commencement of mill operations, wastewater from the mill had been treated in a primary clarifier and aerated lagoons prior to being discharged into the Wapiti River. The effluent discharge rate is about 59,000 m^3/day.

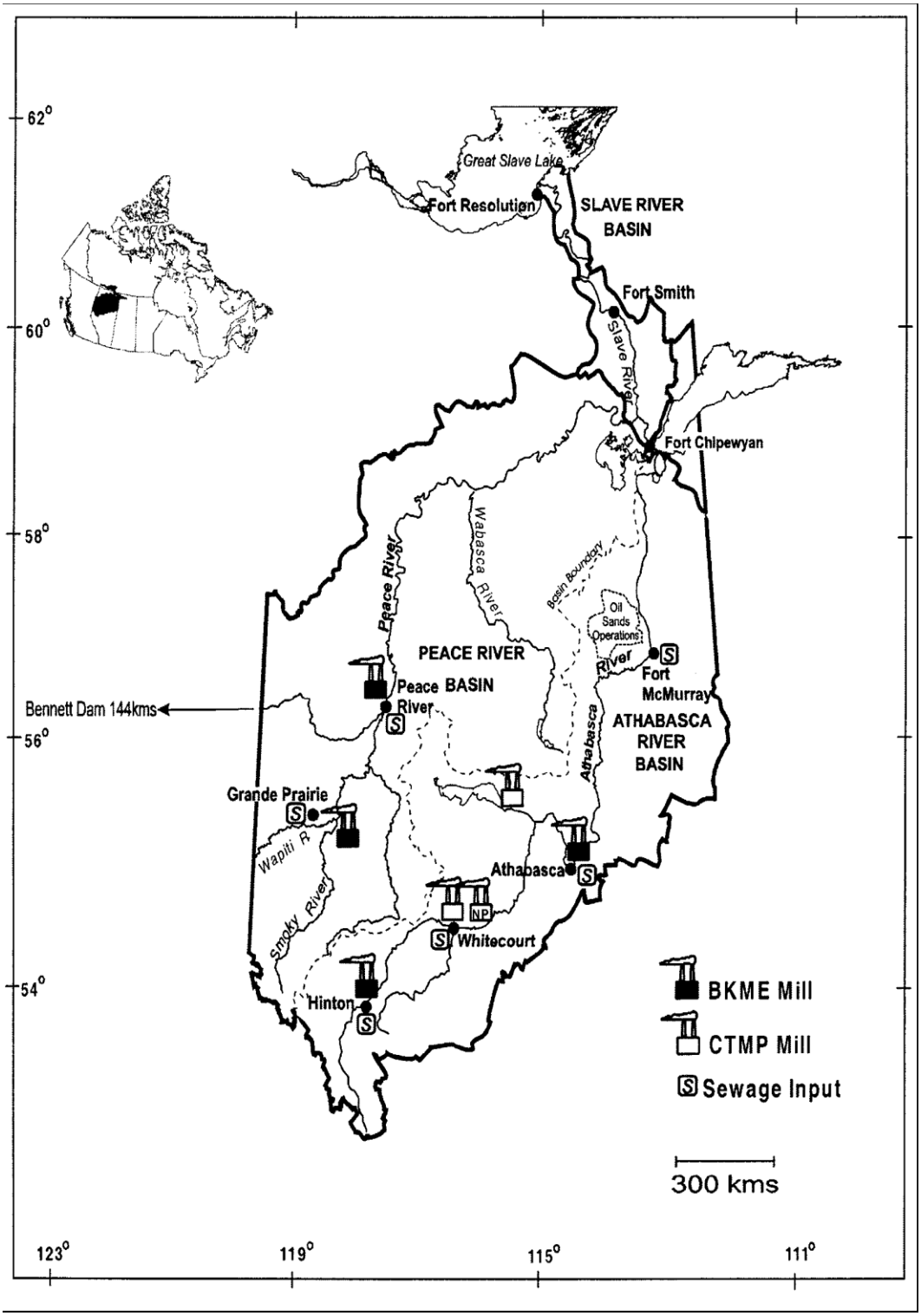

Figure 4: Northern River Basins Study Area in Western Canada indicating major environmental stressors on the Athabasca, Peace and Slave Rivers. (Frederick J. Wrona et. al 2000)

Sewage Treatment Plant for the Grande Prairie City

The sewage treatment plant (STP) for the city of Grande Prairie is the second main point source of effluent on the Wapiti River which will join into Smoky River and finally flow into Peace River. The STP effluent is released an average of just over three weeks/month at a regulated rate of 20,000 m^3/d.

Within a relatively short distance the Peace River receives effluent from (1) a correction facility upstream of the Town of Peace River, (2) the Town of Peace River and (3) the DMI Pulp Mill located 15 km below the Town. There is also input of contaminants from the Non-point sources such as agriculture, forestry, oil and gas, and urbanization.

River Water Level and Flow Discharge

Water discharge and level data of the Peace River and Smoky River within research interests are obtained from the Water Survey of Canada website (www.wsc.ec.gc.ca/). Figure 5 shows the hydrometric and water quality stations on the Peace River basin in Alberta. Since only three stations in the study reach, the Peace River above the Smoky River confluence, Smoky River at Watino, and the Peace River at Peace River Town are chosen to study the flow discharge near the river confluence.

- Peace River above the Smoky River confluence **07FD901**(56°09'18", 117 °26'33")
- Peace River at the Town of Peace River **07HA001** (56°13'28", 117 °17'20")
- Smoky River at Watino **07JG001** (55°42'57", 117 °37'30")

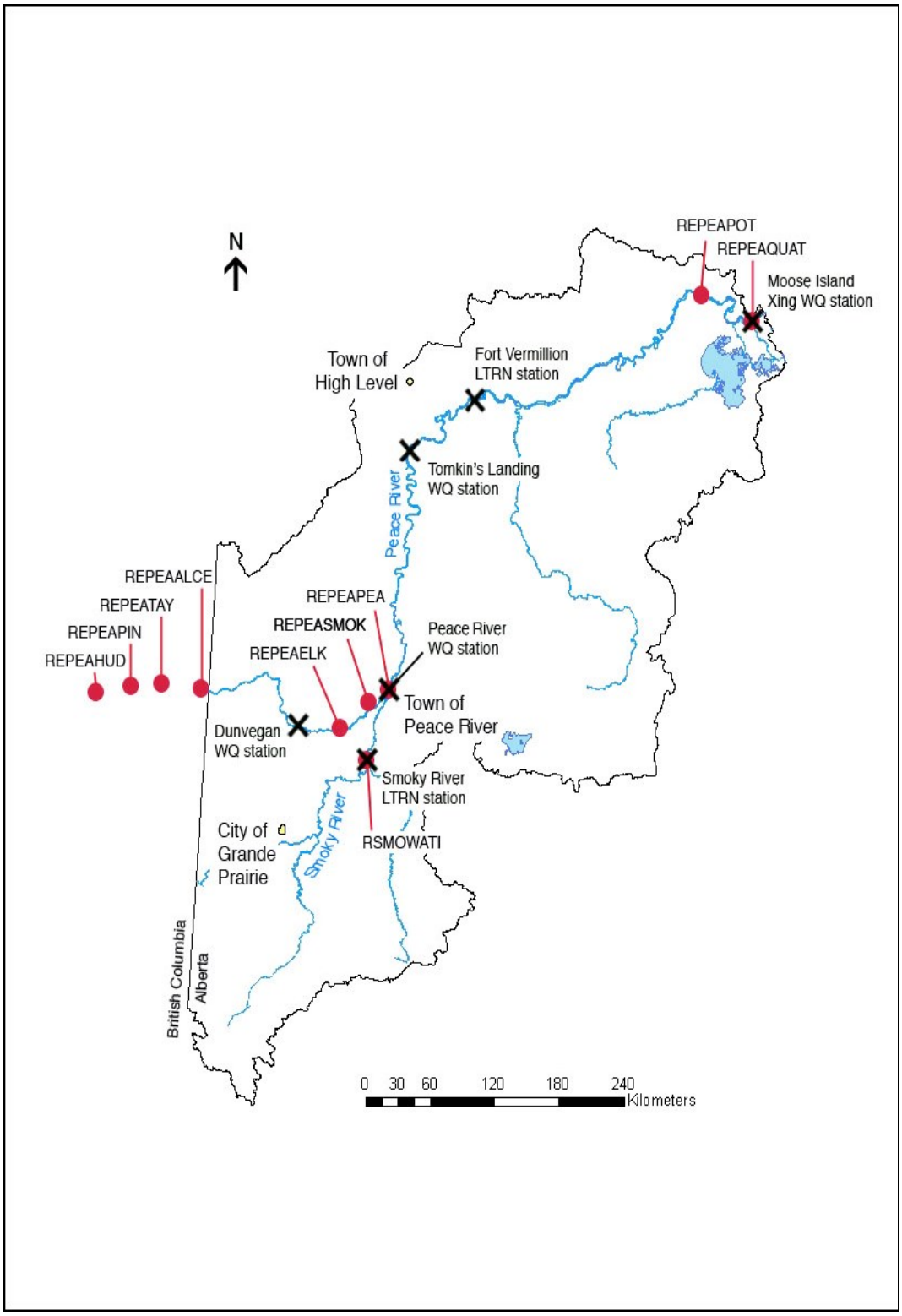

Figure 5: Peace River basin in Alberta showing hydrometric (●) and water quality (X) stations on the Peace River.

Smoky River at Watino (07JG001)

Discharge rate at Smoky River at Watino is monitored; the station located about 15km above the confluence with Peace River. The discharge rate is presented below, water level can vary 0.1~0.3m per day in winter, under ice cover conditions and the variation in summer is bigger up to 1m per day or more.

(a)

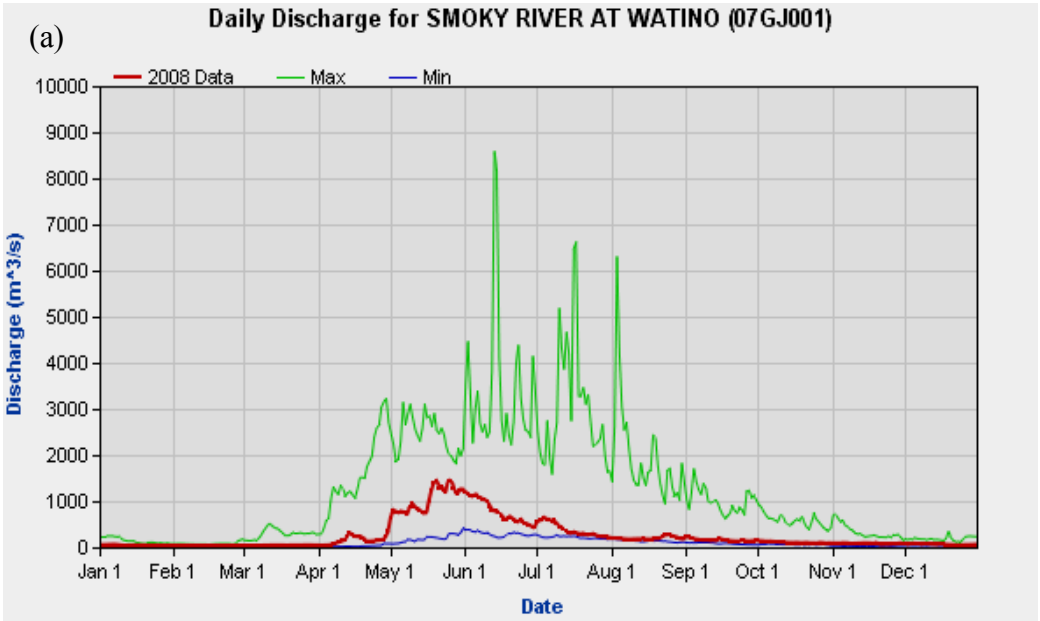

(b)

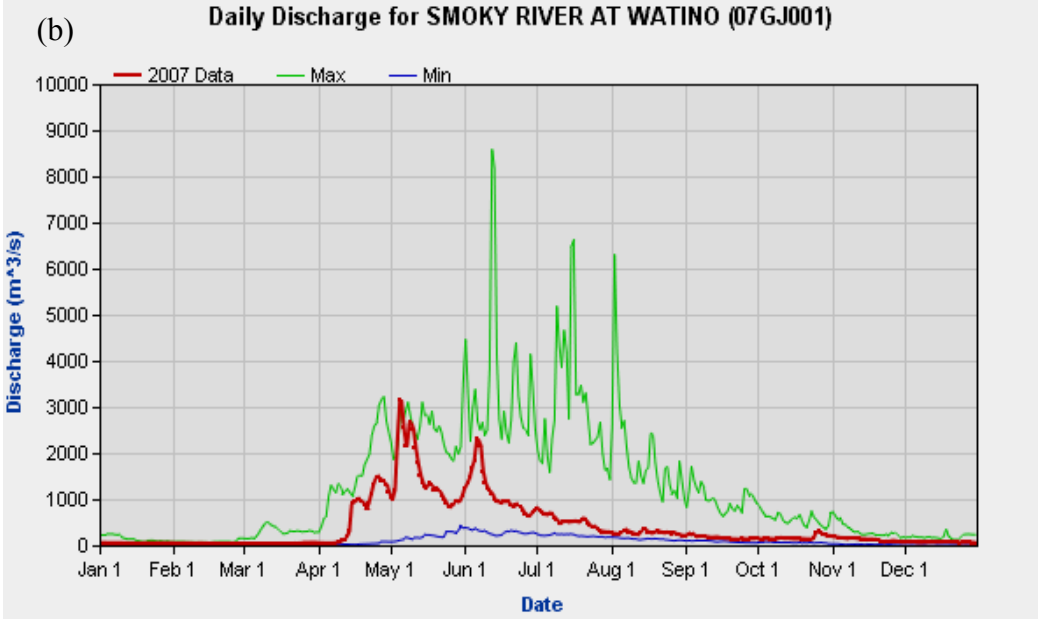

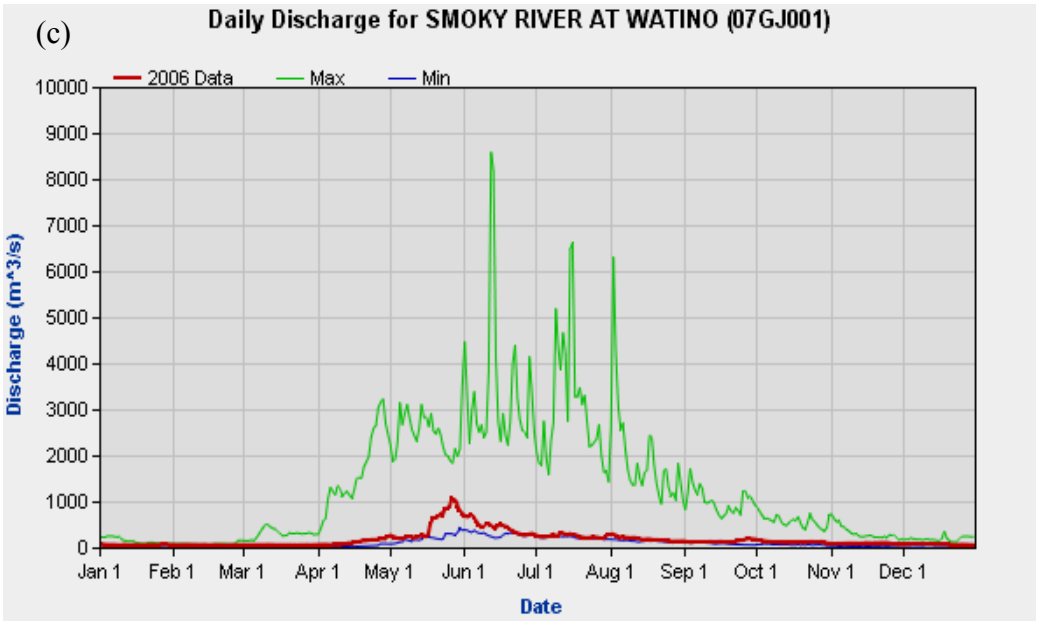

Figure 6 Daily Discharge for Smoky River at Watino from the year of 2006 to 2008

As can be seen in Fig. 6 (a), the peak value of discharge in 2008 is around 1400 m^3/s in late May, and the winter low value is around 40 m^3/s during December and next February. The maximum discharge value within a year happened in May during the year of 2006 to 2008. The largest maximum discharge is about 3000 m^3/s which occur in early May 2007, while in 2006 the discharge of river flow seemed lower than 1000 m^3/s. The lowest flow rate occurred during December and next February due to ice cover. And the peak flow is result in spring runoff due to ice breakup.

The overall annually mean discharges are 257 m^3/s, 394 m^3/s and 170 m^3/s in the year of 2008, 2007, 2006, respectively.

Peace River above Smoky River Confluence (07FD901)

Alberta Environment provides water level data at this station at every 15 minutes. On a typically day, water level doesn't vary a lot, the difference in water level usually falls into a range of 0.3~0.8 meters diurnally, the discharge rate can be obtained using the discharge rating curve along this reach. At monthly level , the variation of water level and discharge rate is bigger, as shown in figure , the water level variation falls into a range of 1~5 m monthly.

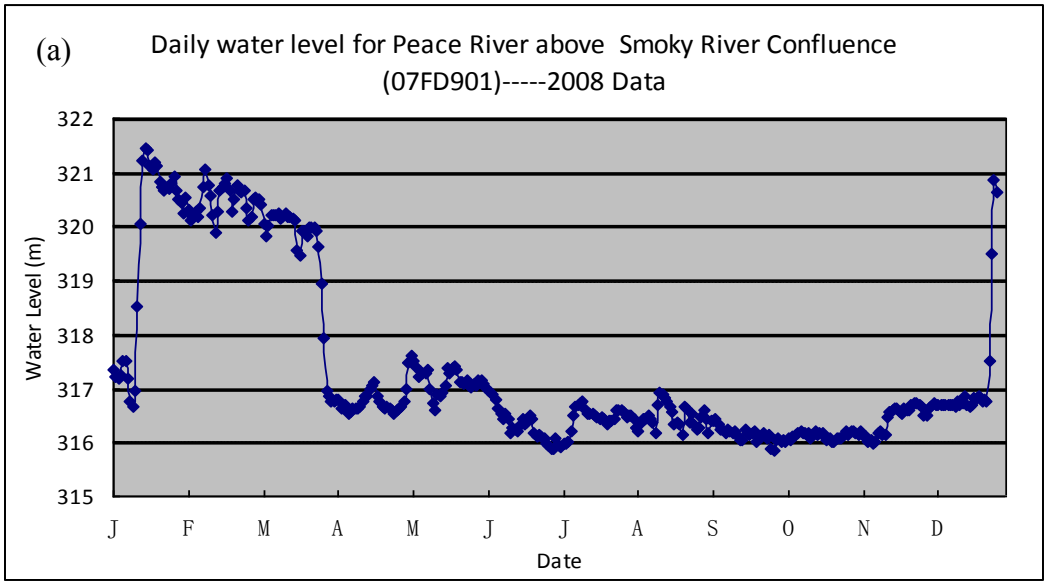

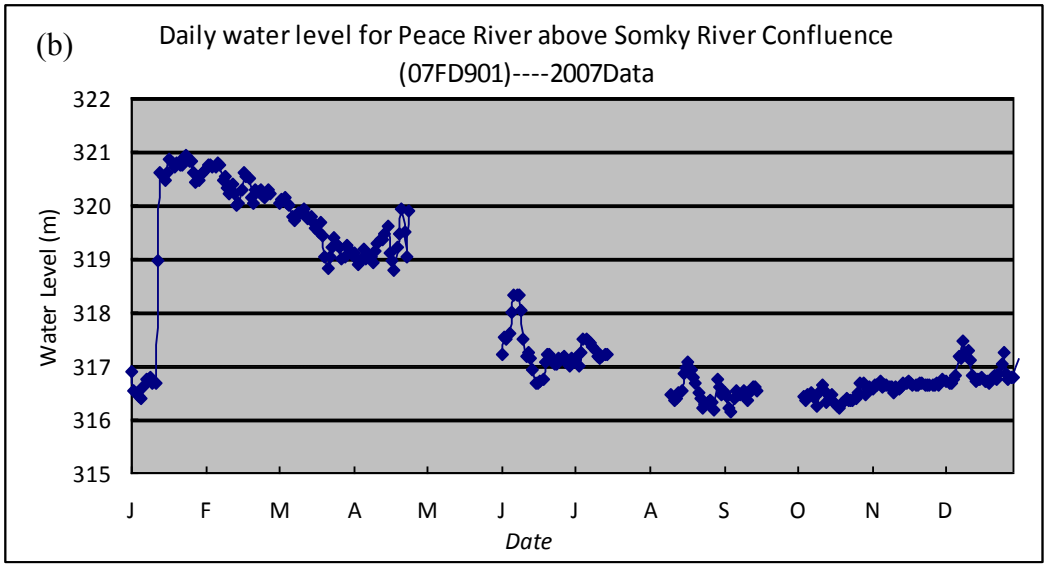

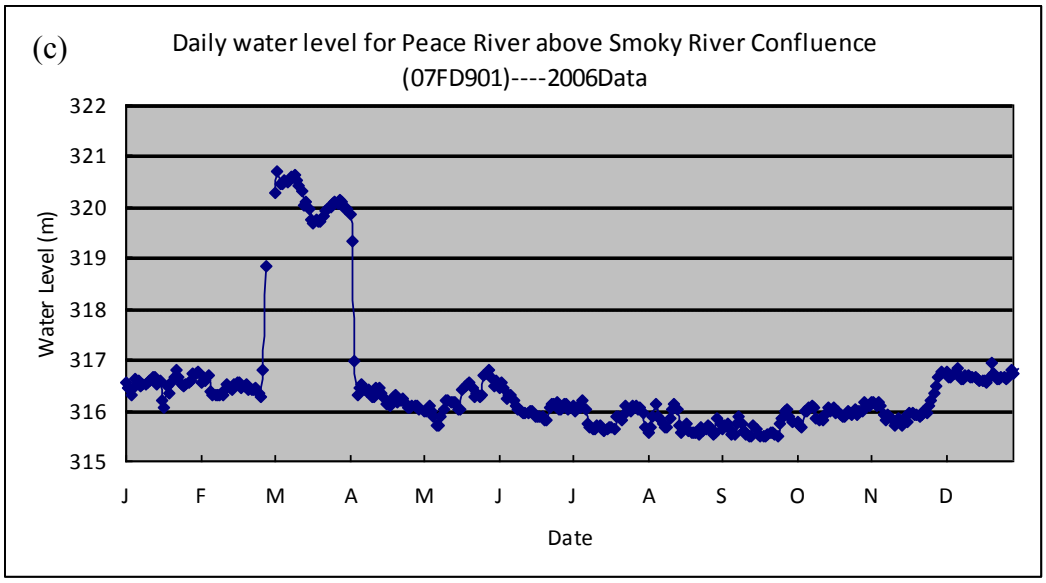

Figure 7 Daily Discharge for Peace River above Smoky River confluence from the year of 2006 to 2008

Figure 7 provides the daily water level at station of 07FD901 which is the Peace River above Smoky River confluence. The water level can be converted to river discharge using rating curve. Since the Peace River is a regulated river after the Hydro's Bennett Dam built in 1972, the water level follows the Dam's regulation. As can be seen in Fig. 7, the water level kept a high value about 320 m during January to April in 2008 and 2007. While in the year of 2006, the situation is slightly different. The peak level occurred in March and April. The values of water level within the rest of the year are pretty much similar which are approximately around 316 m ~317 m.

Peace River at the Town of Peace River (07HA001)

The station named Peace River at the Town of Peace River is the first hydrometric station right after the confluence of Peace River and Smoky River. Due to the two river junction, the river discharge at this station is fairly high comparing with the

Peace River and Smoky River each. As Fig. 8 provided, in 2008, the highest value of discharge was around 4000 m^3/s, which is about 3 times of that at Smoky River. Similarly, the peak flow rate was 3000 m^3/s, also 3 times of that at Smoky River. In 2007, the discharges at Peace River Town and Smoky River were both high, but the flow rate at Peace River Town was still more than 2 times of that of Smoky River.

According to the data obtained from WSC, the mean annual discharge at this station were 1860 m^3/s, 2200 m^3/s and 1350 m^3/s in the year of 2008, 2007, 2006 respectively. As discussed above, the annually mean value of discharge showed that the flow rate of Peace River is about 7 times than that of in Smoky River. (Comparing with the annual mean discharge 257 m^3/s, 394 m^3/s and 170 m^3/s in 2008, 2007 and 2006 at Smoky River).

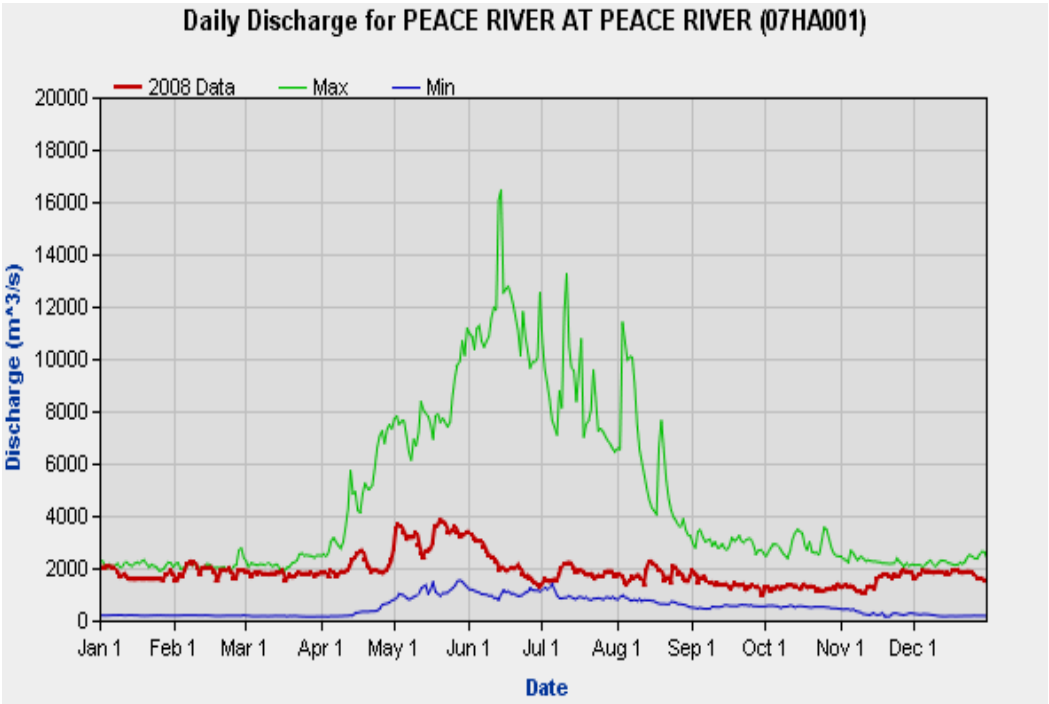

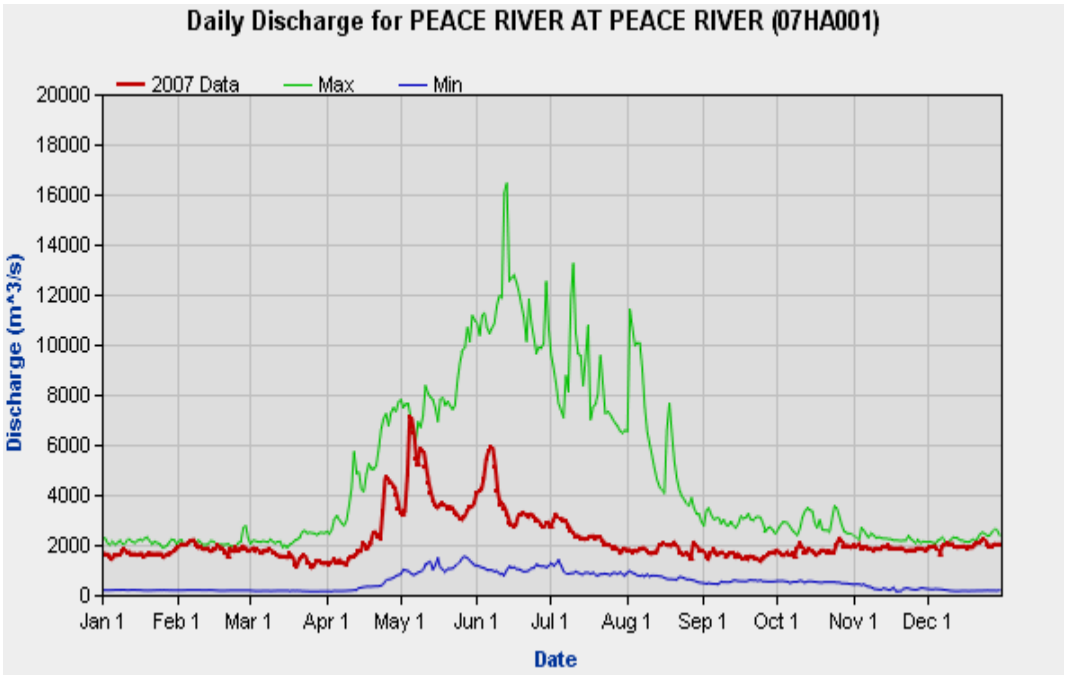

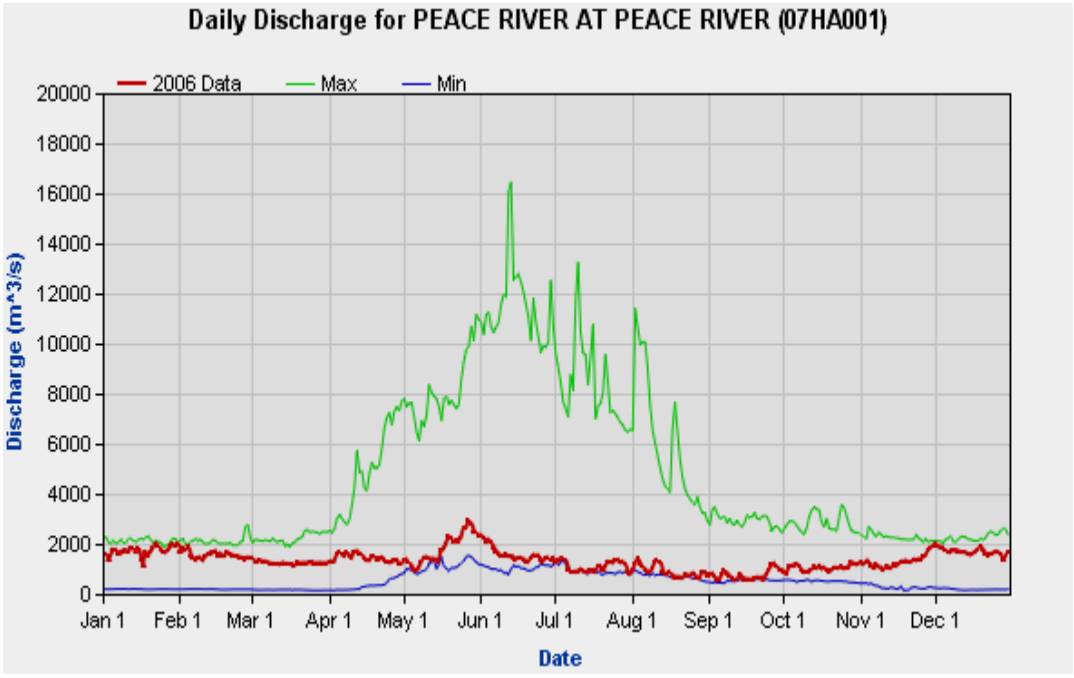

Figure 8 Daily Discharge for Peace River at Peace River Town from the year of 2006 to 2008

<u>Under Ice Condition:</u>

Ice cover is a significant feature of the northern rivers. The ice can not only affect the hydraulics of the river, but also will influent the river's mixing characteristics. As discussed above, the peak and low flow rate occurred in the PS and SR was mainly due to the ice breakup and freeze-up. Therefore the study of ice cover of Peace River within interested reach is necessary.

Table 2 shows the Peace River freeze and Break-up days from the year of 1967 to 2006. As can be seen , the period of ice-cover in Peace River is becoming shorter. In the late 1960's and early 1970's, shortly after the Bennett Dam was constructed, the period of ice-cover was 160 days; in the mid-1980's the period of ice-cover was about 135 days; by the mid-1990's this had slipped to 110 days; and in the last 10 years the ice-cover lasts only about 80 days with the 2004-2005 season having had an ice cover of less than 40 days (Paula Siwik, 2007).

Table 2: Peace River freeze and Break-up days

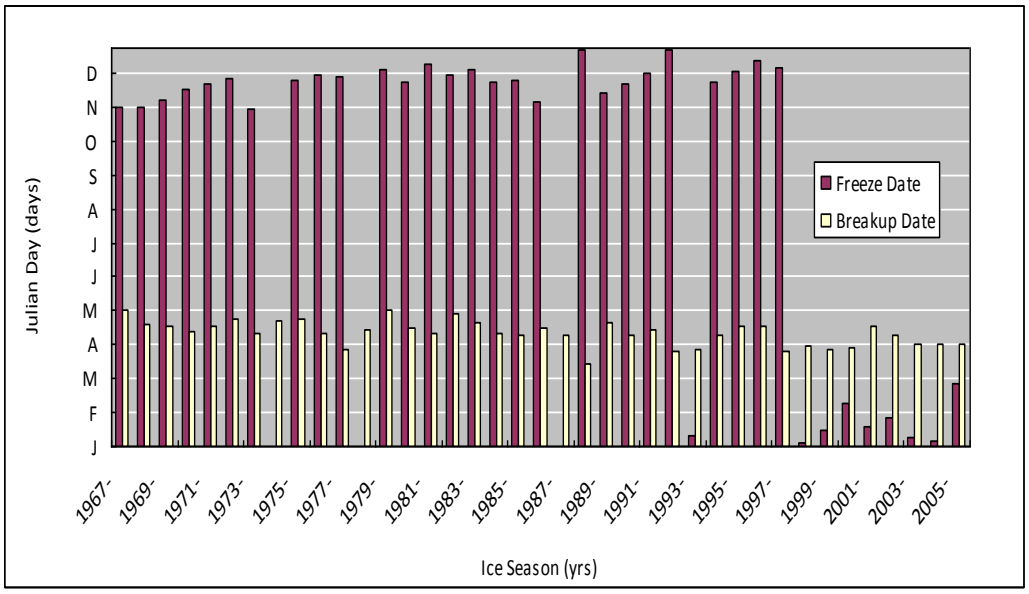

In 1993, C.R.Neill and P.G. Van Der Vinne et.al from Northwest Hydraulic Consultants and Trillium Engineering and Hydrographic conducted a field and analytical study to evaluated under-ice hydraulic characteristics, travel times and mixing parameters from Shaftesbury Ferry through Town of Peace River, Daishowa Bridge, Whitemud River et, down 187 km length to Notikewin River of the Peace River. From the field investigations, they reported that the surface ice cover as far downstream as Whitemud River was generally flat and appeared to have been formed by the juxtaposition of a single layer of ice pans. Downstream of Whitemud River the cover was generally rough and appeared to have been re-formed by sequential consolidation of an initial smoother juxtaposed cover. By drilling 20 holes across each sampling cross-sections, the width-averaged total ice thicknesses are investigated to be 1.0-1.9 m. The river width within this study reach is approximately 400 m, with a gradient of around 0.3 m/km. The depth is up to 15m under winter discharge of around 1700 m^3/s. They indicated that the discharge which was measured under ice condition was fairly close to long-term regulated averaged for the time of year. By using equation Q/A, the mean velocities were calculated as averaged 0.76 m/s and yielded an average Manning roughness of 0.046 as a composite of bed and ice roughness. This value included special energy losses due to channel non-uniformity and possibly parial blockage by frazil ice.

According to the report, the transverse mixing was complete about halfway along the length by doing dye test from the initial station at Shaftesbury Ferry. The transverse mixing coefficients under ice-cover they reported were 0.069 m^2/s from

cross-section Shaftesbury to Mackenzie Cairn, 0.053 m^2/s from Mackenzie Cairn to Peace River, 0.039 m^2/s from Peace River to Daishowa and 0.045 m^2/s from Daishowa to Whitemud. The average transverse mixing coefficient within that study reach was 0.048 m^2/s. They demonstrated that the computed values of transverse mixing parameters based on full-section hydraulics were similar to those of previous studies.

River Water Quality

Dissolved oxygen is highly important for healthy aquatic ecosystems. Dissolved Oxygen concentration always experienced a diminishment in waters during ice cover period in winter, which is indispensable for the survival of many life forms that exist in the aquatic environment.

In the spring of 2005 the dissolved oxygen (DO) concentrations in the Peace River was observed to decline below the water quality guidelines and an investigation is presently underway to determine the potential causes of this drop in the DO levels (Alina Wolanski, private communication). In the past, DO level has not been of concern in the Peace River due to the relatively short period of ice-cover and a large discharge during the typical low flow winter seasons. The Peace River is normally a highly oxygenated river, averaging 11.4 mg/L dissolved oxygen near Fort Vermillion. However, river monitoring on March 15, 2005 come up with a DO concentration of 5.35 mg/L at this station, which is close to the acute Alberta Surface Water Quality Guideline for the Protection of Aquatic Life (Guidelines, 5 mg/L). The report on a low dissolved oxygen concentration

event in the Peace River, Spring 2005 indicated the reason that this results made a link between early and rapid spring runoff and Peace River peak water level and low DO.

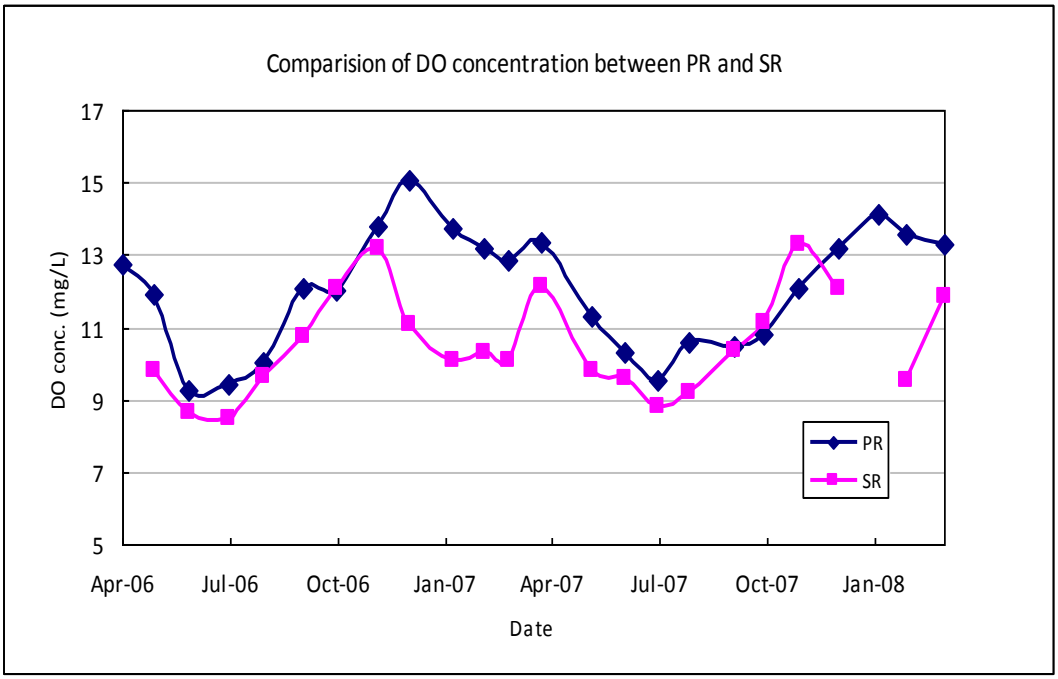

Figure 9 Comparison of DO concentrations between PR and SR

Dissolved oxygen concentration is sampled monthly by AENV, Fig. 9 listed the DO concentration in AENV water quality data index, the sampling time for these two series of data are close, thus the value of DO concentration is valid to compare. From the figure it is clear that the DO concentration of Smoky River is always lower than that in PR before confluence with Smoky River. So it is expected that after Smoky River joined with Peace River, DO concentration will decrease. Furthermore, the DMI effluent discharge, which is located about 15 km downstream of the Town of the Peace River, is included in the mixing length for these two rivers, which may induce a further impact on the PR DO concentration.

In table 6, the April-2006 to Mar-2008 data for SR river at Watino is lower than PR, but still falls into an acceptable region, which exceeds the required limit by Alberta Environment.

Recently, a number of the issues have been raised. According to Alina Wolanski (AENV, private communication), monitoring data collected from the Town of the Peace River's WWTP showed that between February and April 2008 levels of Ammonia Nitrogen in the final effluent increased significantly and ranged between 9.2 and 21.8 mg/L. Discharges of effluent with high Ammonia levels are highly undesirable and can be detrimental to the aquatic biota. The above Ammonia levels are at levels toxic to aquatic biota. While the WWTP final effluent discharge rate generally remains below 0.2 m^3/s and the river has a very high dilution potential, it is still important to delineate the effluent plume to identify the region where Ammonia level exceeds the surface water quality guidelines.

In addition to the industrial and municipal point-source discharges, significant cumulative loadings of nutrients (N and P) from various sources, input of contaminants from agricultural areas, orphan wells and natural gas seepage into the Peace River can significantly affect the water quality.

Water temperature is another main water quality factor. The difference between the temperatures of two mixing streams can be used to visualize the mixing process downstream of two river confluence. Thermal infrared (TIR) images can be a reference indicating the mixing layer between two stream flow surfaces.

Monitoring of river temperatures has been conducted to understand the thermal behaviour of river flows, and subsequently provide another possible method to evaluate the mixing process and river confluence.

WSC monitors continuous water temperature data for some of their sampling locations, the water temperatures are monitored by Long-Term River Network Stations. The differences of annually water temperature can vary by about 0~7.73 ℃ between the Peace River and the Smokey River during the year of 2006-2008. The maximum difference value occurred on 22nd May 2007. As shown in Tab. 3, during winter time the water temperature vary not that much, around 0~1.21 ℃. During summer time it will vary from 4.65-7.73℃.

Table 3: Temperature of Peace River and Smokey River

Smoky River at Watino	T (℃)	Peace River above confluence	T (℃)	Difference
4/19/2006 13:00	3.02	4/19/2006 11:15	4.23	*1.21*
5/15/2006 13:00	13.8	5/15/2006 11:30	9.15	*4.65*
6/14/2006 13:35	18.13	6/14/2006 11:15	17.35	*0.78*
7/18/2006 13:45	18.63	7/18/2006 11:20	17.92	*0.71*
8/16/2006 12:45	19.14	8/16/2006 11:30	16.5	*2.64*
9/20/2006 11:30	10.03	9/19/2006 9:45	9.77	*0.26*
10/18/2006 12:50	4.59	10/18/2006 11:20	7.32	*2.73*
11/21/2006 13:05	0.01	11/21/2006 11:25	0.96	*0.95*
12/20/2006 9:30	-0.25	12/19/2006 15:00	-0.25	*0*
1/18/2007 14:30	-0.25	1/24/2007 13:15	-0.25	*0*
2/22/2007 14:00	-0.27	2/20/2007 14:30	-0.26	*0.01*
3/14/2007 12:30	-0.24	3/12/2007 13:30	-0.24	*0*
4/4/2007 12:15	-0.28	4/10/2007 12:15	-0.28	*0*
5/22/2007 11:15	**0.78**	**5/22/2007 10:15**	**8.51**	***7.73***
6/20/2007 13:15	13.18	6/20/2007 11:00	11.43	*1.75*
7/17/2007 13:15	20.73	7/17/2007 11:30	16.46	*4.27*
8/14/2007 11:40	15.15	8/14/2007 10:00	11.43	*3.72*
9/20/2007 12:45	10.16	9/20/2007 10:45	10.36	*0.2*
10/16/2007 11:20	5.93	10/16/2007 9:45	8.26	*2.33*
11/15/2007 11:50	-0.25	11/15/2007 10:20	3.69	*3.94*
12/19/2007 14:30	-0.13	12/19/2007 11:45	0.3	*0.43*
1/16/2008 13:30	-0.09	1/21/2008 12:45	-0.3	*0.21*
2/14/2008 12:15	-0.33	2/14/2008 10:00	-0.32	*0.01*
3/17/2008 10:15	-0.12	3/17/2008 13:00	-0.12	*0*

Summary

The idea of this research is originally from this real river confluence. This research has provided the knowledge of the flow dynamics (flow velocity distribution, circulation patterns, *etc.*) and the mixing characteristics (mixing interface evolution, transverse mixing coefficient, *etc.*) at lab-scale confluence. However, good field data is needed for lab study and numerical model calibrations to study the mixing of the tributary and the waste streams (effluent discharges) at large river confluence. In addition, there have been very limited field studies on the multi-port diffusers in rivers (with the only exceptions being the recent work by Zhang & Zhu, 2009), especially at river confluence. Therefore, the study of the performance of diffusers at channel confluence would be a great contribution to the river confluence environment.